Experimental study of transport phenomena in the condenser of an OTEC-cycle

M.E. Dahlgren

Master of Science Thesis

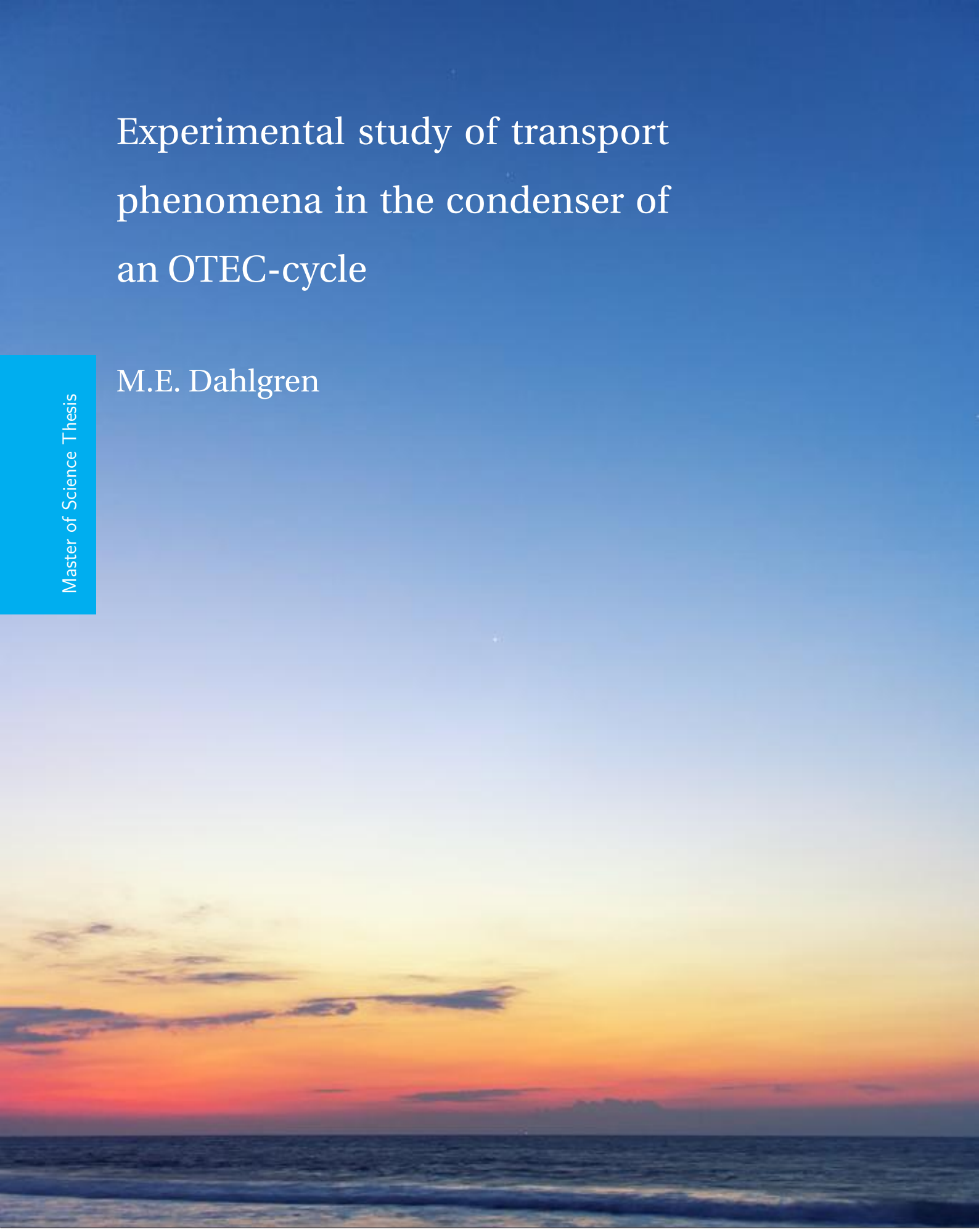

TU Delft Delft University of Technology

Challenge the future

EXPERIMENTAL STUDY OF TRANSPORT PHENOMENA IN THE CONDENSER OF AN OTEC-CYCLE

by

M.E. Dahlgren

to obtain the degree of Master of Science
at the Delft University of Technology,
to be defended publicly on Monday April 30, 2018 at 13:00.

Student number:	4016572	
Project duration:	Februari 1, 2017 – April 30, 2018	
Thesis committee:	Dr. B. P. Tighe,	TU Delft
	Dr.ir. C. A. Infante Ferreira,	TU Delft, supervisor
	Ir. J. A. Kirkenier,	Bluerise B.V., supervisor
	Prof.dr.ir. W. de Jong,	TU Delft

This thesis is confidential and cannot be made public until April 30, 2023.

TU Delft Delft University of Technology

Bluerise harnessing the ocean's power

,

ABSTRACT

In the search for new forms of renewable energy production, an interesting option is to make use of the energy stored in the ocean in tropical areas. The sun heats up the surface water in these areas to a point it is feasible to generate electricity, using the temperature difference between the hot surface water and the cold ocean water at around 1 [km] depth. This form of renewable energy production is called Ocean Thermal Energy Conversion (OTEC). As the water temperature in these areas is quite constant, the electricity generation is quite constant as well, which is a big advantage as no inefficient energy storage or unsustainable base load generation is needed. To make OTEC power generation more economically attractive, design optimization and technology up-scaling need to be done, lowering the costs of the components and making sure the components work as efficiently as possible. A crucial component is the condenser. In the condenser, heat is transferred from the working fluid in the cycle (most commonly ammonia or ammonia-water) to the cold water. The working fluid is condensed, which can then be pumped around. The process of pumping the water up from 1 [km] depth is a costly operation (Kirkenier, 2014) [1] and the condenser itself is a significant part of the cost of an OTEC-plant. It is relevant to gain more insight in the transport phenomena in the condenser by executing experiments, so the cost can be reduced.

The experimental set-up is a small scale OTEC cycle prototype (OTEC-demo), located in the Process & Energy laboratory at the Delft University of technology. For this research, a gasketed plate heat exchanger is added to the set-up, which can be used as a condenser. On the gasketed plate heat exchanger it is possible to apply some modifications and to change the number of plates, as the heat exchanger can be disassembled. Nine miniature temperature sensors are placed along the flow direction of one of the heat transfer plates for local temperatures measurements. For future research on the flow patterns in the condenser, a transparent corrugated plate was designed and fabricated for visualization purposes. First, the plate was designed with 3D CAD software. Then, the plate was constructed by milling, at the central workshop of the Delft University of Technology.

A single phase convective heat transfer coefficient correlation and a pressure drop correlation for the cold water side in the condenser were proposed, by executing experiments with water on both sides of the heat transfer plates in the gasketed plate heat exchanger.

In order to research the influence of the vapour quality and the mass flux on the convective heat transfer coefficient on the working fluid side, ammonia-water mixture condensation experiments were executed. During the experiments, the measured cold water temperature profiles were linear for all the set mass flows. This means the convective heat transfer coefficient did not change much along the flow direction of the plate, which can be explained by the small change in vapour quality during the ammonia-water mixture experiments. The convective heat transfer coefficient on the working fluid side increases for increasing mass flux and also increases for increasing vapour quality.

The results of these experiments were compared to the theory. A numerical condenser model, which can predict the measured data, was developed. The numerical condenser model is a modification of the numerical condenser model by Goudriaan [2] and Kuikhoven [3]. By comparing the results of the experiments to the results from the model, the assumptions made in the model can be validated. The model can predict the cold water inlet temperature and the working fluid outlet temperature of the experimental data within an accuracy of 4%. However, this only applies to the measured range of experiments. More experiments are required to propose correlations that are valid in a higher range of mass flows and vapour qualities.

Furthermore, pure ammonia experiments were executed. The results were compared to the ammonia-water mixture experiments. The convective and overall heat transfer coefficients decreased for increasing mass flux during the pure ammonia experiments, while the convective and overall heat transfer coefficients increased for increasing mass flux during the ammonia-water mixture experiments. More experiments are needed to investigate this phenomenon. The pressure drop of the pure ammonia flow is slightly higher than the pressure drop of the ammonia-water mixture, due to the lower density of pure ammonia.

ACKNOWLEDGEMENTS

I would first like to thank my thesis supervisor Dr.ir. Carlos Infante Ferreira at the Delft University of Technology. I had weekly meetings with him from which I gained a lot of useful feedback. I am also very grateful to my daily supervisor Xuan Tao, who is doing his PhD on flow patterns in plate heat exchangers and local heat and mass transfer processes at the Delft University of technology. We formed a good partnership and his door was always open to me. Furthermore, I would like to thank Joost Kirkenier from Bluerise B.V. for his supervision. He was always helpful when I needed it. Another special gratitude goes to Bram Harmsen from Bluerise B.V. He helped me with practical problems with the experimental set-up and his programming skills were very helpful whenever I had software issues. I would also like to thank the technicians and support staff of the Process & Energy lab, Daniel van Baarle and Jaap van Raamt in particular, for their help with the construction of the extension of the OTEC-demo set-up. Last but not least, I want to thank all my Bluerise colleagues for the interesting discussions and entertaining moments during my thesis. It was a great pleasure.

M.E. Dahlgren
Delft, April 2018

CONTENTS

NOMENCLATURE

Greek Symbols

α	Convective heat transfer coefficient	$[W/(m^2 \cdot K)]$
β	Chevron angle	$[°]$
Δ	Difference	[-]
δ	Deflection	[m]
γ	Aspect ratio	[-]
κ	Thermal conductivity	$[W/(m \cdot K)]$
Λ	Property modifying parameter	[-]
Λ_{wave}	Corrugation wave length	[m]
μ	Kinematic viscosity	$[Pa \cdot s]$
ν	Poisson ratio	[-]
Φ	Surface enhancement factor	[-]
ρ	Density	$[kg/m^3]$
σ	Surface tension	[N/m]
ξ	Drag coefficient	[-]
ζ	Friction factor	[-]
v	Specific volume	$[m^3/kg]$

Roman Symbols

$\hat{a}$	Corrugation amplitude	[m]
A	Heat transfer area	$[m^2]$
a	Height of channel	[m]
A_f	Flow passage area	$[m^2]$
b	Width of channel	[m]
Bo	Boiling number	[-]
c_p	Specific heat capacity	$[J/(kg \cdot K)]$
d_{eq}	Equivalent diameter	[m]
d_g	Channel gap	[m]
d_h	Hydraulic diameter	[m]
D_p	Port diameter	[m]
d_p	Plate thickness	[m]

E	Young's modulus	[Pa]
f	Fanning friction factor	[-]
Fr	Froude number	[-]
G	Mass flux	[kg/(m$^2 \cdot$s)]
g	Gravitational constant	[m/s^2]
h	Enthalpy	[J/kg]
h_{fg}	Latent heat	[J/kg]
K	Loss coefficient	[-]
L	Characteristic length	[m]
L_h	Port-to-port width of plate	[m]
L_p	Effective length of plate	[m]
L_v	Port-to-port length of plate	[m]
L_w	Effective width of flow passage area	[m]
$\dot{m}$	Mass flow	[kg/s]
N_{ch}	Number of channels	[-]
N_e	Effective number of plates	[-]
N_t	Total number of plates	[-]
Nu	Nusselt number	[-]
P	Pressure	[Pa]
p	Corrugation pitch	[m]
p_{cp}	Compressed plate pitch	[m]
Pr	Prandtl number	[-]
Q	Heat transfer	[W]
q	Heat flux	[W/m^2]
Re	Reynolds number	[-]
R_v	Gas to liquid velocity ratio	[-]
Sc	Schmidt number	[-]
T	Temperature	[°C]
U_0	Characteristic flow velocity	[m/s]
U	Overall heat transfer coefficient	[W/(m$^2 \cdot$K)]
U_G	Superficial gas phase velocity	[m/s]
U_L	Superficial liquid phase velocity	[m/s]
$\dot{V}$	Volumetric flow	[m^3/s]
w	Velocity	[m/s]

X	Ammonia mass based concentration	[-]
x	Vapor quality	[-]

Subscripts

av	Averaged
$brazed$	Brazed heat exchanger
c	Cold
$calc$	Calculated
$cond$	Condenser
cr	Critical
cv	Control volume
e	Effective
ele	Elevation
eq	Equivalent
$evap$	Evaporator
f	Friction
G	Gas/vapour
$gasketed$	Gasketed heat exchanger
h	Hot
hex	Heat exchanger
hor	Horizontal
in	Conditions at inlet
L	Liquid
LM	Logarithmic
LO	Liquid only
out	Conditions at outlet
sat	Saturated condition
SP	Single phase
TP	Two-phase
v	Velocity
ver	Vertical
$water$	Water
wf	Working fluid

List of Figures

List of Tables

1

INTRODUCTION

In the search for new forms of renewable energy, an interesting option is to make use of the energy stored in the ocean in tropical areas. The sun heats up the surface water in these areas to a point it is feasible to generate electricity, which is clean and has no emissions. Moreover, since the water temperature in these areas is quite constant, the electricity generation will be quite constant as well, which is a big advantage as no inefficient energy storage or unsustainable base load generation is needed.

1.1. OTEC

The process of generating energy from the ocean is called Ocean Thermal Energy Conversion (OTEC). Warm surface water is used to evaporate a working fluid with a low boiling point in a closed system (see figure 1.1). The working fluid vapour flows through a turbine, generating mechanical energy, which is converted to electricity with a generator. The working fluid is then condensed using the cold deep sea water. The liquid can be pumped back to the evaporator, creating a continuous power generating cycle.

Figure 1.2 shows the potential of OTEC in the earth's waters. In the yellow, orange and red areas, OTEC power generation is feasible, as the thermal gradient and depth of the water are sufficient here. The red color indicates where potential is the highest. It is estimated that OTEC could potentially provide 7 - 30 TW of power (Rajagopalan and Nihous [29]).

1.2. BLUERISE B.V.

Bluerise develops solutions to harness the ocean's power ([30]). Bluerise is a technology provider and project developer of Ocean Thermal Energy solutions. The thermal energy stored in the tropical ocean can be used to generate sustainable electricity, cooling, and fresh water. Bluerise specializes in OTEC (Ocean Thermal Energy Conversion), SWAC (Seawater Air Conditioning) technologies and related Deep Sea Water applications.

Bluerise provides technology and development plans for implementation of OTEC and SWAC as well as Ocean Ecoparks that utilize the ocean resource by means of innovative technologies for desalination, agriculture and aquaculture among others.

Creative thinking, a sustainable mindset and a fresh 21st century look at all system components drives Bluerise to design economical viable and technically feasible solutions. Bluerise provides consulting and engineering services to governments, project developers, energy companies and utilities.

Together with the Delft University of Technology, Bluerise has built and tested an OTEC demonstration plant, which allows the gathering of useful data on the performance of an OTEC-cycle.

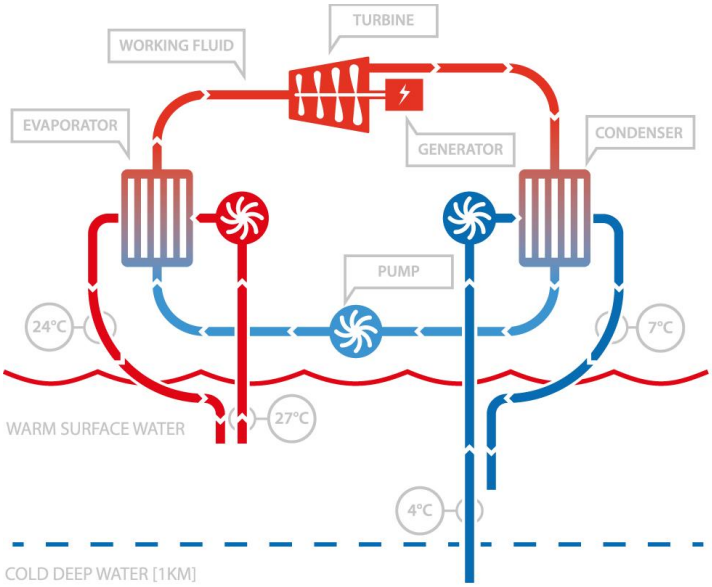

Figure 1.1: The OTEC-principle, using a rankine cycle.

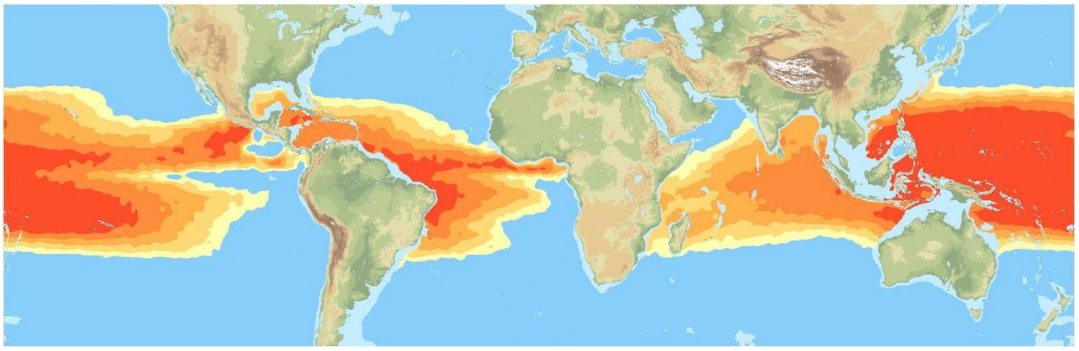

Figure 1.2: The potential of OTEC in the earth's waters, the red colour indicating the highest potential and the blue colour indicating no potential.

1.3. THESIS SCOPE

To make OTEC power generation more economically attractive, design optimization and technology upscaling needs to be done, lowering the costs of the components and making sure the components work as efficiently as possible.

A crucial component is the condenser. In the condenser, the working fluid and cold deep sea water exchange heat, which changes the phase of the working fluid from vapour to liquid. Figure 1.3 shows a plate heat exchanger, which can be used as a condenser. The cold deep sea water is very valuable as the process of pumping the water up from 1 [km] depth is a costly operation (Kirkenier [1]). Therefore, it is essential that the cold water is used as efficiently as possible by optimizing the heat transfer in the condenser. For this purpose, a better understanding of the condensing process is needed.

The most common working fluid in OTEC-cycle analyses is pure ammonia or an ammonia-water mixture (which is used in the Kalina cycle. The Kalina cycle will be discussed in chapter 3). The most common type of heat exchanger used in the cycle is the plate heat exchanger. Plate heat exchangers have been identified as very suitable for phase change application (Abu-Khader [31]) and to have favourable heat transfer coefficients (Thulukkanam [32]). In plate heat exchangers, heat is exchanged through plates that separate the cold and warm mass flows, that flow in opposite directions (see figure 1.3). The plates create channels between them, with either a warm or cold flow.

There is a significant literature gap on condensing flows, especially compared to evaporating flows. On ammonia(-water) condensing in OTEC-cycles very limited research is available while the scientific relevance is high. Research on ammonia(-water) condensers could not only be valuable for OTEC-cycles, but also for condensing two-phase flow modelling in general. Nuijten [33] developed a model which can predict absorption phenomena of binary mixtures in plate heat exchangers and identified the need for visualization experiments. Geschiere [25] created a numerical condenser model for the OTEC-demo cycle.

The parameters in the condenser which are the most relevant and for which little information is available, are the pressure drop, the temperature profile and the flow pattern in the condenser of an OTEC-cycle. All these parameters are expected to have an impact on the heat transfer in the condenser.

Experiments are needed to gain more information on these parameters. The pressure drop can be investigated by varying the amount of plates in the heat exchanger which is used as a condenser or varying the mass flows. Visualization experiments are needed to identify flow patterns. Temperature profiles can be measured by executing experiments with temperature sensors placed locally along a heat transfer plate.

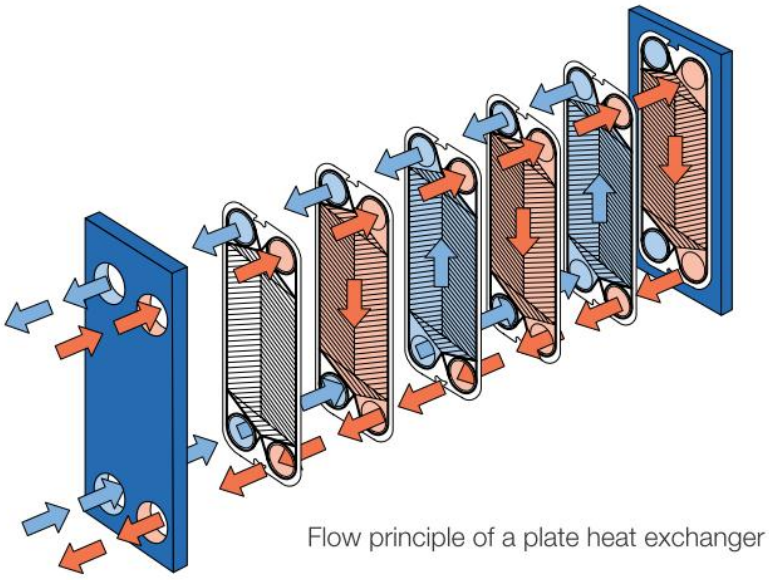

Figure 1.3: The flow principle in a plate heat exchanger, which can be used as a condenser. [4]

1.4. OBJECTIVES

The overall goal of this thesis is to gain a better understanding of the transport phenomena taking place in the condenser of an OTEC-cycle.

In order to achieve this goal, the following sub-goals are identified:

- Design an extension to the existing set-up that allows identification of the flow patterns in the condenser
- Propose pressure drop correlations for the condenser on the working fluid and water sides
- Determine temperature profiles in the condenser and propose heat transfer correlations for the working fluid and water side
- Create a model which can predict the experimental outcomes

1.5. APPROACH

The objectives will be reached by performing the following steps:

1. Literature study. Make an overview of recent visualization studies on (condensing) two-phase flow in plate heat exchangers and an overview of previous designs of the visualization section. Also make an overview of studies which include local temperature measurements.
2. Experimental set-up modifications. Propose modifications to the OTEC set-up so that the experiments can be executed. Design a visualization section for the plate heat exchanger which will be used as a condenser. Implement the required modifications to the set-up and define the visualization section.
3. Condenser model. Study the existing condenser model by Goudriaan [2] and Kuikhoven [3] of the OTEC set-up and modify it to fit the design of the new condenser.
4. Experiments. Execute the proposed experimental programme, process the data and investigate the impact of the varying input parameters.
5. Conclusion. Draw conclusions from the research and propose further research.

1.6. THESIS OUTLINE

In chapter 2, the main contributions to the identification of the transport phenomena are shown. This review assists in finding suitable methods to significantly contribute to a better understanding of the phenomena. Chapter 3 indicates how the methods are implemented. The experimental set-up (the OTEC-demo) is explained and the required modifications to the OTEC-demo needed for this research are discussed. In chapter 4, the impact of these modifications on the existing condenser model by Goudriaan [2] and Kuikhoven [3], are discussed. The changes to the existing model are detailed. In chapter 5, the results of all the experiments are shown, discussed and compared to the modified model outcomes. The performance of the modified model is evaluated. Chapter 6 presents the conclusion of this thesis and recommendations for further research.

2

LITERATURE REVIEW

In chapter 1 was stated that visualization experiments are needed in order to identify flow patterns in the condenser of the OTEC-cycle. Furthermore, local temperature measurements are required to construct temperature profiles along the condenser of the OTEC-cycle. In this chapter, a literature review on relevant flow visualization studies and studies with local temperature measurements is given.

Tao *et al.* [13] (2018) present a literature review of work related to the two-phase flow patterns of vertical downward flow in corrugated chevron plate heat exchangers. Tao *et al.* [13] (2018) conclude that the subjectivity of the observations in the currently available flow visualization studies needed to be reduced by doing new experiments. These experiments need to have unified criteria for lighting conditions, imaging quality and the thickness and material of transparent plates. In the first section of this chapter, an overview of relevant flow visualization studies is made, including these parameters.

Tao *et al.* [13] (2018) also state that incomplete reporting of experimental conditions is a problem for some of the previous visualization studies. In the second section of this chapter, the relevant parameters for the construction of flow pattern maps are determined.

2.1. FLOW VISUALIZATION STUDIES

Grabenstein *et al.* [34] (2017) present an experimental study, in which a flow pattern map for two-phase flow in the gap formed between two corrugated plates and pressure drop correlations connected to each flow regime are proposed. The experimental set-up is schematically shown in figure 2.1. The study gives an overview of two-phase flow patterns in plate heat exchangers. For the experimental analysis, two corrugated transparent polyurethane plates forming a single gap were used.

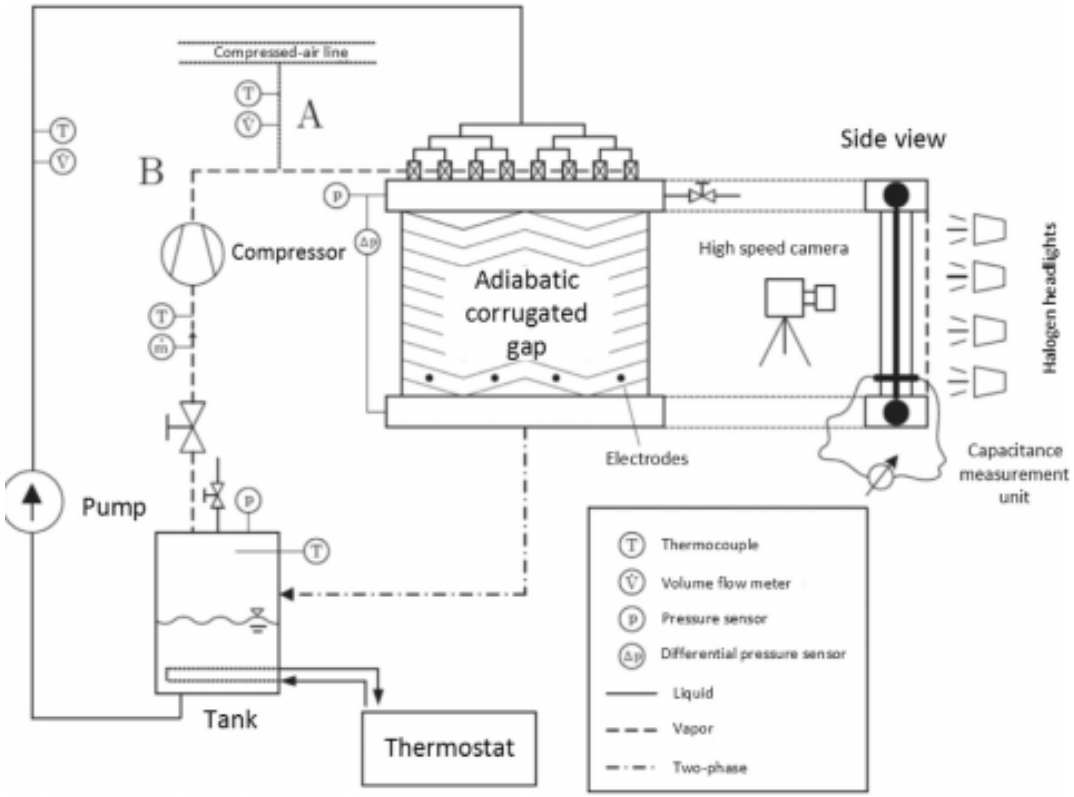

Figure 2.1: Schematic view of the visualization set-up of Grabenstein et al. (2017)

Koyama *et al.* [5] (2014) investigated FC-72 flow boiling in a plate heat exchanger. A transparent acrylic cover with a thickness of 40 [mm] is used to make flow visualization possible (see figure 2.2). In this study, some thermodynamic conditions of the FC-72 are reported: a temperature of $T = 52$ [$^{\circ}C$] at the inlet of the heat exchanger and a fixed saturation pressure of $p = 100$ [kPa].

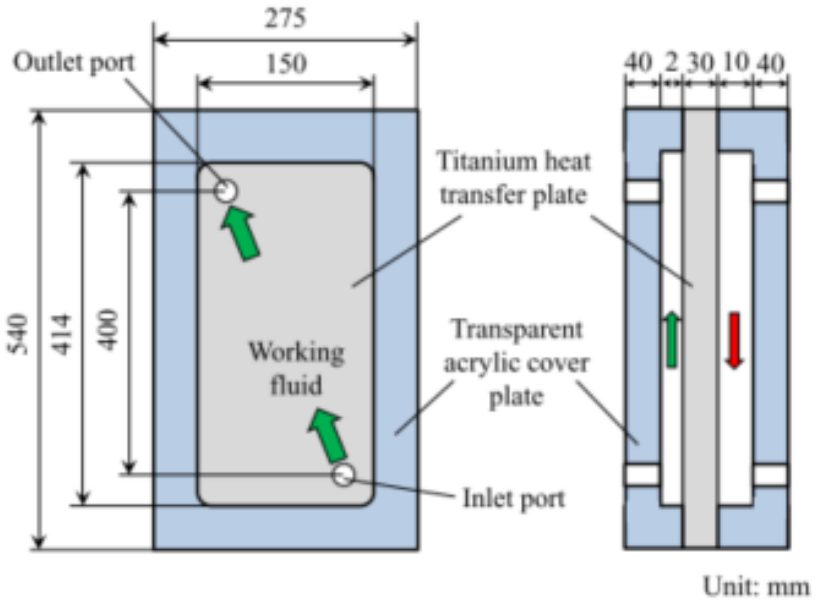

Figure 2.2: Schematic view of the visualization set-up of Koyama *et al.* [5] (2014).

Arima *et al.* [6] (2011) is one of the few studies in which a visualization set-up for a two-phase ammonia-water mixture flow has been designed. The set-up consists of a single pass heat exchanger, with sight glasses on the evaporating working fluid side (see figure 2.3). For the test plate, SUS304 stainless steel was used. The material of the sight glass is not mentioned explicitly, but it's assumed to be glass. The light source was a 250 [W] cold lamp. Images are captured using a digital still camera (Pentax *istD).

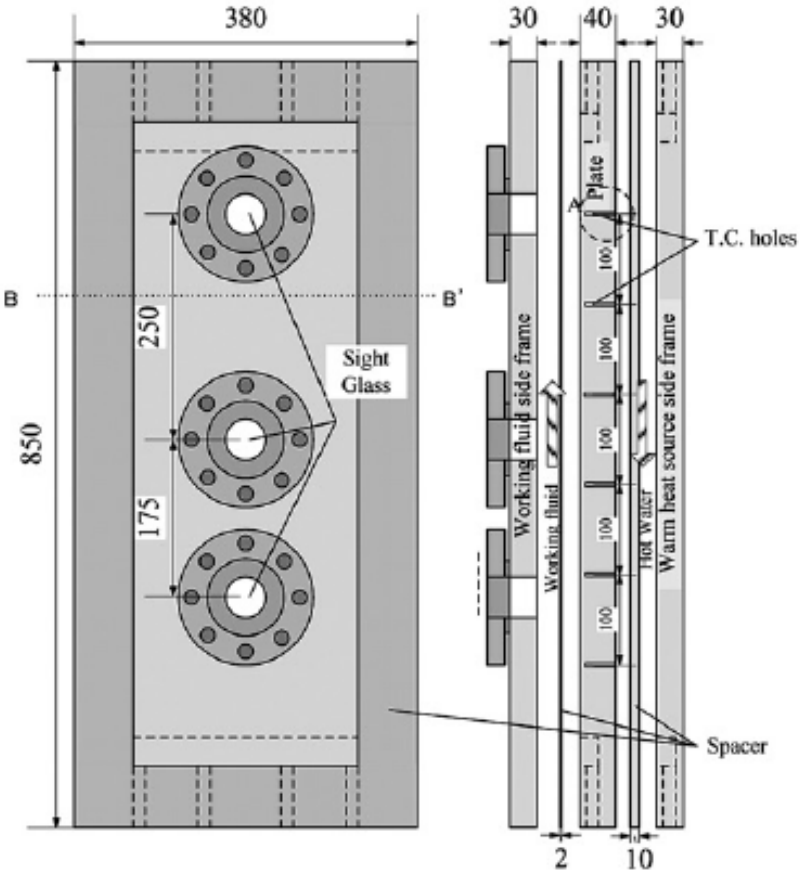

Figure 2.3: Schematic view of the visualization set-up of Arima *et al.* [6] (2011).

Winkelmann [7] (2010) presents an experimental study for a two-phase air-water flow, in which pressure measurements are done and the flow is visualized to draw a preliminary flow pattern map. Figure 2.4 shows the setup of the study, the test section consists of one flow channel. The flow is visualized by using a 40 [mm] thick transparent corrugated plastic plate. Pictures were taken with a small digital camera and a high speed video camera (500 frames per second).

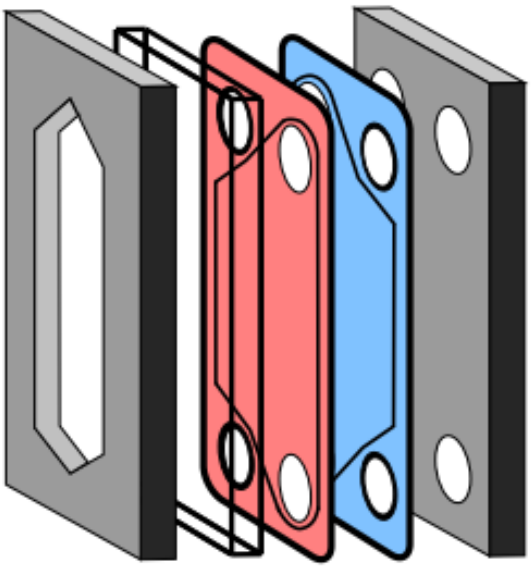

Figure 2.4: Exploded view of the visualization set-up of Winkelmann [7] (2010).

Nilpueng and Wongwises [8] (2010) investigated the air-water two-phase flow characteristics including flow patterns and pressure drop inside a plate heat exchanger. For the experiment, a plate heat exchanger with a single pass under the condition of counter flow is used (see figure 2.5). The material used for the embossed transparent plate, is polyurethane. The thickness of the transparent plate is 30 [mm]. Images are created using a digital camera (Sumsung DigimaxV3). The images published in the paper show some slight visibility problems due to light reflections on the stainless steel plate behind the transparent plate.

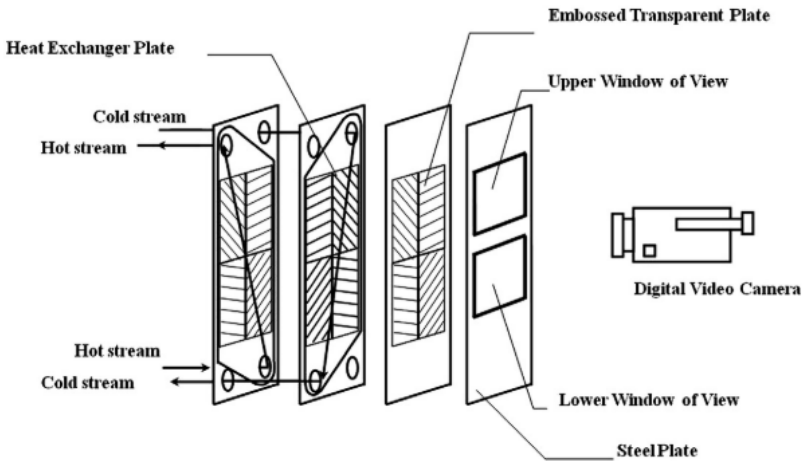

Figure 2.5: Schematic view of the visualization set-up of Nilpueng and Wongwises [8] (2010).

Jassim *et al.* [9] (2006) conducted R134a flow visualization experiments in chevron and bumpy style flat plate heat exchangers. Figure 2.6 shows the flow loop of Jassim et al. (2006), including the test section. The visualization set up of the study is shown in figure 2.7. Three different styles of transparent flat plate evaporator test sections were constructed: a chevron plate, a bumpy plate with a 2:1 bump aspect ratio, and a bumpy plate with a 1:1 bump aspect ratio. All transparent plates were machined from 12.7 [mm]-thick PVC. A stroboscope, which reflected light off a white background, was used to improve the visualization.

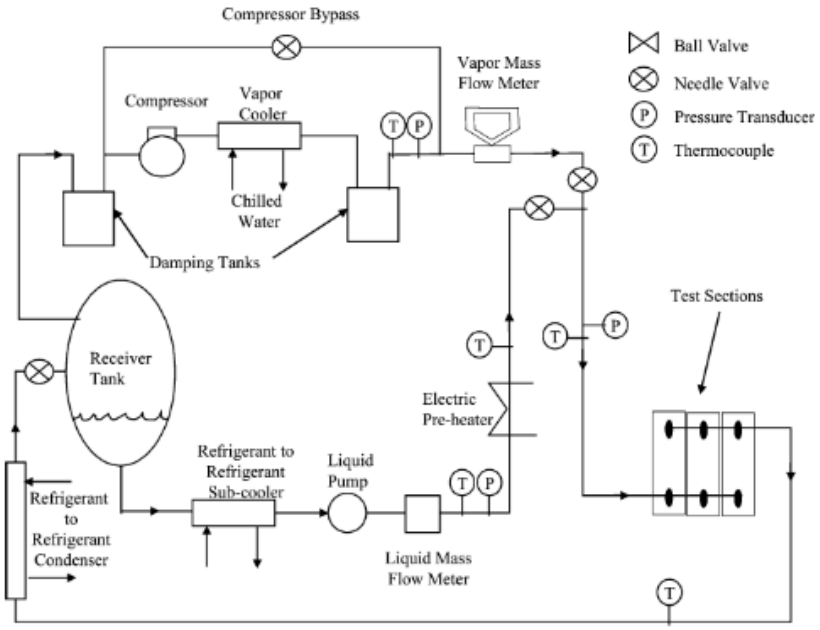

Figure 2.6: Schematic view of the flow loop of Jassim *et al.* [9] (2006).

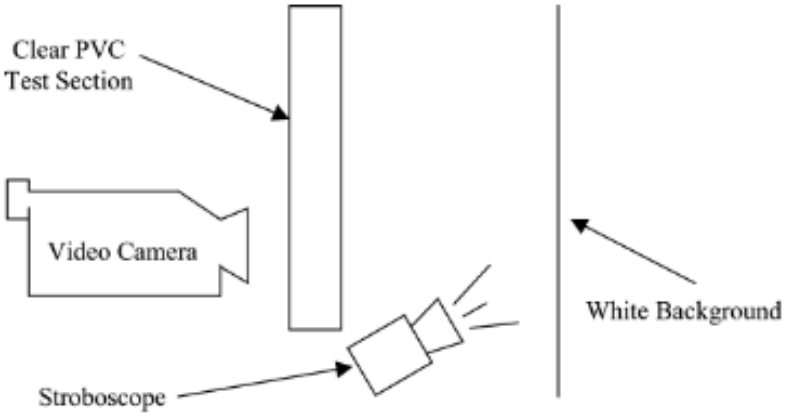

Figure 2.7: Schematic view of the visualization set-up of Jassim *et al.* [9] (2006).

Asano *et al.* [10] (2005) performed a visualization experiment and obtained the void fraction distribution of downward air-water two-phase flow in a plate heat exchanger, using neutron radiography. The study investigated the liquid distribution over the channels by evaluating the volumetric fraction in each channel. Figure 2.8 shows the experimental apparatus of Asano et al. (2005).

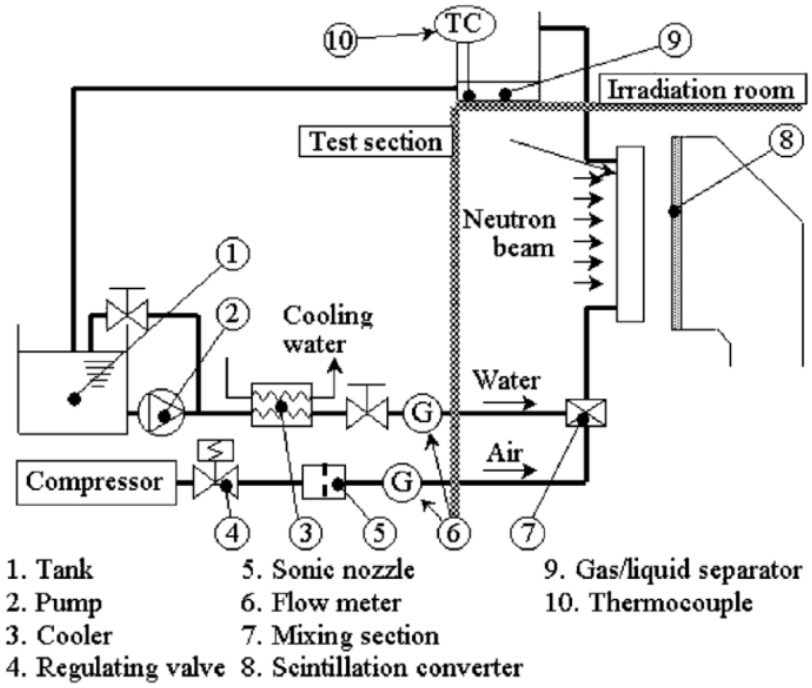

Figure 2.8: Schematic view of the experimental apparatus of Asano *et al.* [10] (2005).

Vlasogiannis *et al.* [11] (2002) present a visualization study for a two-phase air-water mixture in a plate heat exchanger. For the visualization, the movable end covers of the plate heat exchanger are replaced by a 30 [mm] thick corrugated plexiglass plate. The corrugation on the plexiglass plate is created using lithographic techniques. Figure 2.9 shows the visualization set-up of Vlasogiannis et al. (2002). As shown in the figure, UV-light is used to enhance the visual contrast between the gas and the liquid phase. Some operating conditions are mentioned in the study: a temperature of 40°C for the hot inlet water stream and 25°C for the cold air-water stream. The 13 stainless steel plates provide 6 flow channels per stream. A RedLake Motion Scope PCI high-speed video camera is used for recording the images.

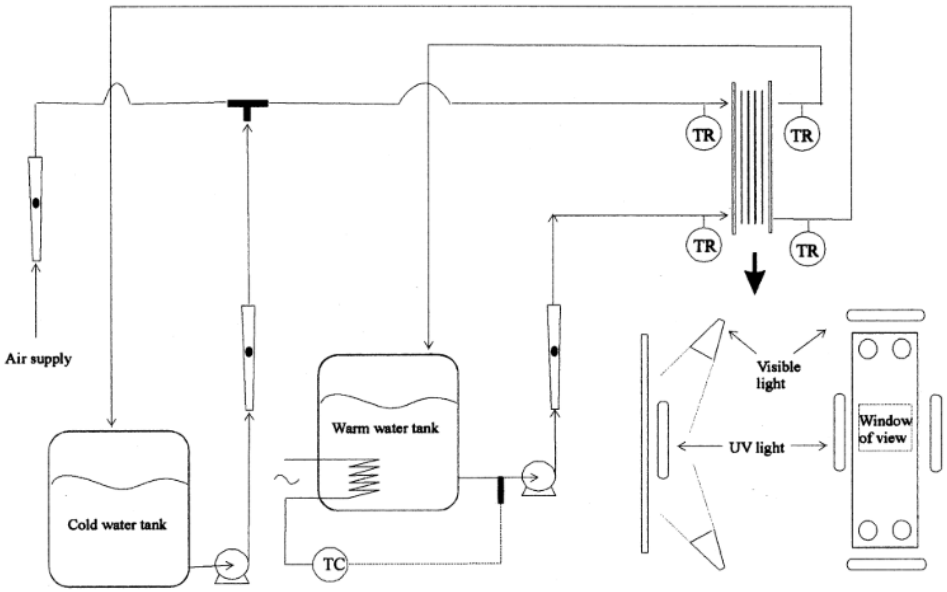

Figure 2.9: Schematic view of the visualization set-up of Vlasogiannis *et al.* [11] (2002).

Tribbe and Müller-Steinhagen [12] (2001) present a flow pattern analysis for an air-water flow in a plate heat exchanger. Visualization is made possible by two polyester plates, see figure 2.10. The heat exchanger consists of one channel. Images are created with a Kodak Ektapro 4340 high-speed video camera.

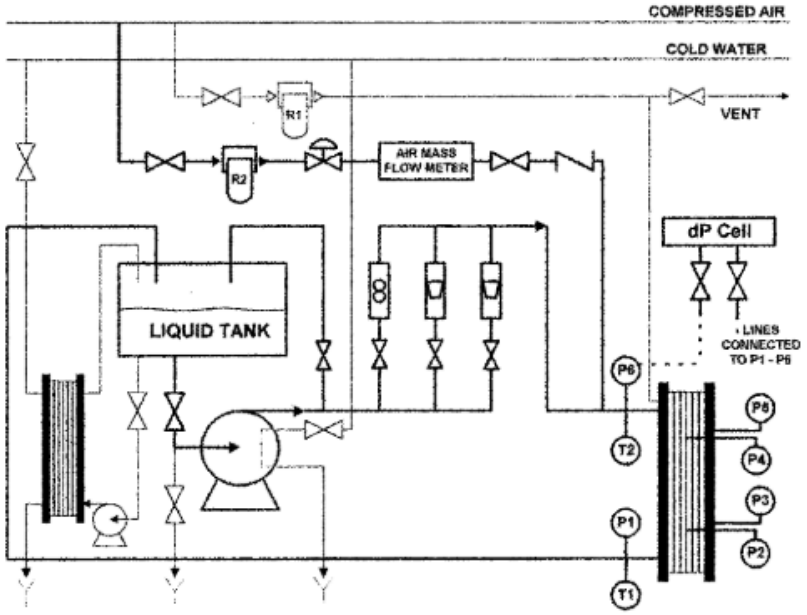

Figure 2.10: Schematic view of the visualization set-up of Tribbe and Müller-Steinhagen [12] (2001).

Table 2.1 gives an overview of the visualization sections of previous flow visualization studies.

Table 2.1: Overview of the visualization sections of previous flow visualization studies

Author	**Work. fluid**	**Chan-nels**	**Visualization method**	**Transp. plate thickness**	**Transp. material**	**Lighting**	**Camera**
Grabenstein et al. (2017)	Air/water R365	1	Corrugated gap, side view		Polyur-ethane	Halogen headlights	
Koyama et al. (2014)	FC-72	1	Transparent end covers	40 [mm]	Acrylic		Nikon D800
Arima et al. (2011)	NH_3/water	1	Sight glasses		Glass	250[W] cold lamp	Pentax *istD
Winkelmann (2010)	Air/water	1	One transparent end plate, hole in frame	40 [mm]	Plastic	From the front	high speed video camera (500 frames per second)
Nilpueng and Wongwises (2010)	Air/water	1	One transparent plate, two windows	30 [mm]	Polyur-ethane		Samsung Digimax v3
Jassim et al. (2006)	R134a	1	Three types of transparent plates	12.7 [mm] (before machining)	PVC	Strobo-scope	Digital
Asano et al. (2005)	Air/water	single/ multi	Neutron radiography				
Vlasogiannis et al. (2002)	Air/water	6	Transparent end covers	30 [mm]	Plexiglass	UV- and visible light	RedLake Motion Scope PCI high-speed
Tribbe and Muller Steinhagen (2001)	Air/water	1	Transparent end covers	3 [mm]	Polyester	Light refraction	Kodak Ektapro 4340 high-speed

2.2. FLOW PATTERN MAPS

The Reynolds number (Re) is defined as the ratio between inertial forces and viscous forces in the flow and is used to predict the type of flow. It can be defined as

$$Re = \frac{G \cdot L}{\mu}, \tag{2.1}$$

where G is the mass flux in [kg/m^{2}s], L is the characteristic length scale in [m] and μ is the dynamic viscosity of the fluid in [Pa s]. The mass flux G can be calculated by using the following equation

$$G = \frac{\dot{m}}{A_f \cdot N_{ch}}, \tag{2.2}$$

where $\dot{m}$ is the mass flow, A_f is the flow passage area and N_{ch} is the number of channels in the plate heat exchanger. The flow passage area is given by

$$A_f = L_w \cdot d_g, \tag{2.3}$$

where L_w is the effective width of the heat transfer plate. Figures 2.12a and 2.12b show the geometric parameters of corrugated heat transfer plates in a plate heat exchanger, including the channel gap d_g.

The characteristic length scale L for a corrugated channel in a plate heat exchanger is the hydraulic diameter d_h. For plate heat exchangers, the hydraulic diameter d_h is defined as

$$d_h = \frac{d_{eq}}{\Phi} = \frac{2 \cdot d_g}{\Phi}, \tag{2.4}$$

where Φ is the surface enhancement factor, which is defined as the ratio between the effective heat transfer area and the projected heat transfer area of a heat transfer plate. This is further discussed in section 3.5.

The Froude number (Fr) is defined as the ratio of the flow inertia to the external field. It is generally defined as

$$Fr = \frac{U_0}{\sqrt{g \cdot L}}, \tag{2.5}$$

where U_0 is the characteristic flow velocity, g is the gravitational acceleration constant and L is the characteristic length scale.

During the condensation of the working fluid in the condenser, multiple types of flow appear (flow patterns). Figure 2.11 shows the four main flows patterns observed for downward two-phase flow in plate heat exchangers (which is the case in the condenser of the OTEC-cycle).

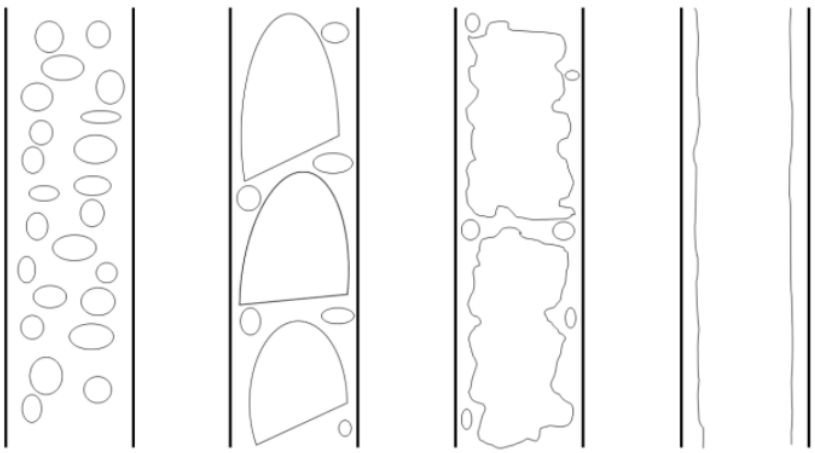

Figure 2.11: Representations of the four main flow patterns observed for downward two-phase flow in plate heat exchangers. From left to right: bubbly flow, slug flow, churn flow and film flow. From Tao *et al.* [13].

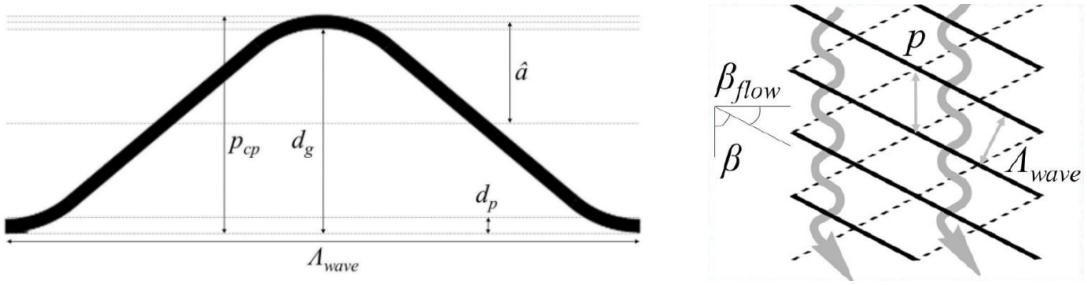

(a) p_{cp}: compressed plate pitch, d_p: plate thickness, d_g: channel gap, $\hat{a}$: corrugation amplitude, Λ_{wave}: wave length.

(b) β: Chevron angle, p: corrugation pitch.

Figure 2.12: Geometric parameters of corrugated heat transfer plates. Based on Winkelmann (2010) [7].

A flow pattern map shows for which conditions certain flow patterns occur. For future research, it is important that all the relevant parameters that influence the flow pattern are clearly reported in this research, so comparisons can be made. Tao *et al.* [13] (2018) state that the incomplete reporting of previous research has limited the progress of the research on downward two-phase flow, which needs to be prevented in future research.

Oshinowo and Charles [35] proposed to base the axes of the flow pattern maps for downward two-phase flow in tubes on $Fr_{TP,ver}/\Lambda^{0.5}$ and $R_v^{0.5}$.

The Froude number for vertical two-phase flow is given by

$$Fr_{TP,ver} = \frac{(U_G + U_L)^2}{g \cdot d_h}, \tag{2.6}$$

where U_G is the superficial gas phase velocity of the fluid and U_L is the superficial liquid phase velocity of the fluid. These velocities are respectively given by

$$U_G = \frac{\dot{V}_G}{A_f}, \tag{2.7}$$

and

$$U_L = \frac{\dot{V}_L}{A_f}, \tag{2.8}$$

where $\dot{V}_G$ is the gas phase volume flow, $\dot{V}_L$ is the liquid phase volume flow and A_f is the flow passage area.

Λ is a property modifying parameter, which is defined as a function of the liquid phase properties relative to those of water under the same conditions:

$$\Lambda = \frac{\frac{\mu_L}{\mu_{water}}}{\left[\frac{\rho_L}{\rho_{water}}\left(\frac{\sigma_L}{\sigma_{water}}\right)^3\right]^{1/4}}, \tag{2.9}$$

where ρ is the density of the fluid and σ is the surface tension of the fluid.

The gas to liquid velocity ratio R_v is defined as

$$R_v = \frac{U_G}{U_L}. \tag{2.10}$$

An example of a flow pattern map based on $Fr_{TP,ver}/\Lambda^{0.5}$ and $R_v^{0.5}$ is shown in figure 2.13.

Tao *et al.* [13] (2018) propose to adapt the flow pattern map by Oshinowo and Charles [35] by basing the axes of the flow pattern maps for downward two-phase flow in plate heat exchangers on Re_L and $Fr_{TP,hor}/\Lambda^{0.5}$.

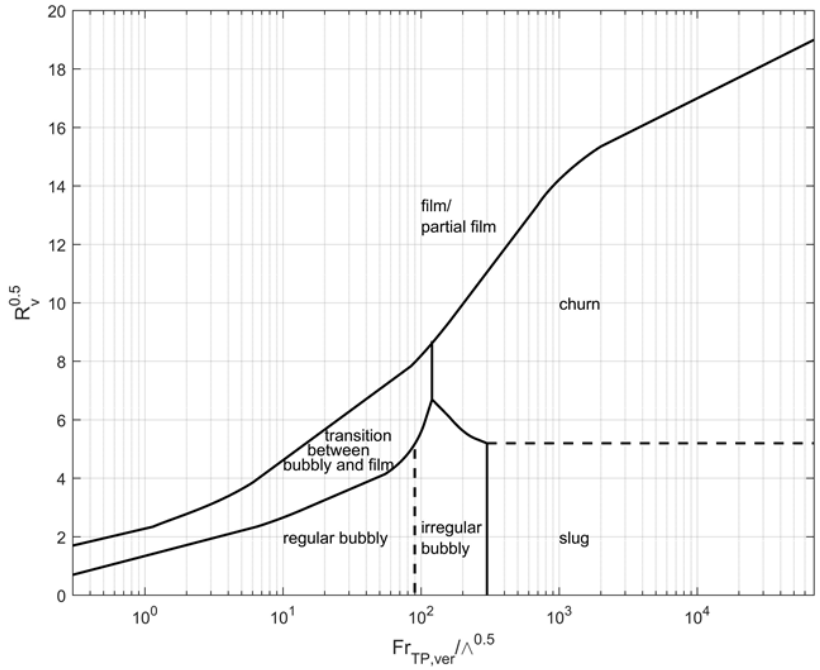

Figure 2.13: A simplified flow pattern map of two-phase flow in plate heat exchangers, based on $Fr_{TP,ver}/\Lambda^{0.5}$ and $R_v^{0.5}$. From Tao *et al.* [13].

The Froude number for horizontal two-phase flow is given by

$$Fr_{TP,hor} = \frac{x \cdot G}{\left[g \cdot d_h \cdot \rho_G(\rho_L - \rho_G)\right]^{0.5}}, \tag{2.11}$$

where x is the vapour quality of the flow.

The liquid phase Reynolds number is defined as

$$Re_L = \frac{G \cdot (1-x) \cdot d_h}{\mu_L}. \tag{2.12}$$

An example of a flow pattern map based on Re_L and $Fr_{TP,hor}/\Lambda^{0.5}$ is shown in figure 2.14. In the flow pattern map proposed by Tao *et al.* [13], the different types of flow are more clearly distinguishable compared to the flow pattern map proposed by Oshinowo and Charles [35].

Thus, to construct flow pattern maps of the two-phase flow in the condenser of an OTEC-cycle, it is essential that the geometric parameters of the heat exchanger plates, such as the channel gap d_g, the effective width of the heat transfer plates L_w and the surface enhancement factor Φ are clearly reported.

The influence of the mass flux G and the vapour fraction x is also stressed by Tao *et al.* [13] and Tao *et al.* [36]. The influence of these parameters on the flow patterns is clearly shown in figure 2.15, which shows a flow pattern map based on G and $x^{0.5}$ with data from Tribbe and Müller-Steinhagen [12].

Lastly, Tao *et al.* [13] stress that the difference in the type of distribution of the flow over the heat exchanger plates has lead to deviations in the flow pattern maps of previous research. The type of distribution of the flow should also clearly be reported.

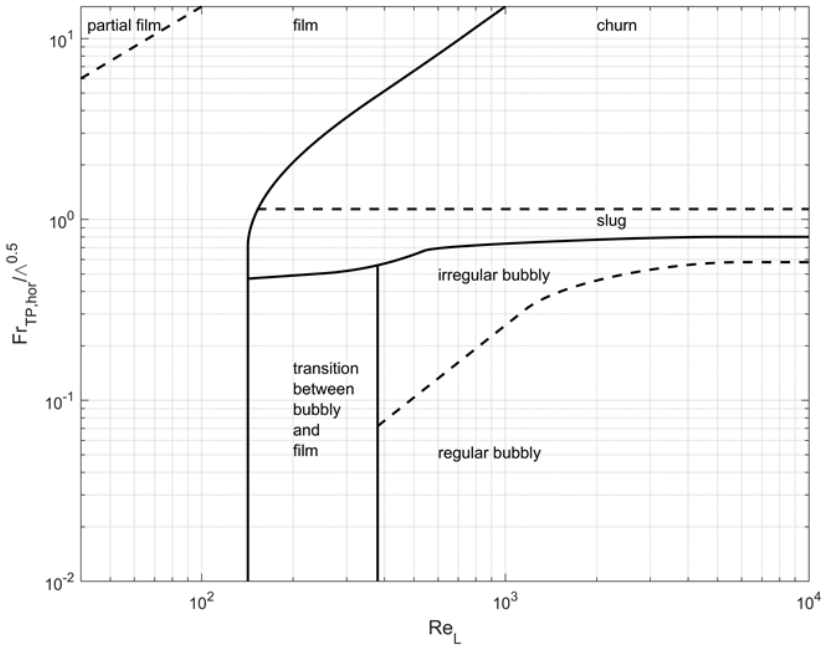

Figure 2.14: A simplified flow pattern map of two-phase flow in plate heat exchangers, based on Re_L and $Fr_{TP,hor}/\Lambda^{0.5}$. From Tao *et al.* [13].

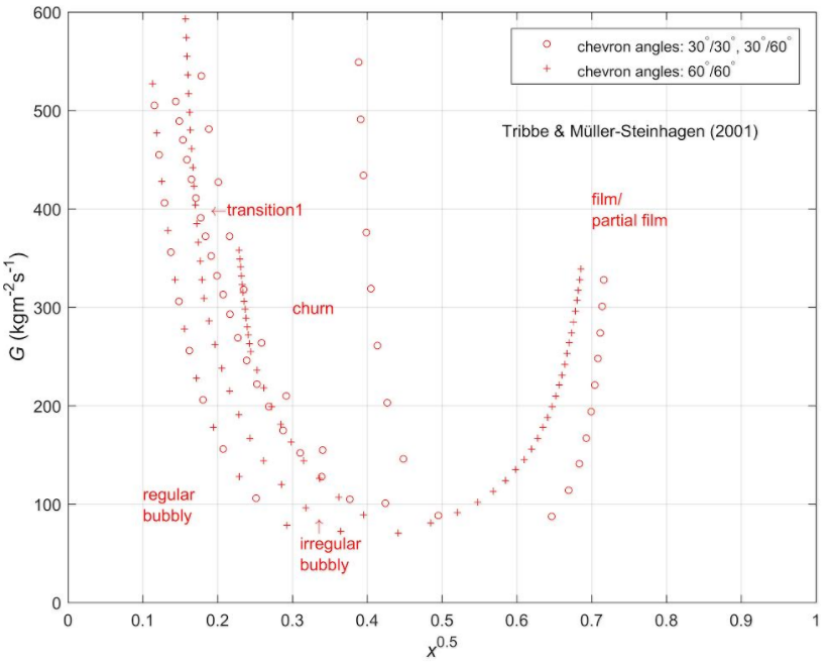

Figure 2.15: A simplified flow pattern map of two-phase flow in plate heat exchangers, based on G and $x^{0.5}$. From Tao *et al.* [13].

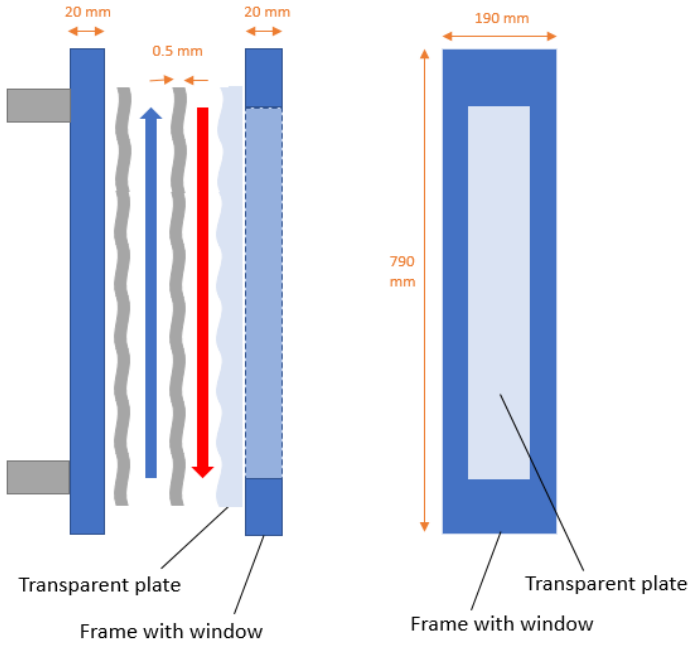

Figure 2.16: Simplified side and front view of a possible single channel visualization set-up

2.3. LOCAL TEMPERATURE MEASUREMENTS

In the previous section, the importance of the mass flux G and the vapour fraction x regarding the design flow pattern maps for two-phase flow in plate heat exchangers is stressed.

Sarraf *et al.* [37] confirm from experiments that the local heat flux q varies significantly along the flow direction of the plate heat exchanger during condensation. The averaged vapour quality x_{av}, which has been used in most previous studies, may not reflect the physical process. Local temperature measurements are needed to locally determine the vapour quality.

Tao *et al.* [36] conclude that the mass flux G and the vapour fraction x effect the transition between the flow patterns and additional local temperature measurements are required to design heat transfer models and flow pattern maps for ammonia(-water) in plate heat exchangers.

2.4. PROPOSED METHODS

Taking the previous review of related studies in sections 2.1, 2.2 and 2.3 it has been decided to take the following steps to get a better understanding of the transport phenomena in plate heat exchangers.

Flow patterns Regarding the observation of flow patterns by visualization of the flow, a gasketed heat exchanger should be used as condenser, as this allows modifications to be made. This way, one of the corrugated endplates of the gasketed heat exchanger can be replaced by a 30 [mm] transparent plate with identical corrugation pattern. The required thickness needs to be checked by calculations (see section 3.7.2). The required material of the plate needs to be investigated (see section 3.7.1), as only Arima *et al.* [6] (2011) used ammonia(-water) and that study used non-corrugated glass sight glasses for visualization. A window should be created in the pressure plate of the gasketed heat exchanger, similar to the visualization section by Winkelmann [7] (2010). Figure 2.16 shows a simplified sketch of the proposed design. The visualization section will be performed for a single channel set-up (see appendix A for the multichannel visualization section designs).

The correct type of lighting and camera can only be determined after certain test visualization experiments are performed. Clear reporting of the channel gap d_g, the effective width of the heat transfer plates L_w, the surface enhancement factor Φ, the mass flux G and the vapour fraction x is essential.

Local temperature measurements In relation to the temperature distribution, local temperature measurements in the condenser can be done by placing miniature temperature sensors along the corrugated endplate, which fits in the corrugation gaps. Thus, this type of measurements requires a modifiable plate heat exchanger as well.

3

EXPERIMENTAL SET-UP

In this chapter, the experimental set-up used for this research, along with the implemented modifications for this research, will be discussed. The experimental set-up is a small scale OTEC cycle prototype (OTEC-demo) to which the new condenser was added. The added condenser is a gasketed plate heat exchanger, which makes it possible to vary the amount of plates and to use self-fabricated plates, for visualization purposes. In order to implement the condenser, a series of modifications needed to be done.

3.1. OTEC-DEMO BASE SET-UP

Together with the Delft University of Technology, Bluerise B.V. has constructed a small-scale version of the OTEC-plant, located in the Process & Energy lab. It is used to test the performance of the OTEC-cycle and to optimize the relevant output. The results will be used for the design of a larger-scale OTEC-plant.

3.1.1. KALINA CYCLE

The thermodynamic process used in the OTEC-demo is the Kalina cycle (see figure 3.1) for mixtures or the Organic Rankine Cycle (ORC) for pure fluids. This way, the advantages and disadvantages of using a mixture instead of a pure working fluid can be tested. In this case, an ammonia-water mixture is used as the working fluid. Goudriaan (2017) [2] and Kuikhoven (2017) [3] performed an analysis of the differences between using ammonia and ammonia-water as a working fluid. They concluded that the benefits of an ammonia-water mixture actually are not larger than the disadvantages of an ammonia-water mixture compared to pure ammonia for the small scale OTEC-demo set-up.

The Kalina cycle differs from an ORC as it has extra components. When using an ammonia-water mixture, a relatively large part of the working fluid is not fully evaporated as the water has a higher boiling point. In order to separate the vapour and the liquid ammonia-water mixture generated after the evaporator, a separator is used. This prevents the liquid to flow through the turbine, which could lead to mechanical damage in the turbine and a lower efficiency of the turbine. A recuperator is used to pre-heat the cold liquid working fluid with the liquid outlet flow of the separator before it enters the evaporator. At the inlet of the condenser, the ammonia vapour, which went through expansion in the turbine, is mixed with liquid ammonia-water mixture from the outlet of the recuperator.

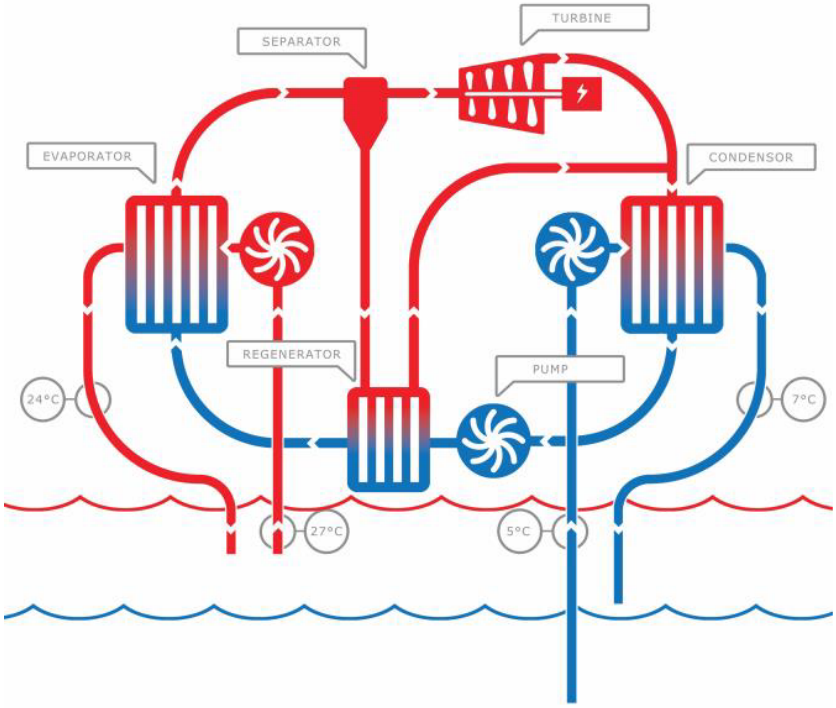

Figure 3.1: An OTEC-cycle based on the Kalina cycle principle (image courtesy of Bluerise).

3.1.2. COMPONENTS

Figure 3.2 shows the physical OTEC-demo test facility, showing the relevant components. The set-up contains all the components of the Kalina cycle, as well as sensors at all the relevant positions.

PUMPS

The experimental set-up contains one reciprocating displacement pump, which is used to create a working fluid flow (indicated by the number 1 in figure 3.2) and two centrifugal pumps, used to pump around water stored in tanks. The water in these tanks represents the ocean water. The hot water pump is indicated by the number 2 and the cold water pump by the number 3.

HEAT EXCHANGERS

Three heat exchangers are used in the OTEC-demo, an evaporator (number 4), a condenser (number 5) and a recuperator (number 6). All of these are plate heat exchangers. In the evaporator, the working fluid is evaporated by using the heat from the hot water and in the condenser the working fluid is condensed by transferring heat to the cold water. The recuperator is used to increase the efficiency by pre-heating the subcooled working fluid before the evaporator.

SEPARATOR AND TURBINE

The separator, indicated by the number 7, separates the vapour and the liquid parts of the working fluid. No liquid flow should go to the turbine (indicated by the number 8), as this could both lead to mechanical damage and a lower efficiency.

Figure 3.2: Image of the OTEC-demo, with the various components.

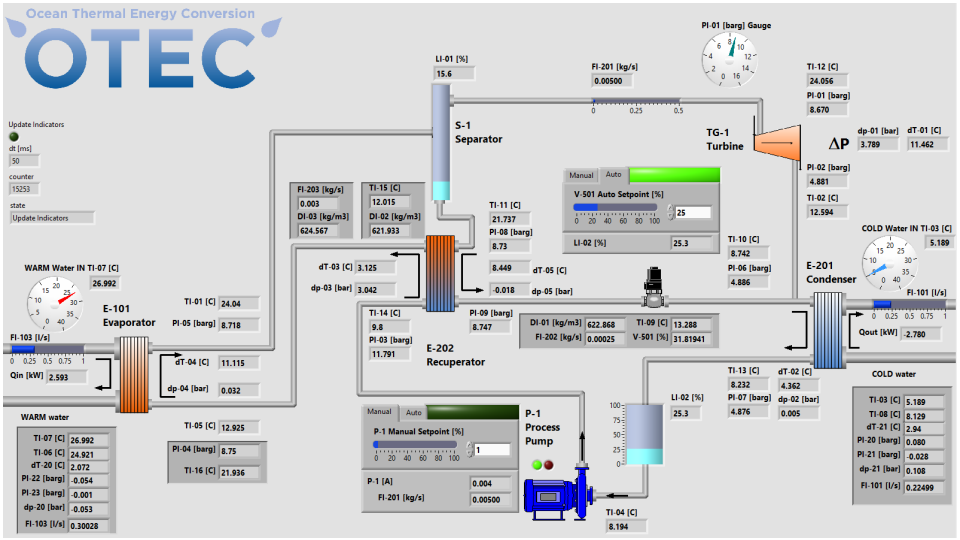

Figure 3.3: Overview of all the sensor values in Labview (image courtesy of Bluerise).

3.1.3. CONTROL SYSTEM

Using a LabView interface, the measured values at the corresponding sensor positions are shown (see figure 3.3). The measured values are also plotted continuously over time. The control system fixes the input values on the desired points. It also makes sure the pressure doesn't exceed 12 [bar] in the system and it controls a valve between the recuperator and the condenser.

3.2. OTEC-DEMO EXTENSION

A number of modifications on the base set-up were required for this research. A gasketed plate heat exchanger, which can be used as a condenser, needed to be implemented, without losing the possibility of using the set-up in the old way. By using a gasketed plate heat exchanger, the amount of plates can be varied,

so both single and multichannel experiments can be done. Also, the plates can be replaced by custom made transparent plates for visualization experiments. Furthermore, temperature sensors needed to be placed locally along the plates.

The gasketed plate heat exchanger needed to be connected to the base set-up with a bypass to the existing brazed heat exchanger. Some new sensors were required to measure inlet and outlet pressures, temperatures and flows for the new condenser. A physical extension of the set-up was made to fit all the new components. Figure 3.4 shows the P&ID for the OTEC Demo installation with the extended part.

3.2.1. WORKING FLUID SIDE

As shown in Figure 3.4, a bypass is created by implementing 3-way valves into both the liquid line and the gas line of the working fluid side. These lines will then be connected in a similar way to the existing mixing set-up, right before the inlet of the heat exchanger (see figure D.1 in Appendix D and figure 3.6). The liquid line with a diameter of 8 [mm] goes through the vapour line (the diameter of the vapour line is increased from 12 [mm] to 16 [mm] so the liquid line fits through) and enters the heat exchanger through small holes of 0.8 [mm] at the end of the tube, creating a liquid spray distribution over the plates. This way, the liquid is mixed with the vapour at the inlet port of the heat exchanger. Figure 3.5 shows the liquid spray tube. The SS-8M0-6 component (indicated by the red underline) in the absorber set-up of the gasket heat exchanger (see figure 3.6) allows the liquid line to be removed, so the distribution of the liquid flow entering the heat exchanger can be changed, by adjusting the position and diameter of the holes.

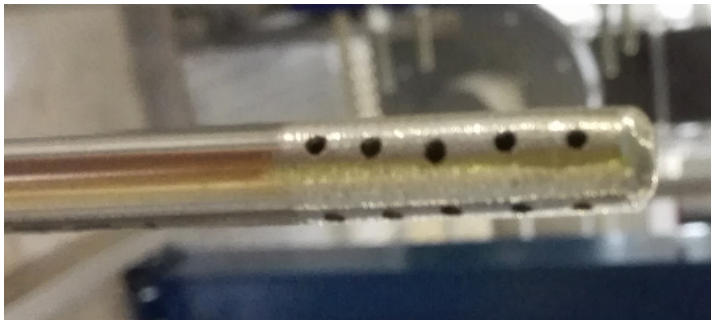

Figure 3.5: The liquid spray tube at the end of the liquid line.

At the outlet of the gasketed heat exchanger on the working fluid side, a new temperature sensor and a new pressure sensor are implemented. The outlet of the gasketed heat exchanger is connected to the inlet of the existing brazed heat exchanger, so the latter can be used as a subcooler. This line will contain a valve, because it should still be possible to use the system in the old way, in which only the brazed heat exchanger is used for the condensation process.

Figure 3.7 shows how the set-up of the old absorber will be changed in order to connect the gasketed heat exchanger. The system can still be used in the old way by closing the 2-way valve (indicated by the number 1) and opening only the outlet of the 3-way valve (indicated by the number 2) in the vapour line which goes to the brazed heat exchanger. For the mode in which the flow is bypassed to the new gasketed heat exchanger, the 2-way valve will be opened and the 3-way valves (indicated by the numbers 2 and 3) will direct the flow to the new gasketed heat exchanger.

3.2.2. WATER SIDE

For the water side, the line is split right before the flow meter, where the new line contains a valve so the system can still be used in the old way. This line is then connected to the water side inlet of the brazed plate heat exchanger, after the sensors. Measuring the thermodynamic data of this flow is not that important for the subcooler. The sensors will be used for the water line which goes to the gasketed heat exchanger instead. Using a three way valve, the line is split. At the water side outlet of the gasketed heat exchanger, a pressure sensor and a temperature sensor are implemented.

Figure 3.8 shows the new arrangement of the water side inlet and figure 3.9 shows the arrangement of the

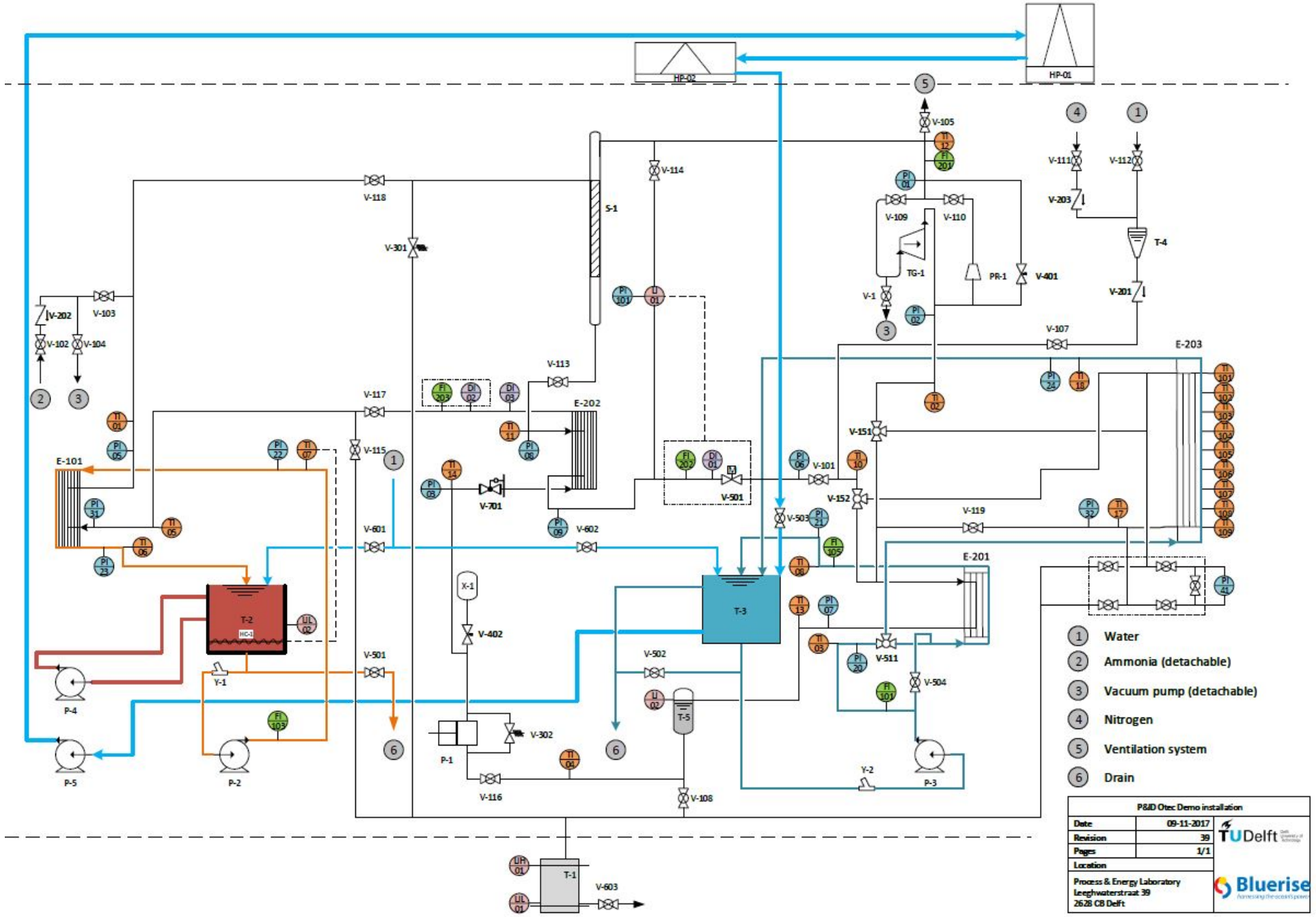

Figure 3.4: P&ID for the OTEC-demo set-up with the extended part. The added lines and components are indicated by the green colour.

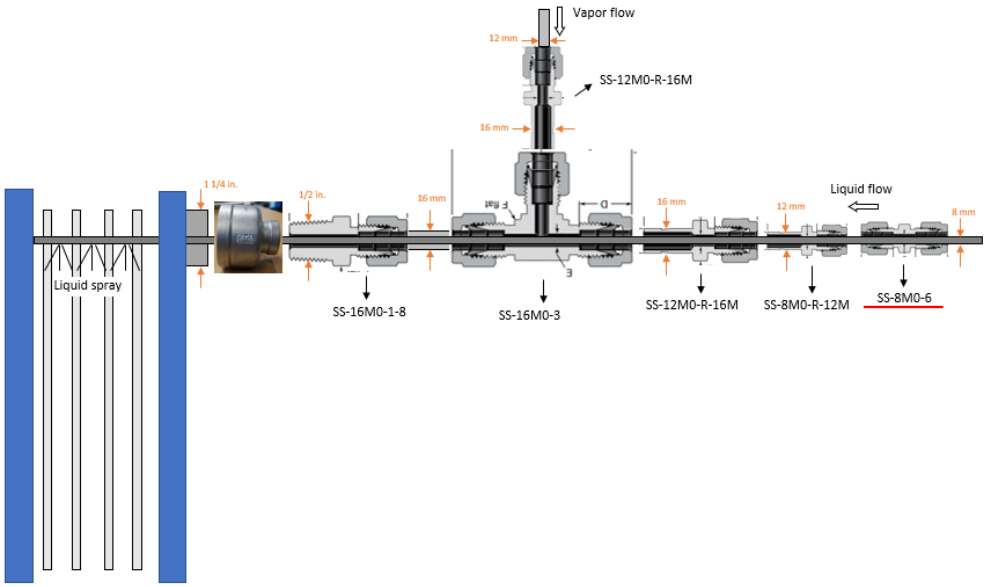

Figure 3.6: Arrangement of the new mixer of the gasketed plate heat exchanger, including the Swagelok® part numbers.

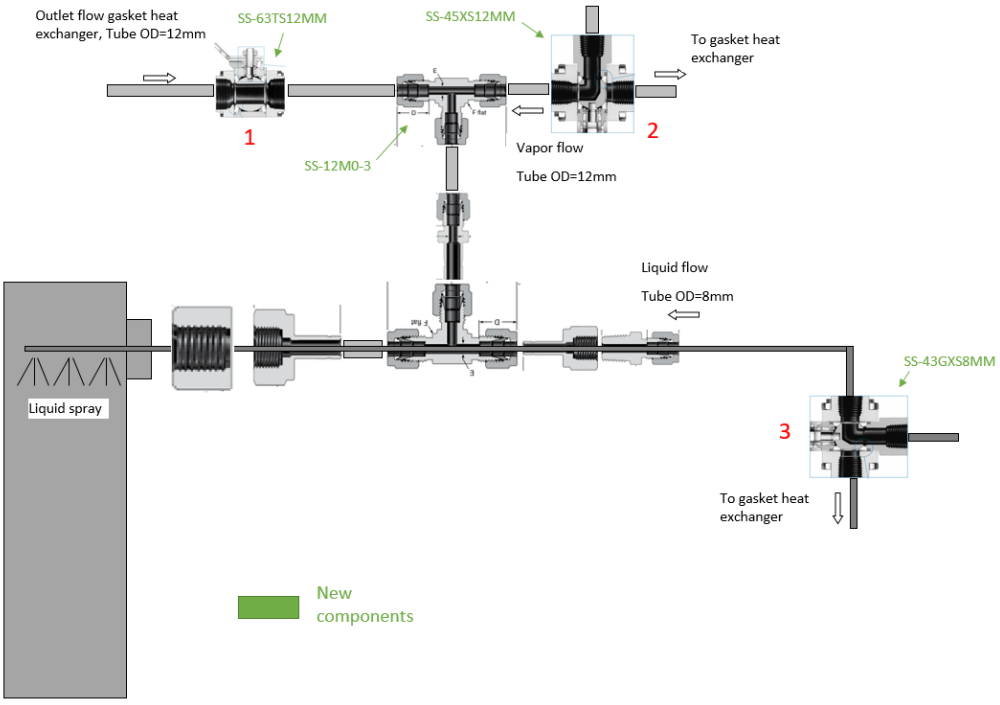

Figure 3.7: Arrangement of the modified mixer of the brazed plate heat exchanger, including the Swagelok® part numbers.

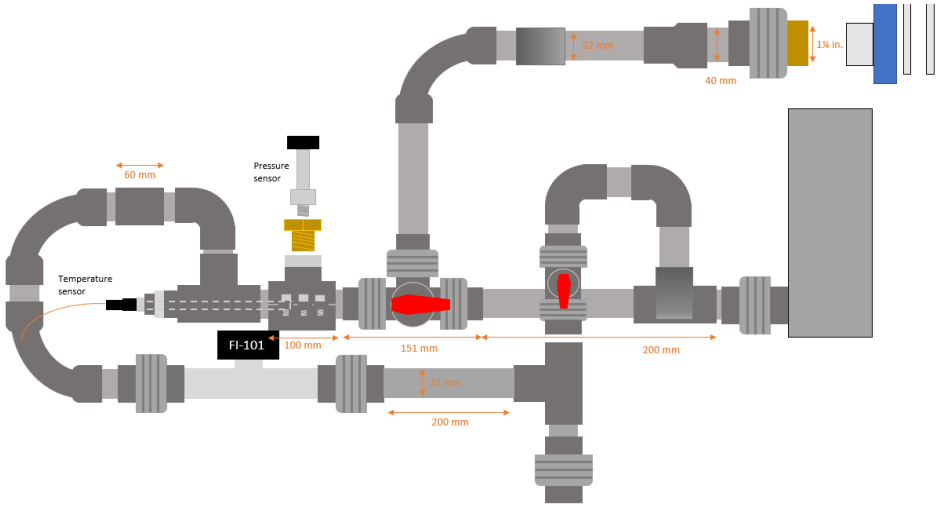

Figure 3.8: Practical drawing of the arrangement of the water side inlet of the new condenser.

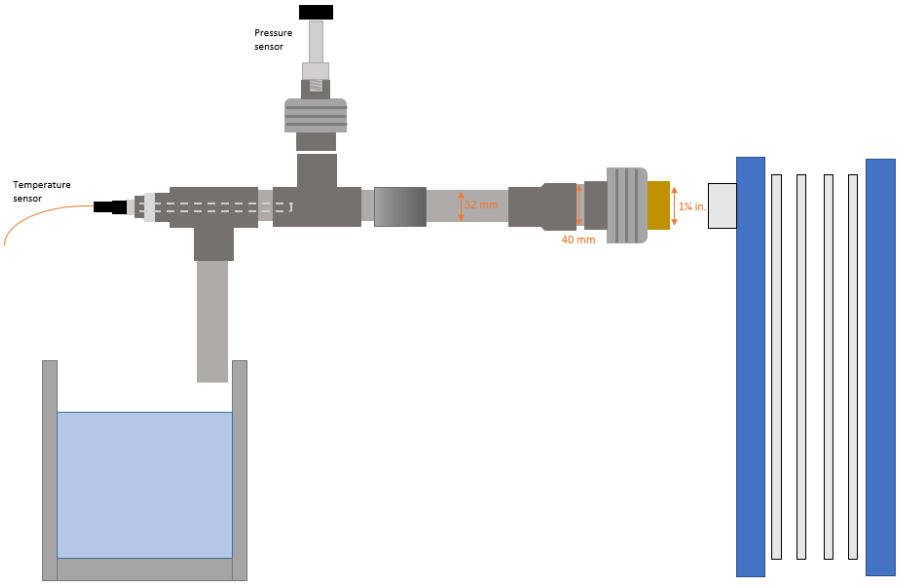

Figure 3.9: Practical drawing of the arrangement of the water side outlet of the new condenser.

new water side outlet. The situation before the OTEC-demo extension modification is shown in Appendix D.

Table 3.1: Sensors added to the OTEC-demo

Sensor type	**No.**	**Sensor name**	**Output signal**	**Measuring range**	**Accuracy**	**Position(s) with respect to gasketed heat exchanger**
Pressure differential	1	Siemens SITRANS P500	4-20 [mA], HART	0 .. 15 [kPa]	≤ 0.03%FS	Working fluid side
Temperature	2	TC Direct Pt-100 precision thermometer	RTD	-5 .. 250 [$^{\circ}C$]	±0.06[$^{\circ}C$]	Water/working fluid side outlet
Pressure	1	TC Direct Industrial Vacuum Pressure Transmitter	4-20 [mA]	-1 .. 2.5 [bara]	±0.5% FS	Water side outlet
Pressure	1	Keller Highly Precise Pressure Transmitters Series 33 X	Digital, Modbus	0.8 .. 1000 [bara]	±0.05%FS	Working fluid side outlet
Flow	1	MAG-VIEW Magnetic Flow Meter [1 .. 60 lpm, 4 .. 20 mA]	4-20 [mA]	1 .. 60 [lpm]	±1.5% RD, ±0.3% FS	Water side inlet (brazed hex)
Temperature (local)	9	TC Direct Pt-100 miniature thermometer	RTD	-75 .. 350 [$^{\circ}C$]	±0.06[$^{\circ}C$]	Along end plate

3.2.3. ADDED SENSORS

Table 3.1 shows the sensors that were added to the set-up, including its accuracies. The accuracies of the existing sensors in the OTEC-demo set-up were investigated by Veijer [38].

PRESSURE DIFFERENCE

The pressure differential sensor is used to measure the pressure drop over the new condenser. The accuracy of the pressure differential sensor is a percentage of the measuring range. For this reason, the measuring range was selected to match the expected operating range. From earlier experiments with the brazed heat exchanger, the pressure drop of the brazed heat exchanger was found to be around 2 [kPa] (see figure B.3 in Appendix B). It can be expected that the gasketed heat exchanger will have a higher pressure drop than the brazed heat exchanger. From the difference in geometry (see chapter 4 for details) and operating conditions (will be discussed later) between both heat exchangers, the pressure drop can be predicted to be approximately five times higher in the gasketed heat exchanger compared to the brazed heat exchanger, taking results from Kuo et al. (2005) [27] into account.

ABSOLUTE PRESSURE

At the outlet of the water side of the gasketed heat exchanger, a new pressure sensor needed to be installed. The same pressure sensor as all the other pressure sensors on the water side in the entire OTEC-demo was chosen, as the conditions (± 0.5 [bara]) are similar here. On the working fluid side, a new sensor was needed at the outlet of the gasketed heat exchanger. This sensor has a high accuracy (see table 3.1).

FLOW

Due to limited space at the water side inlet of the brazed heat exchanger, the new flow sensor was placed at the outlet. The measuring range corresponds to cold water flows in earlier measurements (see Appendix B for details).

TEMPERATURE

At the outlet of the gasketed heat exchanger on the water and working fluid side, the same temperature sensors are implemented as the already existing ones in the set-up (see 3.1), as these have proven to be reliable. The local temperature sensors will be discussed in section 3.6.

Figure 3.10: Image of the OTEC-demo, with the constructed extension. The red rectangle shows the location of the new condenser.

3.3. SPECIFICATIONS OF THE NEW CONDENSER

The TL3BFG10 gasketed plate heat exchanger by Alfa Laval ™ is used for the condensing of the working fluid (see figure 3.11). The heat exchanger consists of ten alloy 316 corrugated heat transfer plates, two epoxy painted steel pressure plates, some bolts and four pipe connections. The hot and cold streams in the TL3BFG10 flow in counter-current direction.

Figure 3.11: The TL3BFG10 plate heat exchanger [14].

3.3.1. CONDENSER DIMENSIONS

Figure 3.12 shows the dimensions of the TL3BFG10 plate heat exchanger.

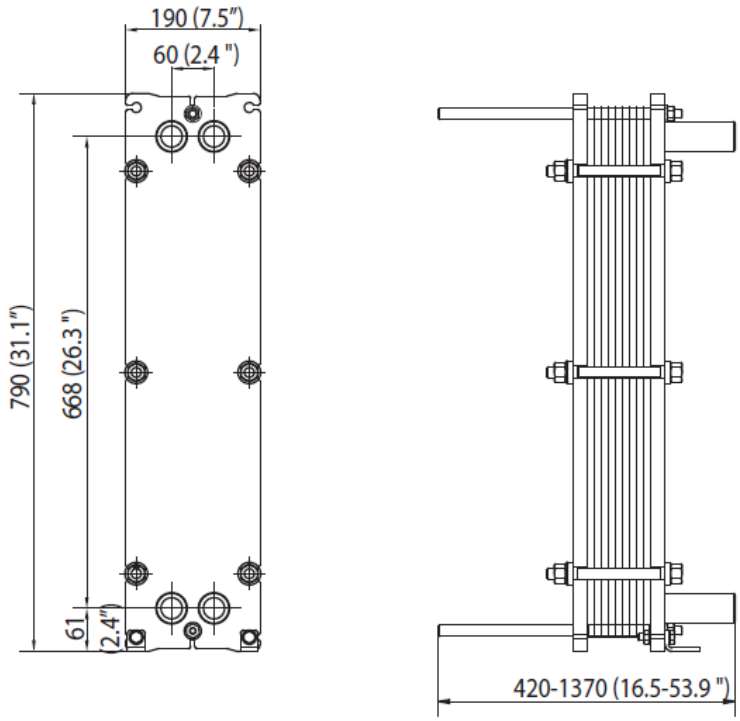

Figure 3.12: Dimensions in mm (inches) of the TL3BFG10 plate heat exchanger [14].

The pressure plates of the TL3BFG10 are 20 [mm] thick and the heat transfer plates are 0.58 [mm] [1] thick.

3.3.2. PLATE GEOMETRY

Figure 3.13 shows an endplate of the gasketed plate heat exchanger. In section 2.2 the importance of reporting the relevant parameters regarding the geometry of the plate is stressed. The following values were measured by hand:

- Corrugation wavelength $\Lambda_{wave} = 6.67$ [mm]
- Plate pitch $p_{cp} = 2.30$ [mm]
- Channel gap $d_g = 1.72$ [mm]
- Plate thickness $d_p = 0.58$ [mm]
- Corrugation pitch $p = 7.50$ [mm]
- Chevron angle $\beta = 63°$
- Effective length $L_p = 586$ [mm]
- Effective width $L_w = 95$ [mm]

The hydraulic diameter of d_h can now be determined using equation 2.4 and the flow passage area A_f can be determined from equation 2.3.

- The hydraulic diameter of $d_h = 2.99$ [mm]
- Flow passage area $A_f = 0.1634$ [mm]

[1] Alfa Laval mentions a thickness of 0.50 [mm] in their documentation. Measurements show the thickness is actually a bit higher.

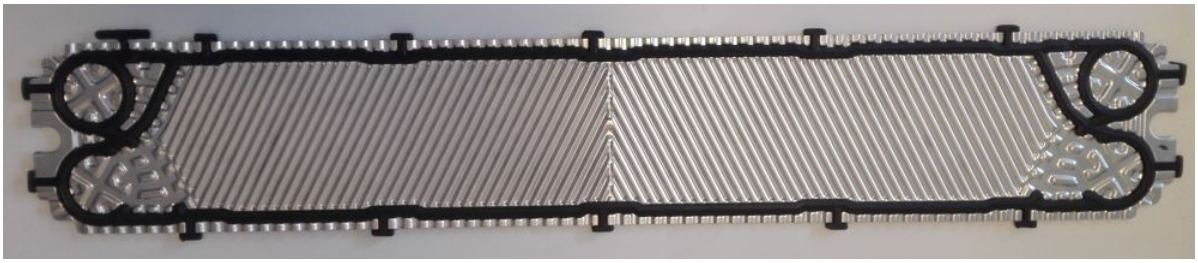

Figure 3.13: An endplate of the TL3BFG10 plate heat exchanger.

Table 3.2: Difference in geometric parameters between the brazed and the gasketed heat exchanger

Parameter	Symbol	Brazed heat exchanger	Gasketed heat exchanger
Plate width (port-to-port)	L_h	0.05 [m]	0.06 [m]
Plate length (port-to-port)	L_v	0.25 [m]	0.668 [m]
Port diameter	D_p	0.03 [m]	0.04 [m]
Plate thickness	d_p	0.0004 [m]	0.00058 [m]
No. channels hot	$N_{ch,h}$	9	5
No. channels cold	$N_{ch,c}$	8	4
No. plates effective	N_e	16	8
Thermal conductivity	κ	16.3 [W/m/K]	16.3 [W/m/K]
Compressed plate pitch	p_{cp}	0.00242 [m]	0.0023 [m]
Effective heat transfer area	A_e	0.4 [m^2]	0.537 [m^2]

3.4. CONDENSER COMPARISON

Before the OTEC-demo set-up extension, a brazed heat exchanger was used as a condenser. Table 3.2 shows the difference in geometric and material parameters between the brazed and the gasketed heat exchanger. The biggest differences lay in the port-to-port length and the number of plates (and thus channels) of the heat exchangers. The thermal conductivity κ is equal in both cases, as both plate heat exchangers contain 316 stainless steel plates. Another significant difference is the mirror plane of the corrugation. In the gasketed heat exchanger, the corrugated zone is mirrored over the horizontal mid plane, while the corrugated zone is mirrored over the vertical mid plane in the brazed heat exchanger (see figure 3.14).

3.5. EFFECTIVE HEAT TRANSFER AREA

For the brazed heat exchanger, the port-to-port length and width the effective length and width of the heat transfer area can be determined by subtracting the port diameter from the port-to-port dimensions (see figure 3.14).

The effective width and length are respectively given by

$$L_{w,brazed} = L_{h,brazed} + D_{p,brazed} \tag{3.1}$$

and

$$L_{p,brazed} = L_{v,brazed} - D_{p,brazed}. \tag{3.2}$$

With respect to the gasketed heat exchanger however, this method is not applicable (see figure 3.13). Due to the form of the gasket, the effective length of the gasketed heat exchanger plates would be overestimated if equation 3.2 would be used for the gasketed heat exchanger as well. Instead, the effective length and width of the gasketed heat exchanger are measured (see section 3.3.2).

The effective number of plates is equal to the total number of plates minus the two endplates,

$$N_e = N_t - 2. \tag{3.3}$$

Other important parameters of the corrugated plates are the corrugation wavelength $\Lambda_{wave} = p \cdot sin(\beta)$ and corrugation amplitude $\hat{a} = (p_{cp} - d_p)/2$ (see figure 2.12). For the gasketed heat exchanger, the surface

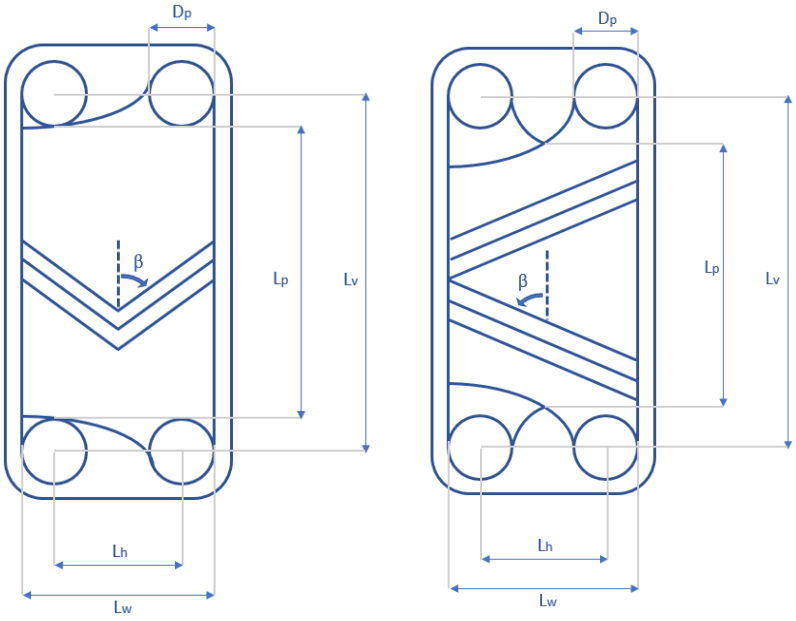

(a) The chevron angle definition for brazed heat exchanger

(b) The chevron angle definition for gasketed heat exchanger

Figure 3.14: Length, width and chevron angle of heat exchanger plates.

enhancement factor Φ can be approximated from these parameters by the following equation, by Martin (1996) [20],

$$\Phi(X) = \frac{1}{6}\left(1+\sqrt{1+X^2}+4\sqrt{1+X^2/2}\right) \tag{3.4}$$

where

$$X = 2\pi\hat{a}/\Lambda_{wave}. \tag{3.5}$$

The surface enhancement factor of the gasketed heat exchanger $\Phi_{gasketed}$ plates is found to be 1.149. Now, the total effective heat transfer area can be calculated, using

$$A_e = \Phi \cdot L_p \cdot L_w \cdot N_e. \tag{3.6}$$

From the documentation of the brazed heat exchanger, it's found that the effective area $A_{e,brazed}$ is equal to 0.4 [m^2] [2].
The effective heat transfer area of the gasketed heat exchanger becomes $A_{e,gasketed} = 0.512$ [m^2], when the maximum number of heat transfer plates is used. The ratio between the effective heat transfer area of the gasketed heat exchanger to the brazed heat exchanger in this case is

$$\frac{A_{e,gasketed}}{A_{e,brazed}} = 1.28 \tag{3.7}$$

The heat transfer area per plate is fixed for both heat exchangers. However, in the gasketed heat exchanger the amount of plates can be varied. To create equal total heat transfer area's for both heat exchangers, the gasketed heat exchanger should be equipped with 6 plates (8/1.28 = 6.25 plates, but the number of plates has to be an integer).

[2] Alfa Laval uses an empirically determined surface enhancement factor, which they don't want to share.

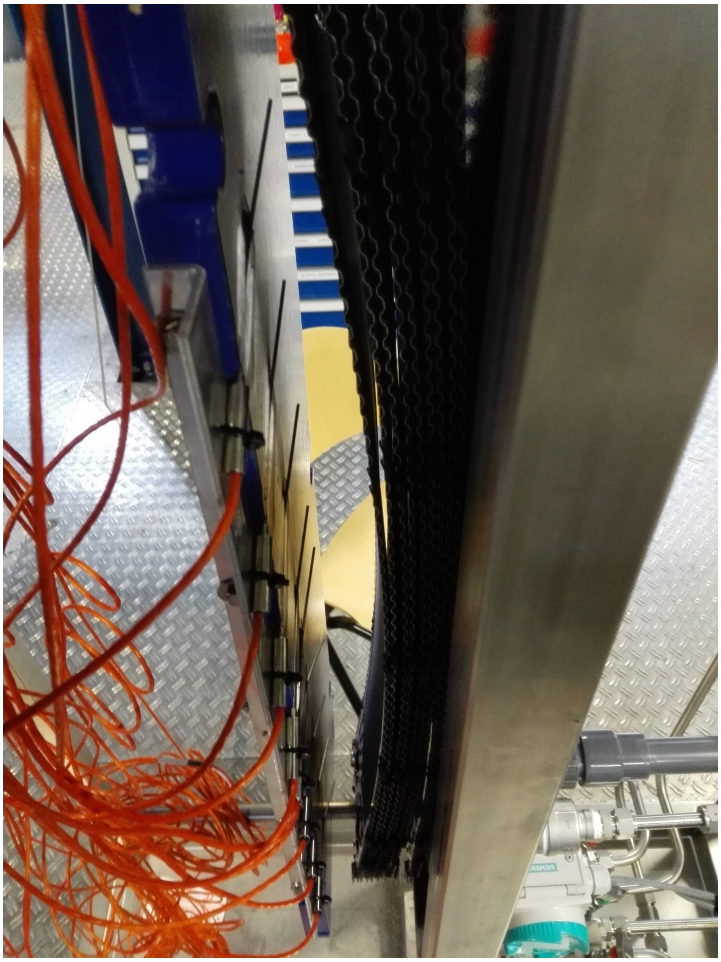

Figure 3.15: Arrangement of the Pt-100 temperature sensors placed between the pressure plate and the endplate of the gasketed plate heat exchanger.

3.6. LOCAL TEMPERATURE SENSORS ARRANGEMENT

In order to measure temperature profiles in the condenser, an arrangement was made in which nine temperature sensors were placed locally along the flow direction in the gaps between the pressure plate and endplate (see figure 3.15). The sensors are miniature versions (diameter d = 1.5 [mm]) of the Pt-100 temperature sensors placed at the outlet of the working fluid side and the outlet of the water side (see table 3.1). The miniature temperature sensors fit in the gaps of the corrugated endplate, which is shown in the simplified model in figure 3.16.

The miniature temperature sensors are insulated from the pressure plate by using insulating tape (see figure 3.17). The sensors are thermally connected to the corrugated plate by using a thermal paste of zinc. Both the zinc thermal paste (thermal conductivity κ_{zinc} = 116 [W/(m · K)]) and the stainless steel endplate (thermal conductivity steel κ_{ss} = 16.3 [W/(m · K)]) have a high thermal conductivity. This way, the difference between the measured temperature and the actual temperature of the flow is assumed to be small. Before doing experiments, all sensors have been calibrated.

Figure 3.18 shows the expected situation in the condenser during single channel experiments with ammonia(-water) as working fluid. The liquid working fluid flow (red) is expected to flow past the endplate of the channel, while the vapour working fluid flow (orange) is expected to flow past the heat transfer plate in the middle. The cold water flow (blue) will flow in the other channel. This arrangement will be further discussed in section 5.2.

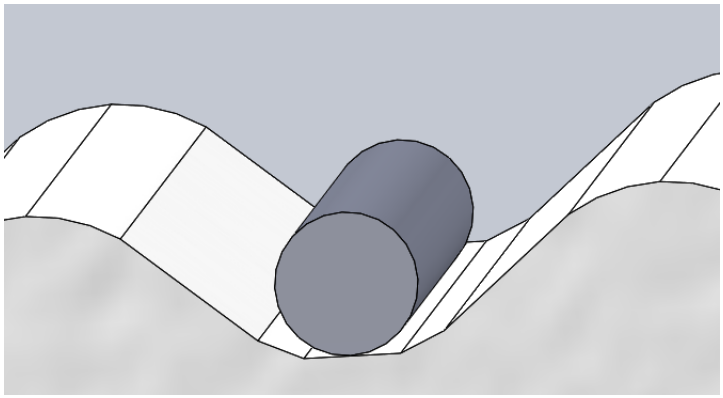

Figure 3.16: A simplified model of one of the temperature sensors placed against the corrugated endplate.

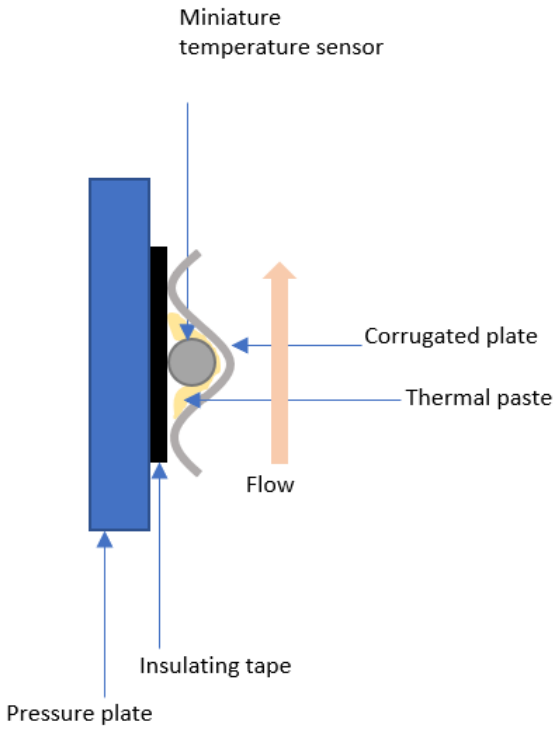

Figure 3.17: Cross section sketch of the position of the temperature sensors with regard to the pressure plate and the corrugated heat transfer plate.

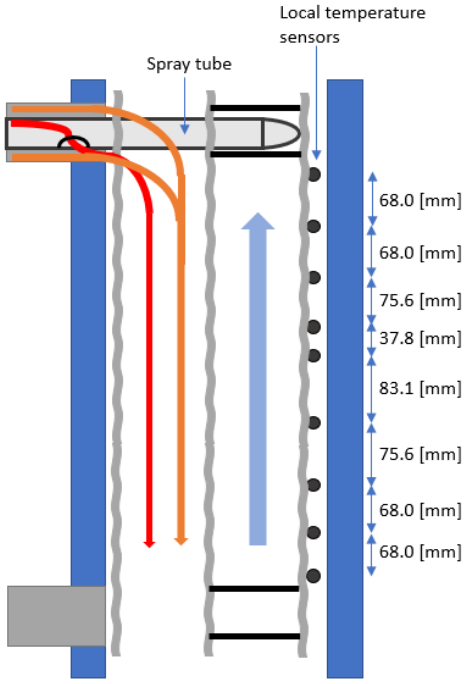

Figure 3.18: Arrangement of local temperature sensors along the endplate in the gasketed heat exchanger with single channel configuration. The image also shows the flow situation, where the liquid working fluid flow (red) enters the condenser via a hole in the spray tube and the vapour working fluid flow (orange) enters the condenser in the common way.

3.7. TRANSPARENT PLATE

The transparent plate has the following requirements (next to the obvious requirement of being transparent, which limits the options quite significantly already):

- Chemically compatible with ammonia.
- Able to withstand a pressure of max. 12 [bar].
- Possible to machine, to apply corrugation.
- Limited water absorption.

Because the plate will only be used for visualization tests and not for long-time operations, factors like creep resistance and flammability are not very relevant.

From the transparency requirement, the options are already quite limited. The available transparent polymers are perspex (PMMA), polycarbonate and clear PVC. Glass is not an option, because it's not possible to machine. PVC is also very hard to machine, since it is very soft.

3.7.1. CHEMICAL COMPATIBILITY WITH AMMONIA

As the working fluid, which will flow along the transparent plate, is ammonia or ammonia/water, a very important requirement is the chemical compatibility with ammonia of the material.

According to [39] polycarbonate is not chemically compatible with ammonia. Perspex however, is rated as 'Little or no damage after 30 days of constant exposure to the reagent.'

In Chemical Resistance of Thermoplastics (2012) [40], the rating of 2-9 (0-9 scale with 9 indicating the highest resistance) is assigned to the chemical resistance of perspex to ammonia. Since the operating temperature, which significantly influences the chemical resistance, is relatively low (Chemical Resistance of Thermoplastics (2012) [40] does not take the temperature into account), it's assumed the resistance is sufficient.

3.7.2. PLATE THICKNESS

In this section, the required plate thickness will be determined.

BENDING PLATE THEORY

The maximum deflection of the transparent plate can be calculated by using the theory of flexure of slabs (Westergaard [41]). The maximum deflection of the plate can be calculated by:

$$\delta_{max} = C \cdot (1 - \nu^2) \cdot \frac{P \cdot b^4}{E \cdot d_p^3} \tag{3.8}$$

where ν is the Poisson ratio of the material, E is the Young's modulus of the material, b the width of the plate, P is the pressure acting on the plate and d_p is the thickness of the plate.
The parameter C is given by:

$$C = \frac{0.032}{1 + \gamma^4} \tag{3.9}$$

where the aspect ratio $\gamma = b/a$ and a is the height of the window.

According to the CES Edupack 2016 [42] database the Young's modulus of perspex is 2.24-3.24 GPa. For these calculations, the lower limit of the Young's modulus will be used. The Poisson ratio is also obtained from the CES Edupack 2016 [42] database. The upper limit is used: $\nu = 0.403$. The width b of the window is 0.09 [m]. The height of the window will be $a = 0.55$ [m]. The pressure at the working fluid side can reach 12 [bar]. At the other side of the plate, the pressure is atmospheric. Hence, the pressure difference over the plate will be 11 [bar].

With these data, a plate with a thickness of $d_p = 30$ [mm] (which is used by Nilpueng and Wongwises [8] (2010) and Vlasogiannis *et al.* [11] (2002)) would only have a maximum deflection of $\delta_{max} = 0.032$ [mm]. A plate with a thickness of $d = 40$ [mm] (which is used by Winkelmann [7] (2010) and Koyama *et al.* [5]) (2014) would even have a maximum deflection of only $\delta_{max} = 0.014$ [mm].

3.7.3. TRANSPARENT PLATE MODEL

The plate was constructed by machining, at the central workshop of the Delft University of Technology. In order for this to be done, a 3D-model of the endplate needed to be constructed. The 3D CAD software Solidworks® was used to make the model (see figure 3.19).

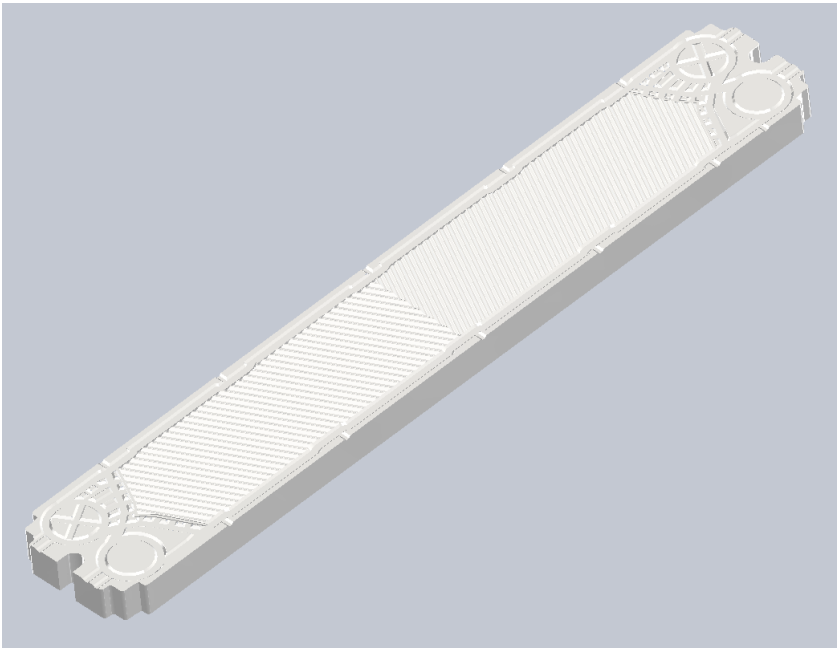

Figure 3.19: 3D CAD model of the transparent endplate.

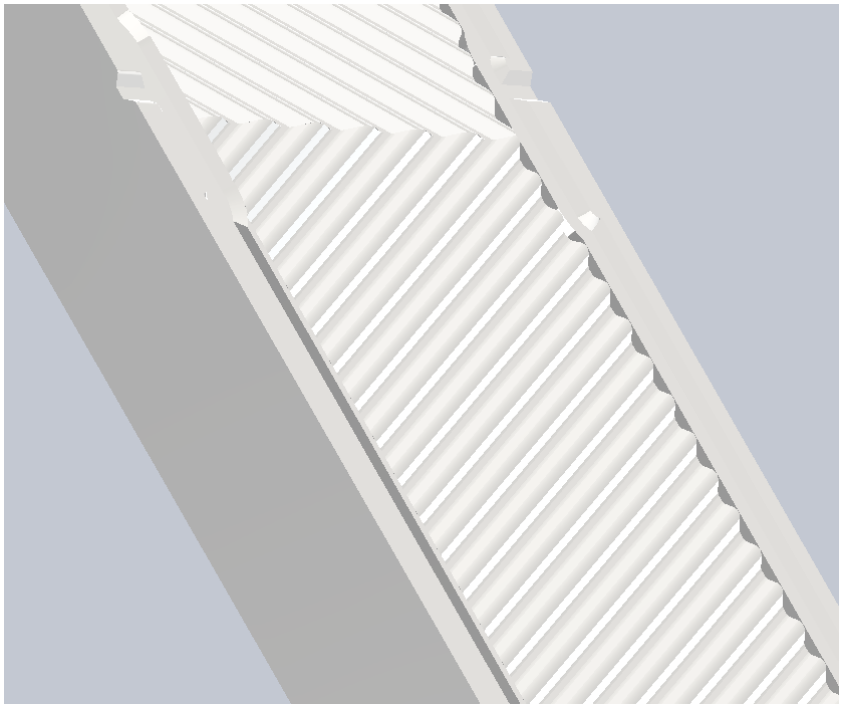

Figure 3.20: Part of the corrugation zone of the transparent endplate model

From table 2.1 it follows that most visualization studies done previously used a plate thickness of 30 [mm], while using materials with similar characteristics. Additionally, from the calculations done in the previous section, the thickness of 30 [mm] is proven to be sufficient to make bending effects negligible. Therefore, a plate thickness of 30 [mm] is used in the model.

CORRUGATION

It's essential that the corrugation zone is modelled as accurately as possible. Figure 3.20 shows the modelled corrugation. The corrugation is not simply a sinusoid, around the averaged line of the wave the profile is more linear (see figure 3.22a). The corrugation is mirrored over the central horizontal axis.

DISTRIBUTION ZONE

The flow enters the corrugation zone via the distribution zone, shown in on the right side of figures 3.21a and 3.21b. It is not quite clear how much this zone influences the flow, but it was modelled with an accuracy of ± 0.5 [mm] nevertheless, as is shown in the comparison of figure 3.21.

SIMPLIFICATIONS

Because the expected fabrication cost and time of the base model were too high at the central workshop of the Delft University of Technology, some simplifications needed to be made. The corrugation was slightly adjusted so it would be more simple to machine. At the minima of the corrugation wave, the wave was flattened (see figure 3.22). The flat parts are 1 [mm] wide. It was expected that it is unlikely that this change will influence the flow along the plate significantly.

Furthermore, some very complex details were removed. For example, the gasket fitting holes, shown in figure 3.23, were too complex to machine and had to be taken out. The gasket would instead be fixed to the transparent plate making use of tape.

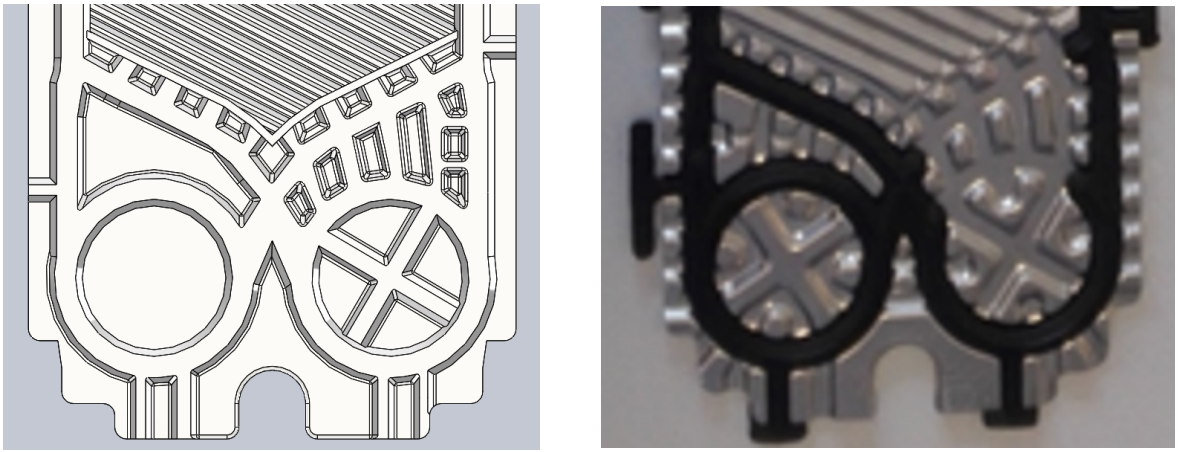

(a) Distribution zone of the transparent endplate model.

(b) Distribution zone of the original endplate

Figure 3.21: The distribution zone in the model compared to the distribution zone in the physical plate.

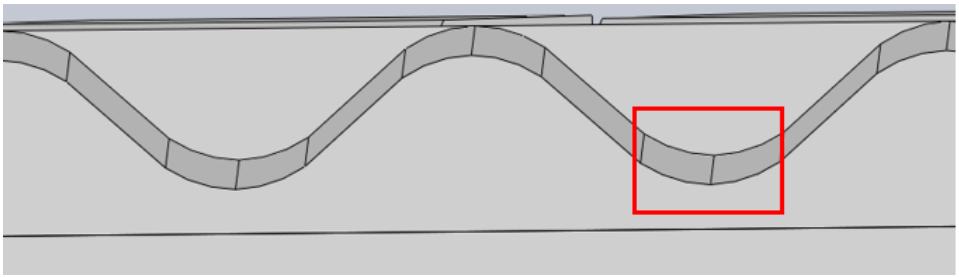

(a) The corrugation pattern in the base model

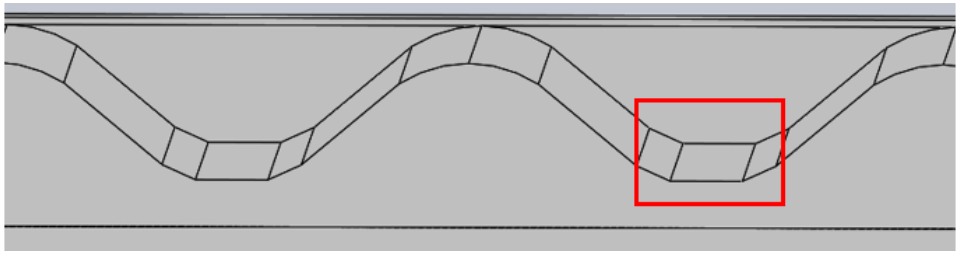

(b) The corrugation pattern in the simplified model

Figure 3.22: Difference in corrugation pattern between the base model and the simplified model.

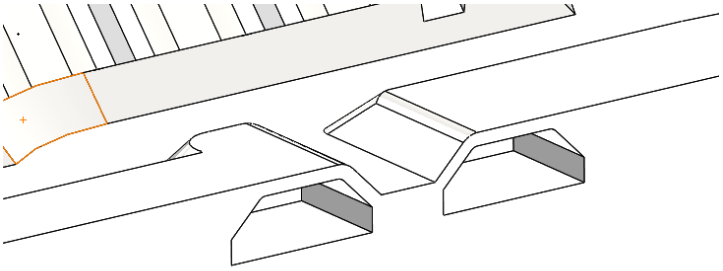

Figure 3.23: Gasket fitting holes in the transparent plate model.

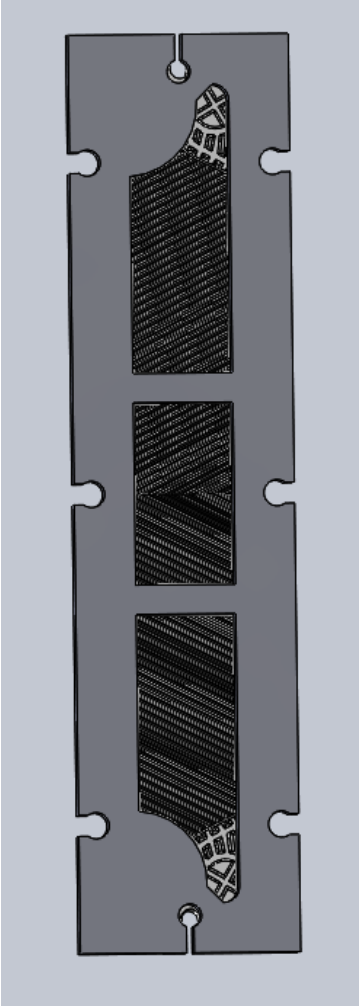

Figure 3.24: Front view of the pressure plate with window in front of the transparent endplate.

3.8. PRESSURE PLATE WITH WINDOW MODEL

Figure 3.24 shows the 3D CAD model of the new pressure plate with window, which makes visualization possible. The window is shaped in the form of the gasket, which the pressure plate needs to overlap. The two horizontal bars around the middle provide support.

3.9. VISUALIZATION SECTION

Figure 3.25a shows the fabricated PMMA transparent corrugated plate. The gasket fits in the gasket fitting gap. The corrugation pattern, gasket fitting gap and distribution zone details were created by machining, at the DEMO workshop at the Delft University of Technology.

Figure 3.25b shows the fabricated stainless steel pressure plate with window. The window was created by waterjet cutting at the same workshop as the transparent plate.

(a) The fabricated transparent corrugated plate, with gasket.

(b) The fabricated pressure plate with window

Figure 3.25: The fabricated plates.

4

NUMERICAL CONDENSER MODEL

The experimental set-up is extended in a way which allows more specific experiments to be done with the condenser, such as local temperature measurements and visualization experiments. The results of these experiments should be used for validation purposes by comparing them to the theory. Therefore, a model which can predict the experimental results was developed.

The model has the model by Goudriaan [2] and Kuikhoven [3] (the GoudKuik model) as starting point. They developed a model for the entire OTEC-cycle, before the extension to the OTEC-demo was made. In their model, the condenser was modelled separately. In this chapter, firstly the GoudKuik condenser model will be introduced shortly. Subsequently, the required adjustments and additions to this model will be discussed.

4.1. GOUDKUIK MODEL

The GoudKuik model is developed to predict the conditions of the flows in the condenser at the outlet using measured data at the inlet. The model was validated with experiments from OTEC-demo set-up before the implementation of the new condenser. Thus, the condenser part of this model is based on the brazed heat exchanger.

4.1.1. MODEL ALGORITHM

Figure 4.1 shows the condenser model algorithm used by Goudriaan [2] and Kuikhoven [3]. The inputs are the measured pressures and temperatures of the inlet flows on both the working fluid and the cold water side. The total heat transfer Q_{total} is assumed to be equal on both the cold water and the working fluid side (no heat losses), so $Q_{total} = Q_{water} = Q_{wf}$. It is calculated by making a guess for the cold water temperature $T_{water,out}$ at the outlet and using the following equation:

$$Q_{water} = \dot{m}_{water} \cdot c_{p,water} \cdot \Delta T_{water}. \tag{4.1}$$

Here c_p is the specific heat capacity in [J/kg K] and ΔT is the temperature difference. The specific heat capacity can be assumed to be relatively constant for the cold water, as the pressure and temperature difference over the condenser are relatively low and the cold water is in a single phase through the condenser (liquid).

The calculated total heat transfer is then divided over control volumes of equal heat transfer:

$$Q_{cv} = Q_{total} / n_{cv} \tag{4.2}$$

where n_{cv} is the set number of control volumes over the heat exchanger.

By assuming no heat is lost in the condenser, the calculated heat transfer per control volume is equal on the working fluid and the cold water side. On the working fluid side, the heat transfer per control volume can not be calculated with the specific heat capacity c_p, as the vapour quality is not constant over the condenser

and the vapour quality has a big influence on the specific heat capacity. Instead, on the working fluid side the heat transfer per control volume is related to the enthalpy change:

$$Q_{cv} = \dot{m}_{wf} \cdot \Delta h_{wf,cv} \tag{4.3}$$

The working fluid vapour flow (pure ammonia) and working fluid liquid flow (ammonia-water mixture) are mixed at the inlet of the condenser (see section 3.1.1 for details). This mixing process is assumed to be homogeneous and instant. From the energy balance, the working fluid inlet enthalpy can be determined:

$$h_{mix,wf,in} = \frac{\dot{m}_G \cdot h_G + \dot{m}_L \cdot h_L}{\dot{m}_G + \dot{m}_L}. \tag{4.4}$$

Subsequently, the enthalpy at the outlet of the first control volume of the working fluid side is calculated using equation 4.3. As the outlet conditions of a certain control volume are equal to the inlet conditions of the next control volume, this process can be repeated for all control volumes to obtain the entire enthalpy profile on the working fluid side of the condenser.

In the GoudKuik model the pressure drop over the condenser is assumed to be fixed and linear over the condenser. This way, the pressure at the inlet and outlet of every control volume can be determined. Subsequently, the temperature T and vapour quality x at the inlet and outlet of every control volume can be determined from the corresponding pressure P and enthalpy h from a thermodynamic library, using the pressure, the enthalpy and the ammonia concentration of the mixture: $T_{wf,in} = T_{wf,in}(h_{mix,wf,in}, p_{wf,in}, X_{wf,in})$ and $x_{wf,in} = T_{wf,in}(h_{mix,wf,in}, p_{wf,in}, X_{wf,in})$. In the GoudKuik model, the ammonia concentration is an input value which can manually be determined iteratively from the density ρ, the temperature T and the pressure P.

Using equation 4.5, the heat transfer per control volume is correlated to the heat transfer area per control volume.

$$Q_{cv} = U_{cv} \cdot A_{cv} \cdot \Delta T_{LM,cv} = U_{cv} \cdot A_{cv} \cdot \left(\frac{(T_{wf,in} - T_{water,out}) - (T_{wf,out} - T_{water,in})}{ln\frac{(T_{wf,in} - T_{water,out})}{(T_{wf,out} - T_{water,in})}} \right)_{cv} \tag{4.5}$$

The overall heat transfer coefficient U is defined by

$$U = \frac{1}{\frac{1}{\alpha_{wf}} + \frac{d_p}{\kappa_{wall}} + \frac{1}{\alpha_{water}}}, \tag{4.6}$$

in which α_{wf} is the two-phase convective heat transfer coefficient on the working fluid side and α_{water} is the single phase convective heat transfer coefficient on the cold water side. The overall heat transfer coefficient per control volume is given by

$$U_{cv} = \frac{1}{\frac{1}{\alpha_{cv,wf}} + \frac{d_p}{\kappa_{wall}} + \frac{1}{\alpha_{cv,water}}}, \tag{4.7}$$

where $\alpha_{cv,water}$ and $\alpha_{cv,wf}$ are the convective heat transfer coefficients per control volume. The convective heat transfer coefficients will be discussed further in section 4.1.2

The conductive heat transfer coefficient resistance term $\frac{d_p}{\kappa_{wall}}$ is small compared to the convective heat transfer coefficient terms, because the thickness d_p is very small (see table 3.2).

For every control volume, the heat transfer area of the control volume is determined using 4.5. The sum of these heat transfer areas is then compared to the specified heat transfer area from the brazed heat exchanger documentation. If the heat transfer area error is too large, the guessed outlet temperature on the water side is updated and the process is repeated. When the error is acceptable, the outlet conditions of the flows are determined. These values can then be compared with the experimental data.

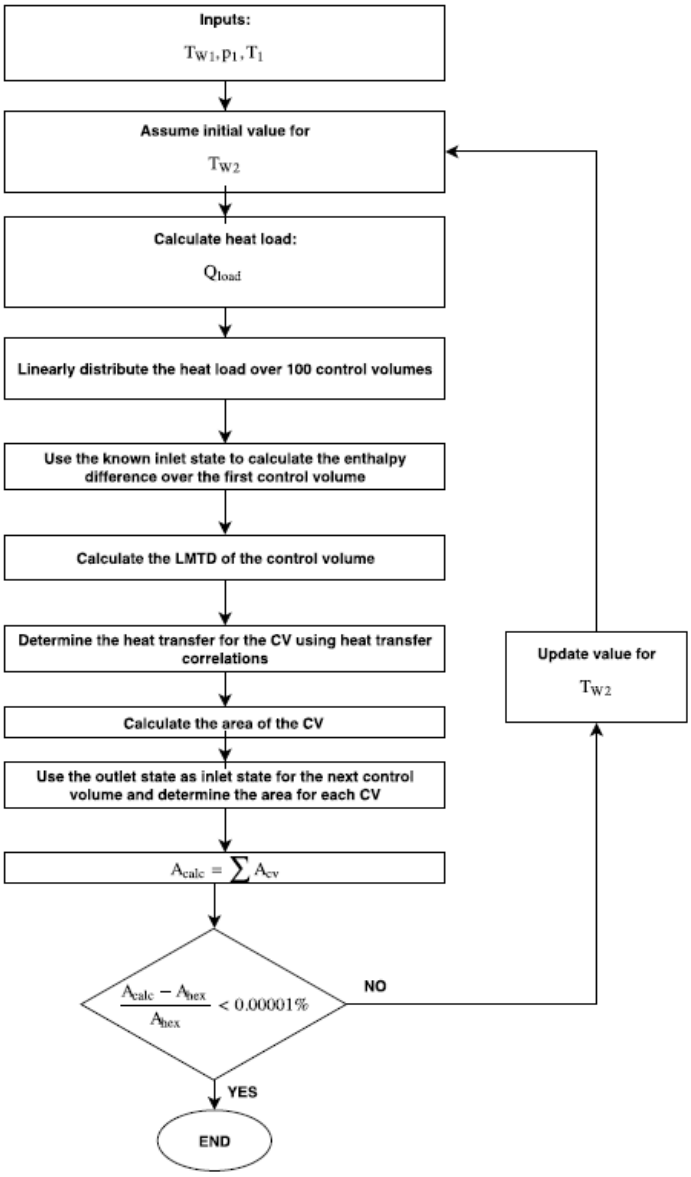

Figure 4.1: Condenser algorithm in the Goudkuik model. From Goudriaan [2].
$T_{w1} = T_{water,in}, T_{w2} = T_{water,out}, T_1 = T_{wf,in}, p_1 = P_{wf,in}, Q_{load} = Q_{cond}$
.

4.1.2. CONVECTIVE HEAT TRANSFER COEFFICIENTS

The Nusselt number Nu is a dimensionless property which is defined as the ratio between the convective and the conductive heat transfer. It can be given by the following equation

$$Nu = \frac{\alpha \cdot L}{\kappa} \tag{4.8}$$

where L is the characteristic length scale of the flow.

Regarding the Nusselt number multiple correlations have been proposed in literature, each valid for certain conditions. To the water side single phase correlations are applicable while to the working fluid side two-phase condensing correlations are applicable.

SINGLE PHASE

For single phase, the Nusselt number is generally determined from the following equation

$$Nu = a \cdot Re^{b} \cdot Pr^{1/3} \tag{4.9}$$

where the Prandtl number Pr is a dimensionless number which is defined as the ratio between the viscous diffusion rate and the thermal diffusion rate of a fluid. It can be given by

$$Pr = \frac{c_p \cdot \mu}{\kappa}. \tag{4.10}$$

Throughout literature the exponent of the Prandtl number is widely accepted to be 1/3. Regarding the constants a and b in equation 4.9 different values have been proposed. Goudriaan [2] and Kuikhoven [3] made a comparison of relevant single phase Nusselt number/convective heat transfer coefficient correlations for the condenser in OTEC-demo set-up.

As most correlations are only valid for specific conditions (such as a certain heat exchanger geometry or a certain range of Reynolds numbers), the most accurate way to describe the convective heat transfer coefficients is to fit a correlation for the conditions of the experimental set-up of the study. Goudriaan [2] and Kuikhoven [3] proposed the following single phase convective heat transfer correlation for the brazed heat exchanger:

$$\alpha_{SP} = \frac{\kappa}{d_{eq}} 0.29 Re^{0.72} Pr^{0.33}. \tag{4.11}$$

TWO-PHASE CONDENSING

On the working fluid side the Reynolds number is widely replaced by the equivalent Reynolds number for two-phase flow, which in this case is defined as

$$Re_{eq} = G\big((1-x) + x(\rho_L/\rho_G)^{1/2}\big) d_h/\mu_L. \tag{4.12}$$

Goudriaan [2] and Kuikhoven [3] made a comparison of relevant two-phase condensing Nusselt number/convective heat transfer coefficient correlations for the condenser in OTEC-demo set-up. Goudriaan [2] and Kuikhoven [3] proposed to use a correlation by Winkelmann [7] with a correction factor.

Geschiere [25] (2018) proposed the following two-phase condensing convective heat transfer coefficient correlation for the flow in the brazed heat exchanger:

$$Nu = 1.16 \cdot Re_{eq}^{0.48} \cdot Pr_L^{-0.50} \cdot Sc_L^{0.17} \tag{4.13}$$

Here the Schmidt number Sc is a dimensionless property defined as the ratio between the viscous diffusion and the molecular mass diffusion rate. It is defined as

$$Sc = \frac{\mu}{\rho \cdot D} \tag{4.14}$$

where D is the mass diffusivity in [m^2/s]. The liquid Schmidt number Sc_L can be calculated by using the liquid properties of the flow.

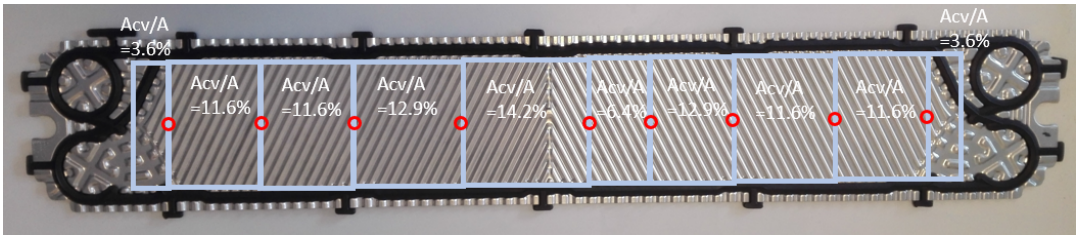

Figure 4.2: The percentages of the heat transfer area with respect to the total heat transfer area per plate between the individual local temperature sensors along the endplate of the gasketed heat exchanger. The red circles indicate the exact positions of the temperature measurements.

4.2. MODIFIED MODEL

The Goudkuik model had to be modified in such a way, that it could predict the local temperature experiments with the gasketed heat exchanger. First of all, the gasketed heat exchanger geometry was implemented, see table 3.2 for the difference in geometry between the brazed and the gasketed heat exchanger.

4.2.1. MODEL ALGORITHM

A large modification that was required, was to divide the heat transfer area A into control volumes instead of the heat transfer Q. This makes it possible to compare the calculated temperature profiles over the condenser by the model to the experimentally determined temperature profiles. The locations of the temperature sensors along the endplate of the gasketed heat exchanger correspond to a certain part of the total heat transfer area. The percentages of the total heat transfer area between the individual local temperature sensors are shown in figure 4.2.

Figure 4.3 shows the algorithm of the modified condenser model. From measurements, the working fluid inlet conditions and cold water outlet conditions can be determined (these are at the same position as the heat exchanger is of the countercurrent type). The specified heat transfer area is divided into control volumes, with the working fluid inlet and cold water outlet per control volume at node n and the working fluid outlet and cold water inlet per control volume at node n+1. The pressure drop over the heat exchanger on the water side per control volume is determined by using the proposed pressure drop correlation from the experiments (see section 5.1.2). On the working fluid side, no correlation was proposed, but the experimental data is still used to determine the pressure drop in the model (see section 5.2.2).

For every control volume, the working fluid and water temperature at point n+1 are determined iteratively, using the equations shown in figure 4.3. This requires convective single phase and two-phase heat transfer correlations applicable to the gasketed heat exchanger, which will be discussed in section 4.2.4. When the complete temperature profiles are determined, the calculation is finished. The total heat transfer, working fluid outlet temperature and cold water inlet temperature of the heat exchanger can now be compared to the experimental results.

4.2.2. ASSUMPTIONS

The following assumptions are made in the model:

- No heat loss, so $Q_{water} = Q_{wf}$
- No mass loss, so $\dot{m}_{in} = \dot{m}_{out}$
- Linear pressure drop over the condenser on both sides, so $\Delta P_{cv} = \Delta P / n_{cv}$
- Homogeneous mixing of vapour and liquid at condenser inlet on the working fluid side

4.2.3. PRESSURE DROP

Goudriaan [2] and Kuikhoven [3] assumed a fixed pressure drop over the condenser on the working fluid and water side. As discussed in section 3.2.3, the pressure drop for the gasketed heat exchanger is expected to be higher. In order to predict the pressure drop on both the water and working fluid side correctly, pressure drop

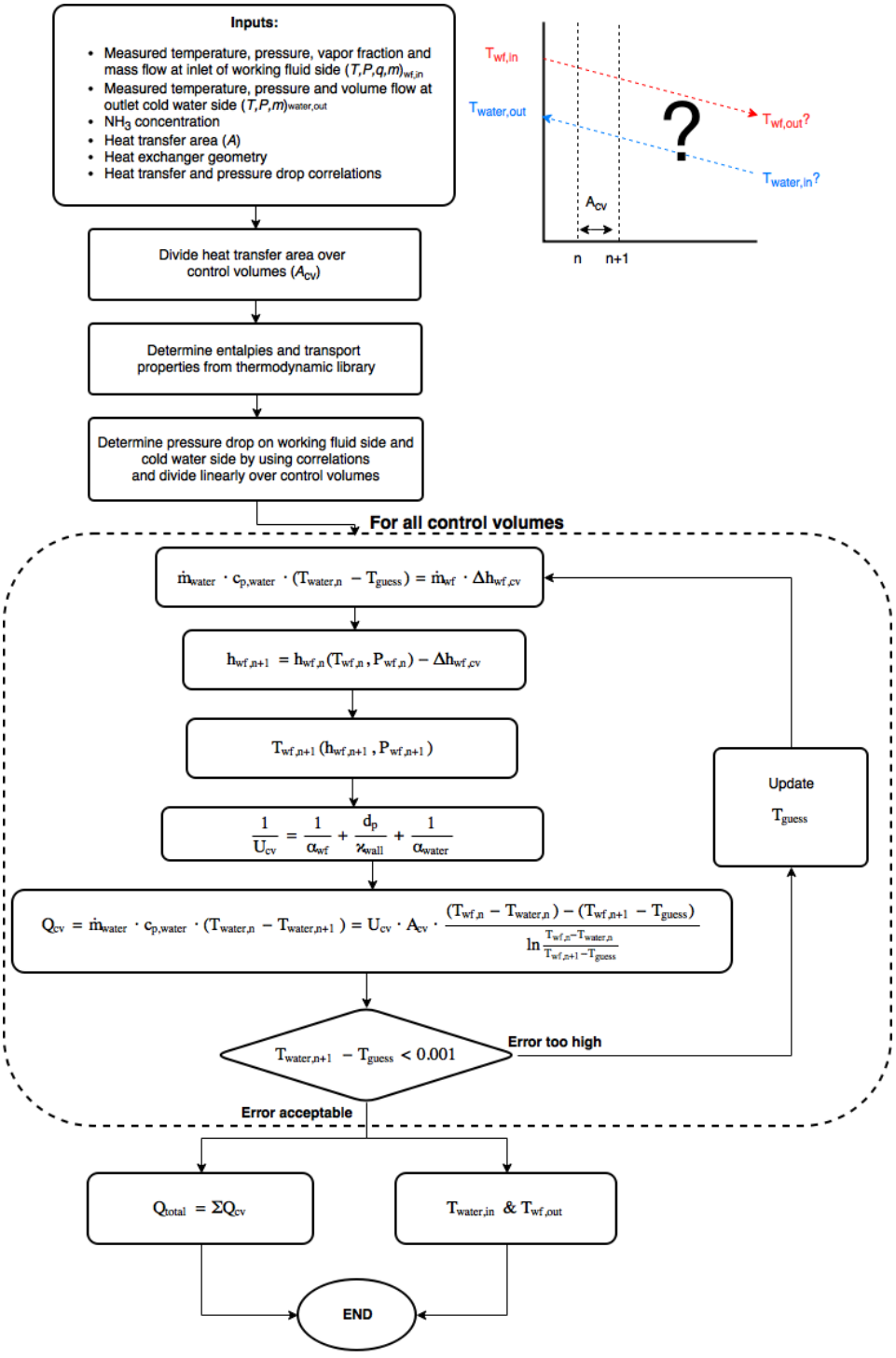

Figure 4.3: Algorithm of the numerical condenser model.

correlations are implemented in the model.

Firstly, an overview of currently available pressure drop correlations is given. Tao *et al.* [13] (2018a) performed a literature study on two-phase vertical downward flow in plate heat exchangers. According to this study, all factors that enhance heat transfer also increase pressure drop. Pressure drop increases for increasing condensation pressure, according to Grabenstein *et al.* [34] (2017), but the influence is small according to Longo [43] (2010), Yan *et al.* [15] (1999) and Kuo *et al.* [27] (2005). Larger chevron angles lead to higher pressure drop, according to Han *et al.* [26] (2003). Pressure drop increases slightly with mean heat flux, according to Yan *et al.* [15] (1999) and Kuo *et al.* [27] (2005).

Yan et al. (1999) [15] measured that between 93% and 99% of the total pressure drop was due to frictional pressure drop, which means other factors that influence pressure drop can be neglected. The frictional pressure drop is given by the following equation

$$\Delta P_f = 2 \cdot f \cdot \frac{G^2 \cdot L_p}{\rho \cdot d_h}, \tag{4.15}$$

where f is the Fanning friction factor. Another definition for the friction factor is $\zeta = 4f$.

SINGLE PHASE

Table 4.1 shows an overview of friction factor correlations for single phase in plate heat exchangers, which are relevant for this research. Some studies present different correlations for different chevron angles. In that case, the correlation for a chevron angle closest to the chevron angle of the heat transfer plates of the gasketed heat exchanger used for this study ($\beta = 63°$) is presented. A comparison of the proposed Fanning friction factor correlations for single phase flow will be shown in section 5.1.2, including the measured data.

Table 4.1: Overview of friction factor correlations for single phase flow in plate heat exchangers

Investigator	**Correlation**	**Validation range**
Martin (1996) [20]	$\frac{1}{\sqrt{\zeta}} = \frac{\cos\beta}{\sqrt{0.18\tan\beta + 0.36\sin\beta + \zeta_0/\cos\beta}} + \frac{1-\cos\beta}{\sqrt{3.8\zeta_1}}$ $\zeta_0 = \frac{64}{Re}$ $\zeta_1 = \frac{597}{Re} + 3.85$	$Re < 2000$
Winkelmann (2010) [7]	$f = 0.30 + 53Re^{-10}$ $f = 1.0Re^{-0.135}$	$10 < Re < 1700$ $1700 \leq Re < 50000$
Kumar (1984) [21]	$f = 19.40Re^{-0.589}$ $f = 2.990Re^{-0.183}$	$10 < Re < 100$ $Re > 100$, $\beta_{flow} \leq 30°$
Focke et al. (1985) [19]	$\zeta = 5.03 + 7.55/Re$ $\zeta = 26.8Re^{-0.209}$	$90 < Re < 400$ $400 \leq Re < 16000$ $\beta = 60°$
Thonon (1995) [18]	$f = 45.57Re^{-0.670}$ $f = 0.370Re^{-0.172}$	$Re < 160$ $Re > 160$ $\beta = 60°$
Heavner et al. (1993) [22]	$f = 0.490\Phi^{1.1814}Re^{-0.1814}$	$400 \leq Re \leq 10000$ $23° \leq \beta \leq 90°$
Khan et al.(2017) [24]	$f = 34.43Re^{-0.5}$	$500 < Re < 2500$ $\beta = 60°$
Luan et al. (2008) [23]	$f = 0.2Re^{-0.23}$	$1500 \leq Re \leq 15000$

TWO-PHASE CONDENSING

As the density of a fluid can change significantly during condensation, an averaged density should be used in a two-phase frictional pressure drop correlation, which becomes

$$\Delta P_f = 2 \cdot f_{TP} \cdot \frac{G^2 \cdot L_p}{\rho_{av} \cdot d_h}, \tag{4.16}$$

Table 4.2: Overview of Fanning friction factor correlations for condensation in plate heat exchangers

Investigator	Correlation	Validation range and fluid
Yan et al. (1999) [15]	$f = 94.75 Re_{eq}^{-0.0467} Re_{LO}^{-0.4} Bo^{0.5} \left(\frac{P}{P_{cr}}\right)^{0.8}$	R134a $500 < Re < 1000$ $60 \leq G \leq 120$ $10 \leq q \leq 16$ $0.1 \leq x_{av} \leq 0.9$
Han et al. (2003) [26]	$f = Ge_3 Re_{eq}^{Ge_4}$ $Ge_3 = 3521.1 \left(\frac{\Lambda_{wave}}{d_{eq}}\right)^{4.17} (\beta \cdot \frac{\pi}{180})^{-7.75}$ $Ge_4 = -1.024 \left(\frac{\Lambda_{wave}}{d_{eq}}\right)^{0.0925} (\beta \cdot \frac{\pi}{180})^{-1.3}$	R410A $20° < \beta_{flow} < 45°$ $10 \leq G \leq 35$ $4.7 \leq q \leq 5.3$
Kuo et al. (2005) [27]	$f = 21{,}500 Re_{eq}^{-1.14} Bo^{-0.085}$	R410A $10 \leq G \leq 35$ $4.7 \leq q \leq 5.3$ $0.1 \leq x_{av} \leq 0.9$

where ρ_{av} is the averaged density, defined as

$$\frac{1}{\rho_{av}} = \frac{1-x}{\rho_L} + \frac{x}{\rho_G} \tag{4.17}$$

Little research has been done on condensation pressure drop. One of the few studies in which a pressure drop correlation was proposed is Yan *et al.* [15], who proposed the following correlation,

$$f = 94.75 Re_{eq}^{-0.0467} Re_{LO}^{-0.4} Bo^{0.5} \left(\frac{P}{P_{cr}}\right)^{0.8}, \tag{4.18}$$

in which the liquid only Reynolds number Re_{LO} is defined as

$$Re_{LO} = \frac{G \cdot d_h}{\mu_L}, \tag{4.19}$$

and Bo is the Boiling number, defined as

$$Bo = \frac{q}{G \cdot h_{fg}}, \tag{4.20}$$

where h_{fg} is the latent heat of condensation. The critical pressure P_{cr} of ammonia is equal to 113.336 [bara]. An overview of the Fanning friction factor correlations for condensation is given in table 4.2. A comparison of the proposed correlations including the measured data will be made in section 5.2.2.

As ammonia(-water) is used as the working fluid for this research instead of R410A or R134a, some properties that influence the Reynolds equivalent number Re_{eq} or Boiling number Bo differ (see table 4.3). The density ratio of liquid to gas is a lot higher for the ammonia. The latent heat, which is a parameter in the Boiling number equation, also differs quite a lot for ammonia. The dynamic viscosities differ relatively little.

Table 4.3: Fluid property comparison of ammonia and the refrigerants R410A and R134a for the operating pressures of the two-phase studies.

	h_{fg}	ρ_G	ρ_L	ρ_G/ρ_L	μ_L
	[kJ/kg]	[kg/m^3]	[kg/m^3]	-	10^{-6} [Pa s]
Ammonia (P = 6.6 [bar])	1217.71	5.21	621.71	119.38	149.83
R410A (P=14.4 [bar])	198.93	55.53	1084.0	19.52	126.18
R134a (P=6.75 [bar])	218.86	32.82	1204.9	36.71	193.72

Other parameters which influence the Reynolds equivalent number Re_{eq} or Boiling number Bo also differ between the considered studies. The flow passage area A_f influences the mass flux G while the heat flux q is a factor in the boiling number equation. All the differences in these parameters lead to modified friction factor correlations for the conditions in this study.

Table 4.4 presents a geometric comparison of parameters in the heat exchanger that influence Reynolds number and/or friction factor, between the present study and the other two-phase studies.

Table 4.4: Comparison of geometric parameters between the two-phase studies.

	d_h	A_f	β
	[m]	[m^2]	[°]
Present study	0.0030	0.00017	63
Yan et al. (1999) [15]	0.0047	0.00049	60
Han et al. (2003) [26]	0.0035	0.00025	70/55/45
Kuo et al. (2005) [27]	0.0047	0.00049	60

The single phase pressure drop correlation is determined from water-water experiments (see sections 5.1.2 and 5.2.2).

4.2.4. HEAT TRANSFER

Kuikhoven [3] made a comparison of convective heat transfer coefficient correlations for single phase flow and for condensing flow. Goudriaan [2] and Kuikhoven [3] proposed a single phase convective heat transfer correlation for the brazed heat exchanger in the OTEC-demo set-up and Geschiere [25] proposed a two-phase convective heat transfer correlation for the condensation of ammonia-water in the brazed heat exchanger. In section 5.1.1 a comparison of the single phase convective heat transfer coefficient correlations will be made for the measured data in this research and in section 5.2.1 the same will be done for the condensing flow.

In the modified model, the single phase convective heat transfer coefficient correlation (equation 5.1) proposed in section 5.1.1 for the gasketed heat exchanger will be used. Regarding the convective heat transfer coefficient for condensation, equation 5.14 is used.

5

RESULTS AND DISCUSSION

5.1. WATER/WATER EXPERIMENTS

In order to obtain single phase heat transfer and pressure drop correlations for the cold water side in the condenser, water/water experiments were executed, in which the system was filled with (demi)water. Thus, in the condenser, heat was transferred from the hot water side (working fluid side) to the cold water side.

Input parameters Originally, the plan was to vary the cold water flow and the effective number of heat transfer plates, while keeping the other input parameters constant. Two configurations would be used for the number of effective plates, the maximum (8 effective plates) and the minimum (1 effective plate). However, during the set of experiments with 8 effective plates, it became apparent that temperature difference between the working fluid outlet and the cold water inlet was very low. This induced the following problems: a high risk of error in the logarithmic temperature difference of the gasketed heat exchanger and a significant part of the heat transfer area in the gasketed heat exchanger used ineffectively. In short, the heat transfer area is too large when using the maximum number of plates.

Subsequently, only single channel experiments are performed (one channel for the hot water and one channel for the cold water), in which the cold water flow was varied. The temperature difference between the working fluid outlet and the cold water inlet is a lot higher for a single channel configuration in the condenser. For the single channel arrangement, the cold water flow rate was limited to 0.16 [L/s], because the pressure drop would become too high for higher cold water flows. The minimum cold water flow rate was found to be 0.045 [L/s]. The cold water flow was varied between the minimum and maximum value.

Relevant measurements were done on the following cold water volume flows: 0.045 [L/s], 0.050 [L/s], 0.070 [L/s], 0.100 [L/s], 0.120 [L/s], 0.150 [L/s] and 0.153 [L/s]. The cold water inlet temperature was constant at 10 [°C]. The warm water mass flow was constant at 0.012 [kg/s]. The warm water inlet temperature of the condenser was between 16.3 [°C] and 16.4 [°C]. Table 5.1 shows the set volume flows for the water-water experiments and its corresponding Reynolds numbers.

Heat transfer unbalance During the water-water experiments, it became apparent that there was a heat transfer unbalance in the condenser. The calculated heat transfer rate of the cold water side was higher than the heat transfer rate on the hot water side (working fluid), by 6%-20% (0.02 [kW] - 0.1 [kW] out of 0.3 [kW]-0.4 [kW]).

Table 5.1: The set volume flows for the water-water experiments and its corresponding Reynolds numbers. The warm water mass flow was constant at 0.012 [kg/s]. The warm water inlet temperature of the condenser was between 16.3 [°C] and 16.4 [°C].

Volume flow $\dot{V}$ [L/s]	0.045	0.050	0.070	0.100	0.120	0.150	0.153
Reynolds number Re	725	805	1127	1611	1932	2416	2472

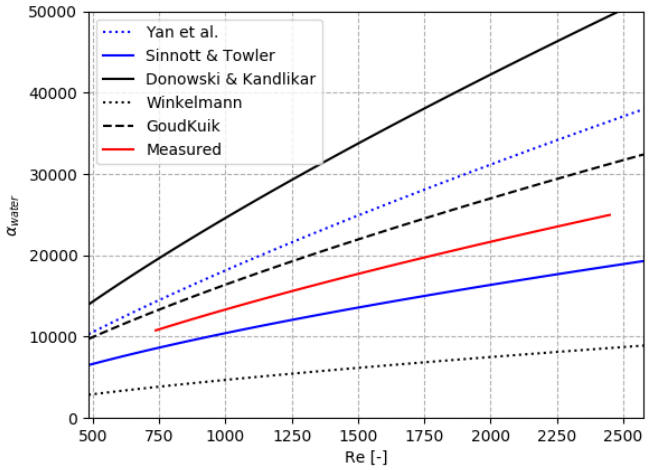

Figure 5.1: Convective heat transfer coefficient correlation comparison for single phase flow, including this research, Yan *et al.* [15], Sinnott and Towler [16], Donowski and Kandlikar [17], Winkelmann [7] and Goudriaan [2]/Kuikhoven [3].

After this phenomenon was observed, an additional layer of insulating material (the thickness of the insulating layer was doubled) was added around the condenser. The tubes at the in- and outlet of the condenser were insulated as well.

A new set of experiments was executed, in which the phenomenon was still present. Subsequently, the uncertainty analysis was done for the cold water flow sensor and the in- and outlet temperature sensors. The uncertainty of the temperature is ±0.05°C and the uncertainty of the temperature rise is ±0.1°C. This seems to explain the heat transfer unbalance in the condenser.

5.1.1. HEAT TRANSFER

Longo and Gasparella [44] describe a method to determine the single phase convective heat transfer coefficient, for which water/water experiments are required. As there is water flowing on both sides of the heat exchanger plates (both in single phase), the same convective heat transfer coefficient correlation can be used on both sides. This way the number of unknowns is reduced. Using the method by Longo and Gasparella [44], the following single phase convective heat transfer coefficient correlation is proposed for the condenser:

$$\alpha_{water} = \frac{\kappa_{water}}{d_h} \cdot 0.2709 \cdot Re_{water}^{0.7} \cdot Pr_{water}^{0.333} \tag{5.1}$$

Figure 5.1 shows the proposed single phase heat transfer correlation compared to the existing correlations. The trend seems to indicate the flow was turbulent during the experiments, which can be achieved in plate heat exchangers at lower Reynolds numbers, because of the structure of the plates. The convective heat transfer coefficient increases significantly for increasing Reynolds numbers of the flow. None of the correlations other than equation 5.1 can be used to determine the single phase convective heat transfer coefficient in the gasketed heat exchanger. Goudriaan [2] and Kuikhoven [3] proposed the GoudKuik correlation from experimental data on the same set-up, but they used the brazed heat exchanger as the condenser in the cycle.

5.1.2. PRESSURE DROP

The pressure drop of the cold water over the condenser is shown in figure 5.2. As discussed earlier in this section, a set of experiments without insulating material around the condenser was done. This set of experiments is not useful for any heat transfer related parameters, but it has shown to be useful for the pressure drop, as the pressure drop is less effected by heat loss. During the experiments without insulation, more data points were gained than during the experiments with insulation. Therefore, pressure drop data from these experiments are also shown in figure 5.2. The trendline is similar for both sets of experiments.

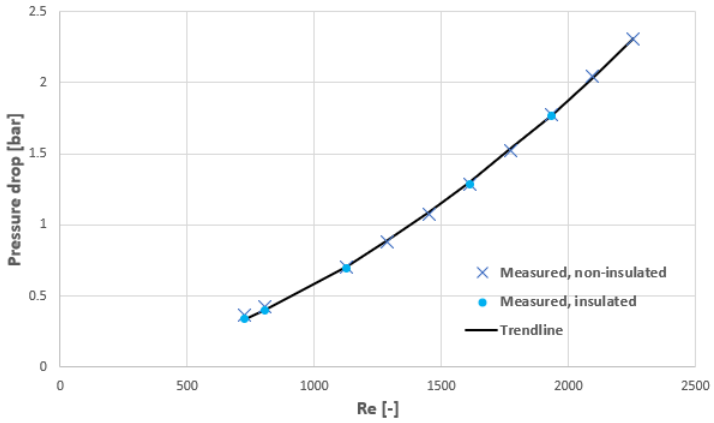

Figure 5.2: The measured cold water pressure drop over the condenser versus the Reynolds number, for Reynolds numbers in the range 725-2255. Pressure drop data from both a set of experiments with insulation around the condenser and a set of experiments without insulation are shown. The trend is similar for both experiments.

Figure 5.2 shows a trendline of the following equation

$$\Delta P_{water} = 0.46 \cdot Re_{water}^{1.7}, \tag{5.2}$$

with ΔP in [Pa].

Now, the factors that influence the measured pressure drop on the cold water side will be investigated.

Pressure drop in pipes The pressure drop in the PVC pipes from the pressure drop sensors to the condenser can be given by (VDI [45])

$$\Delta P_{pipes} = \xi \cdot \frac{L_{pipes}}{d_{pipes}} \cdot \frac{\rho_{water} \cdot w_{water}^2}{2} \tag{5.3}$$

where L_{pipes} is the total length of the pipes from the pressure drop sensors to the condenser, d_{pipes} is the diameter of the pipes, w_{water} is the water velocity in the pipes and ξ is the drag coefficient. The total length of the pipes from the pressure drop sensors to the condenser is approximately 2.5 [m] and the inner diameter of the PVC pipes on the cold water side is 27 [mm].

The water velocity w_{water} can be calculated by dividing the volume flow over the cross section area of the pipes: $w_{water} = 0.153 \cdot 10^{-3} / (\frac{1}{4}\pi d^2) = 0.267$ [m/s] (for the maximum measured volume flow).

The Reynolds number of the flow through the pipes then becomes $Re = 6347$. As the Reynolds number is in the range of 3000 < Re < 100,000, the drag coefficient ξ can be calculated with a formula by Blasius,

$$\xi = \frac{0.3164}{\sqrt[4]{Re}}. \tag{5.4}$$

In this case, the drag coefficient ξ is equal to 0.035. This leads to a pressure drop in the pipes of ΔP_{pipes} = 117 [Pa], which is negligible.

The elbows in the PVC piping between the in- and outlet pressure sensors on the cold water side involve a pressure drop as well, which can be calculated with the following equation in White [46]:

$$\Delta P_{elbows} = \Sigma K \cdot \frac{\rho_{water} \cdot w_{water}^2}{2}. \tag{5.5}$$

Here K is the resistance coefficient of an elbow part and ΣK is the sum of these resistance coefficients. Between the in- and outlet pressure sensors on the cold water side, there are three 90° elbows with a long radius (K = 0.72 each), there is one 90° elbow with a regular radius (K = 1.5) and there is one 45° elbow with a regular radius (K = 0.32). The sum of the resistance coefficients of the elbows in the PVC piping is then ΣK = 3.98.

The pressure drop resulting from the elbows then becomes $\Delta P_{elbows} = 142$ [Pa] for the maximum measured flow velocity, which is also negligible.

Elevation pressure change The pressure drop which follows from the vertical distance between the pressure inlet and pressure outlet sensors on the cold water side, is given by

$$\Delta P_{ele,water} = \rho_{water} \cdot g \cdot H. \tag{5.6}$$

Here H is the vertical distance between the inlet pressure sensor and the outlet pressure sensor on the cold water side. Using the measured height difference of 0.39 [m], this leads to a pressure drop due to elevation of $\Delta P_{ele,water} = 0.038$ [bar], which is a significant value and will be taken into account.

Frictional pressure drop The frictional pressure drop in the condenser can now be calculated by subtracting the elevation pressure change from the total measured pressure drop on the cold water side:

$$\Delta P_{f,water} = \Delta P_{water} - \Delta P_{ele,water} \tag{5.7}$$

The trend line for frictional pressure drop only then becomes

$$\Delta P_{f,water} = 0.195 \cdot Re_{water}^{1.81}. \tag{5.8}$$

By combining equation 4.15 and equation 2.1 the Fanning friction factor correlation for single phase can now be determined:

$$f_{water} = \frac{\Delta P_{f,water} \cdot \rho_{water} \cdot d_h^3}{2 \cdot Re_{water}^2 \cdot \mu_{water}^2 \cdot L_p}. \tag{5.9}$$

As the geometric parameters (hydraulic diameter $d_h = 2.99$ [mm] and effective plate length $L_p = 0.586$ [m]) did not change during the experiments and the dynamic viscosity μ and density ρ can be assumed to be constant for the single phase experiments, the only parameter that influences the pressure drop is the Reynolds number Re. Subsequently, the single phase pressure drop correlation following from the water-water experiments leads to the following single phase friction factor correlation:

$$f_{water} = 2.285 \cdot Re_{water}^{-0.19}. \tag{5.10}$$

Figure 5.3 shows the single phase Fanning friction factor correlation comparison including the existing Fanning friction factor correlations (see table 4.1). Equation 5.10 is similar to the correlation proposed by Martin [20].

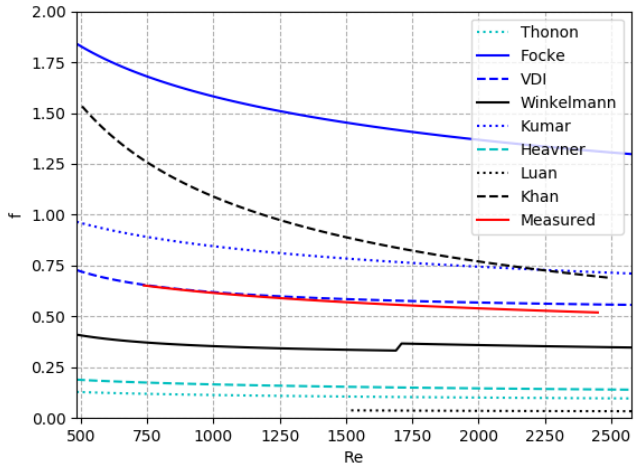

Figure 5.3: Fanning friction factor correlation comparison for single phase flow, including this research, Thonon [18], Focke *et al.* [19], Martin [20] (VDI), Winkelmann [7], Kumar [21], Heavner *et al.* [22], Luan *et al.* [23] and Khan *et al.* [24].

5.2. AMMONIA-WATER MIXTURE CONDENSATION EXPERIMENTS

In order to research the influence of the vapour quality x and the mass flux G on the convective heat transfer coefficient of an ammonia-water mixture working fluid, experiments were executed.

Input parameters: working fluid mass flow Similar to the water-water experiments, the ammonia-water mixture condensation experiments were done with a single channel arrangement, so only one effective heat transfer plate was used. During the ammonia-water experiments, firstly the working fluid flow was varied. Measurements were done on the following working fluid mass flows $\dot{m}_{wf}$: 0.0084 [kg/s], 0.0094 [kg/s], 0.0104 [kg/s], 0.0116 [kg/s], 0.0118 [kg/s], 0.0130 [kg/s], 0.0136 [kg/s], 0.01367 [kg/s] and 0.01368 [kg/s] (see table 5.2). No stable condition was achieved outside this range. The cold water inlet temperature was constant at 5 [°C] and the cold water flow was constant at 0.012 [L/s].

Resulting parameters From equation 2.2 the corresponding mass fluxes G_{wf} can be determined (The flow passage area $A_f = 1.634 \cdot 10^{-4}$ [m^2]). The corresponding Reynolds numbers can be determined by equations 2.12 (liquid Reynolds number Re_L), 4.19 (Liquid only Reynolds number Re_{LO}), 4.12 (equivalent Reynolds number Re_{eq}). An overview of the referred equations is made below:

$$G = \frac{\dot{m}}{A_f} \qquad \text{(2.2 revisited)}$$

$$Re_L = \frac{G \cdot (1-x) \cdot d_h}{\mu_L} \qquad \text{(2.12 revisited)}$$

$$Re_{LO} = \frac{G \cdot d_h}{\mu_L} \qquad \text{(4.19 revisited)}$$

$$Re_{eq} = G\big((1-x) + x(\rho_L/\rho_G)^{1/2}\big)\frac{d_h}{\mu_L} \qquad \text{(4.12 revisited)}$$

The working fluid mass flux did influence the ammonia concentration in the ammonia-water mixture (see figure 5.4) and vapour quality (see figure 5.5). The concentrations were determined iteratively from the density ρ, the temperature T and the pressure p by using the REFPROP library by the National Institute of Standards and Technology (Lemmon *et al.* [47]). The inlet vapour quality x_{in} can be determined from the working fluid inlet conditions by using a thermodynamic library. The outlet vapour quality x_{out} can be determined in a similar way from the working fluid outlet conditions. The average vapour quality is equal to the average of the inlet and outlet vapour quality. The liquid phase density ρ_L and the vapour phase density ρ_G

are determined from a thermodynamic library. The average of the densities at the inlet pressure and at the outlet pressure and the average vapour quality x_{av} are used to calculate the Reynolds numbers. The hydraulic diameter d_h is 2.994 [mm]. The liquid phase dynamic viscosity is assumed to be constant at $\mu_L = 154$ [μPa s].

Input parameters: inlet vapour quality Secondly, a few measurements were done in which the pressure over the valve that replaced the turbine was varied, which influences the inlet vapour quality. Measurements were done on the following inlet vapour qualities: 0.346, 0.314, 0.280 and 0.263 (see table 5.3). The working fluid flow was constant for these measurement points at 0.0125 [kg/s]. It should be noted that the inlet pressure varied between 5.3 and 4.8 [barg].

Table 5.2: The set mass flows for the ammonia-water mixture condensation experiments with the corresponding mass fluxes, Reynolds numbers, concentrations and vapour qualities.

Mass flow $\dot{m}_{wf}$ [kg/s]	0.0084	0.0094	0.0104	0.0116	0.0118	0.0130	0.0136	0.01367	0.01368
Mass flux G_{wf} [kg/m^{2}s]	51.64	57.69	63.73	71.25	72.36	79.36	83.24	83.63	83.69
NH_3 conc.	0.922	0.913	0.910	0.909	0.907	0.906	0.909	0.906	0.907
Vapour inlet quality x_{in}	0.483	0.427	0.383	0.337	0.335	0.299	0.280	0.282	0.284
Average vapour quality x_{av}	0.398	0.352	0.316	0.277	0.276	0.244	0.230	0.231	0.233
Vapour outlet quality x_{out}	0.314	0.277	0.248	0.217	0.216	0.190	0.179	0.180	0.182
Liquid Reynolds number Re_L	604	727	848	1002	1019	1166	1246	1249	1247
Liquid only Reynolds number Re_{LO}	1004	1122	1239	1385	1407	1543	1618	1626	1627
Equivalent Reynolds number Re_{eq}	6192	6282	6355	6399	6476	6472	6464	6531	6576

Table 5.3: The vapour quality inputs for ammonia-water mixture experiments in which the vapour quality x was varied while the mass flux G was constant.

Vapour inlet quality x_{in}	0.346	0.314	0.280	0.263
Average vapour quality x_{av}	0.285	0.259	0.229	0.216
Vapour outlet quality x_{out}	0.225	0.203	0.178	0.168

Subcooler Because only one effective heat transfer plate was used, the effective heat transfer area is quite small. As the heat transfer area is proportionally related to the total heat transfer, the total heat transfer is relatively low. This means the working fluid flow was not fully condensed after the condenser.

As mentioned in section 3.2.1, the brazed heat exchanger can be used as a subcooler. To make sure the flow is fully condensed when entering the buffer tank, the brazed heat exchanger was used as subcooler during the ammonia-water experiments. If the flow is not fully liquid when entering the buffer tank, no stable condition can be achieved, because the liquid level will keep decreasing.

5.2.1. HEAT TRANSFER AND TEMPERATURE PROFILES

As mentioned in section 3.6, nine local temperature sensors were placed along one of the endplates of the gasketed heat exchanger. This allows temperature profiles in the condenser to be measured and the local heat flux and heat transfer coefficient in the segments between two local temperature sensors to be determined. The heat flux per segment can be calculated by using

$$q_{segment} = \frac{Q_{segment}}{A_{segment}}. \tag{5.11}$$

The area of the each segment $A_{segment}$ is measured (see figure 4.2). The heat transfer per segment $Q_{segment}$ can be determined from

$$Q_{segment} = \dot{m} \cdot \Delta h_{segment}. \tag{5.12}$$

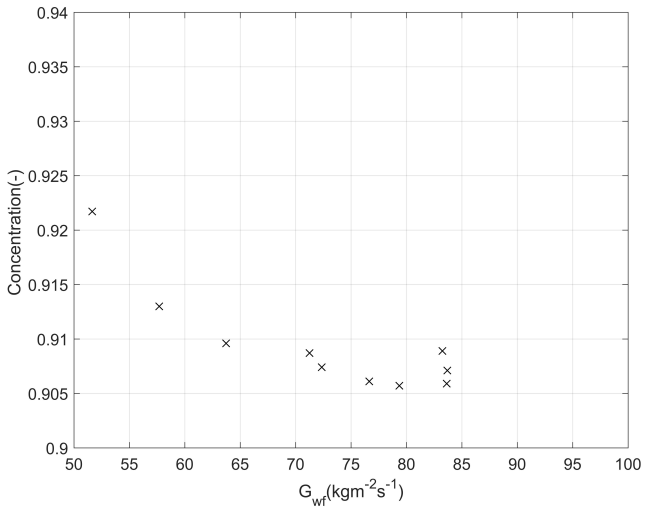

Figure 5.4: The working fluid concentration versus the working fluid mass flux G_{wf}, during the ammonia-water mixture experiments. The measured concentration range is 0.908 to 0.922 and the measured working fluid mass flux range is 52 to 84 [kg/m^{2}s].

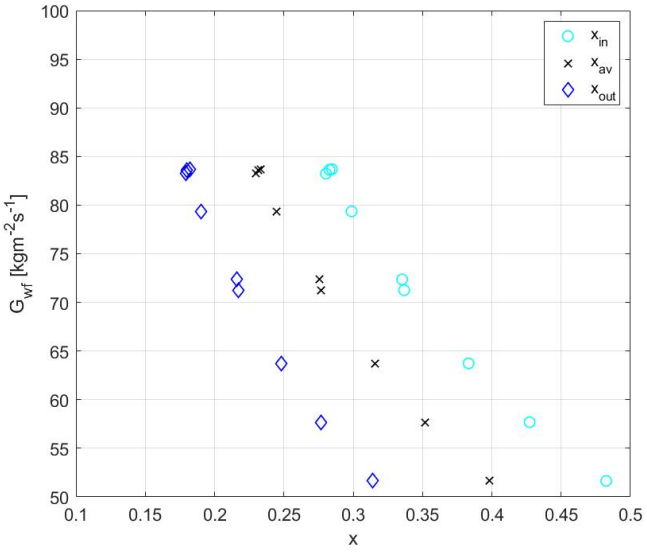

Figure 5.5: The working fluid mass flux G_{wf} versus the inlet vapour quality x_{in}, average vapour quality x_{av} and outlet vapour quality x_{out}, during the ammonia-water mixture experiments. The measured working fluid mass flux range is 52 to 84 [kg/m^{2}s].

The enthalpy difference per segment $\Delta h_{segment}$ can be determined from the measured local temperatures and by assuming a linear pressure drop profile. During the ammonia-water experiments, the local temperature sensors measured the local temperatures of the cold water flow. On the working fluid side, the saturation temperatures can be determined from the pressure, as the working fluid is in the two-phase region in the condenser. Then, the local overall heat transfer coefficient of the segment $U_{segment}$ can be obtained from the following equation

$$Q_{segment} = A_{segment} \cdot U_{segment} \cdot \Delta T_{LM,segment}. \tag{5.13}$$

Figure 5.6 shows the measured temperatures for the different working fluid mass flows at the corresponding positions on the plate. The red circles show the measured temperatures on the working fluid side. At the working fluid inlet, both the liquid and the vapour inlet are shown, where the vapour flow is the highest temperature of the two. The measured cold water temperature profile is shown by dark blue points. The cold water temperature profile is clearly linear for all the working fluid mass flows. This means that the convective heat transfer coefficient on the working fluid side does not change much over the length of the plate, which can be explained by the small change in vapour quality during the ammonia-water mixture condensation experiments.

Figure 5.7 shows the measured temperatures for the different working fluid inlet vapour qualities. The measured cold water temperature profiles are still linear in this case. At $x = 0.346$ [−], the measured temperatures (except the set cold water inlet temperature) are significantly higher compared to the other measurements. The working fluid inlet, working fluid outlet and cold water outlet temperatures all decrease for decreasing vapour flow.

Issues The second and fourth local temperature sensor, counting from the cold water outlet side, malfunctioned before the first measurement. The temperatures at these positions are determined by linear interpolation.

The measured temperature at the first local temperature sensor on the cold water outlet side was surprisingly equal to the temperature at the cold water outlet, even though there is a significant heat transfer area between these sensors. On the inlet side however, the measured difference between the last local temperature sensor and the cold water inlet temperature sensor was quite high (around 0.48 $^{\circ}C$), while the heat transfer area between these sensors is similar. These temperature differences are expected to be similar. The local temperature sensors are placed at the other side of the heat transfer plate with respect to the cold water flow (see figure 3.18), which leads to a small error in the measurements of the local temperature sensors, even though in actual steady state the temperatures should be equal as the system is assumed to be adiabatic. The combined thermal conductivity of the stainless steel endplate ($\kappa_{ss} = 16.3$ [W/(m · K)]) and the zinc thermal paste ($\kappa_{zinc} = 116$[W/(m · K)]) seemingly is too low to create temperature equality at both sides of the endplate. The local temperature sensors are therefore corrected by subtracting 0.24 °C.

Heat transfer coefficients As the convective heat transfer coefficient on the cold water side is known (see 5.1.1), the convective heat transfer coefficient on the working fluid side can be determined from equation 4.6.

Figure 5.8 shows the convective heat transfer coefficient on the working fluid side and the overall heat transfer coefficient versus the working fluid mass flux for the ammonia-water mixture condensation experiments. As expected from literature, the heat transfer coefficients increase for increasing mass flux. Figure 5.9 shows the convective heat transfer coefficient on the working fluid side and the overall heat transfer coefficient versus the vapour quality. As Tao *et al.* [13] conclude, the vapour quality and mass flux have a large influence on the convective heat transfer coefficient.

In the measured mass flux range of 52 to 84 [kg/m^{2}s], the following equation is used:

$$\alpha_{wf} = \frac{\kappa_{wf}}{d_h} \cdot 13.35 \cdot Re_{eq}^{0.35} \cdot Pr_L^{1/3} \tag{5.14}$$

The liquid Prandtl number is given by

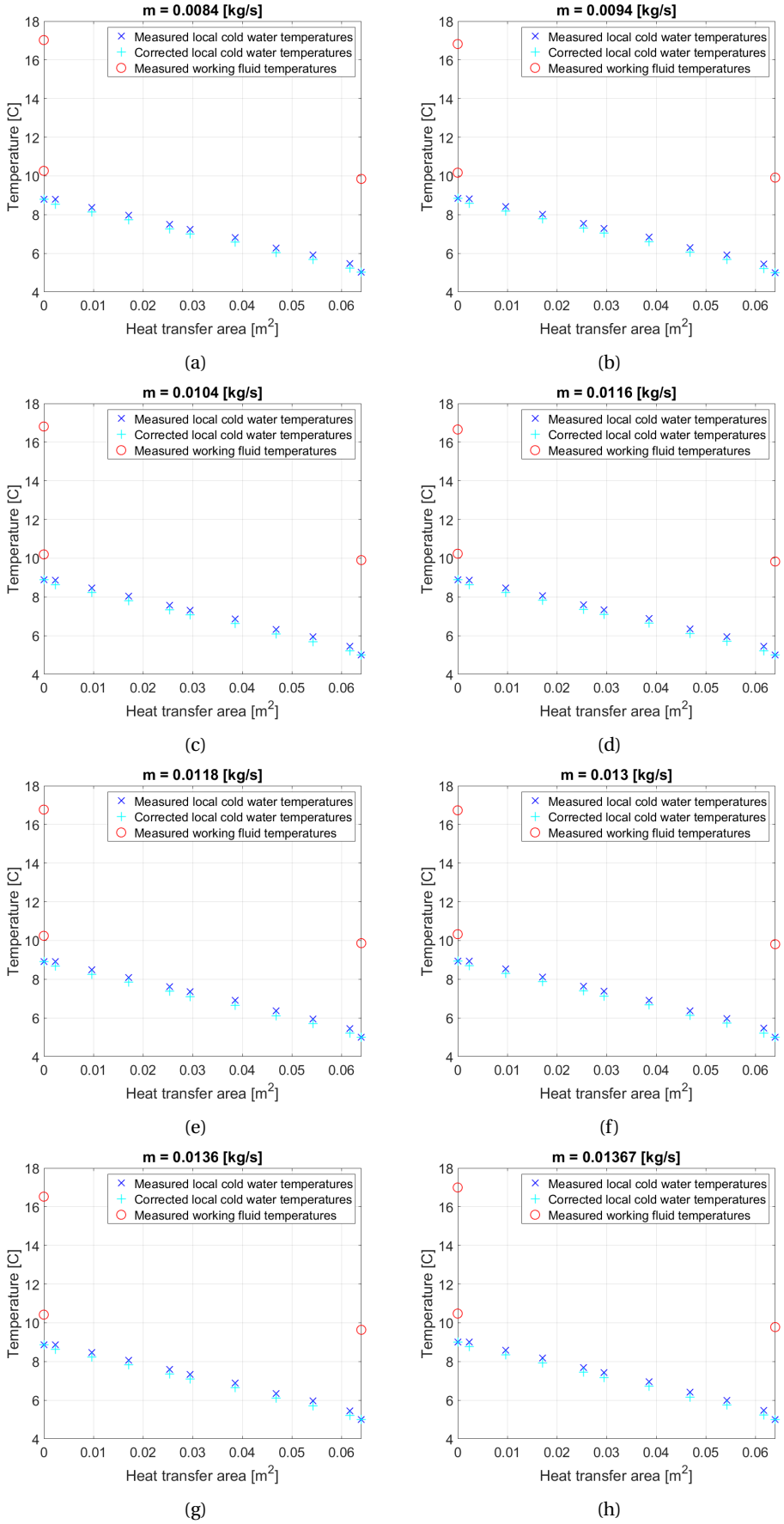

Figure 5.6: The measured temperatures T for various ammonia-water working fluid mass flows m_{wf}, versus the heat transfer area A. The subfigures a to h show the liquid working fluid inlet temperature, the vapour working fluid inlet temperature, the working fluid outlet temperature, the cold water inlet and outlet temperatures and the local cold water temperatures in the condenser.

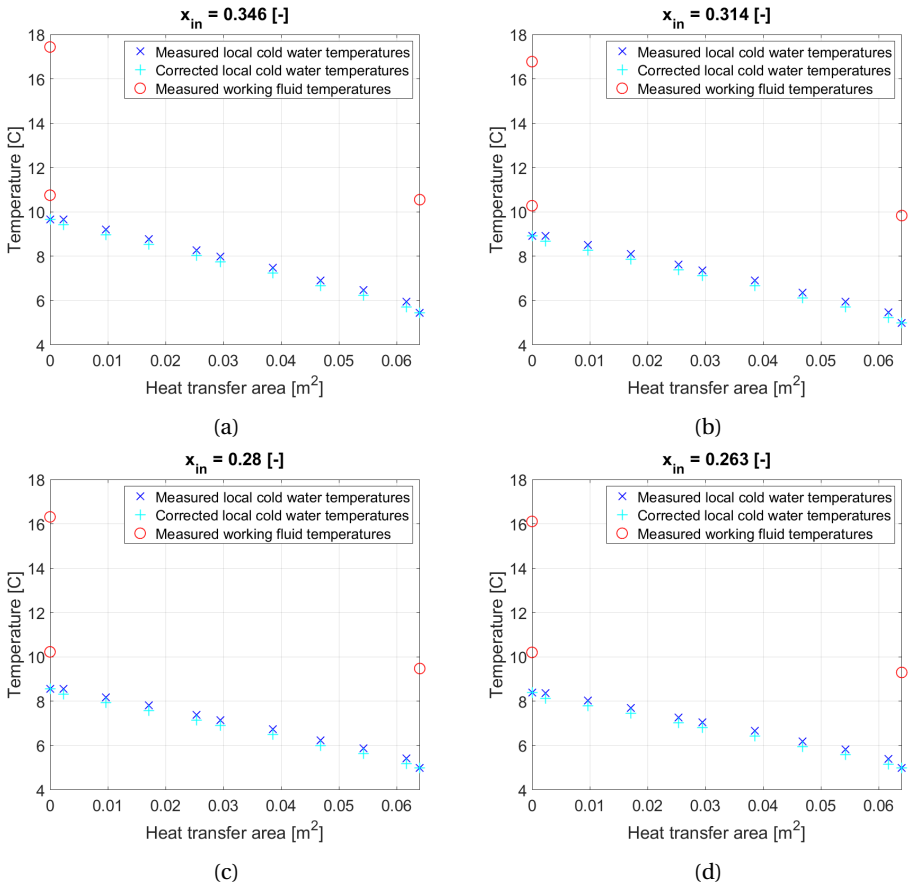

Figure 5.7: The measured temperatures T for various ammonia-water working fluid inlet vapour qualities x_{in}. The subfigures a to d show the liquid working fluid inlet temperature, the vapour working fluid inlet temperature, the working fluid outlet temperature, the cold water inlet and outlet temperatures and the local cold water temperatures in the condenser.

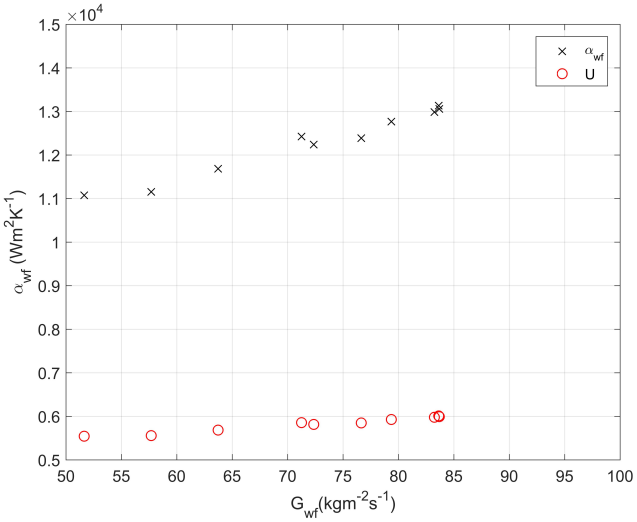

Figure 5.8: The convective heat transfer coefficient on the working fluid side α_{wf} and the overall heat transfer coefficient U versus the working fluid mass flux G_{wf} for the ammonia-water mixture condensation experiments. The working fluid mass flux range during the ammonia-water mixture experiments was 52 to 84 [kg/m^{2}s].

$$Pr_L = \frac{c_{p,L} \cdot \mu_L}{\kappa_L}. \tag{5.15}$$

where the liquid phase properties are determined using a thermodynamic library.

Figure 5.10 shows a comparison of convective heat transfer coefficient correlations for condensation, including the measured convective heat transfer coefficient for the measured working fluid mass flux range of 52 to 84 [kg/m^{2}s]. The measured convective heat transfer coefficient is close to the correlation by Han *et al.* [26], even though the correlation by Han *et al.* [26] was only validated in the mass flux range of 10 to 35 [kg/m^{2}s]. The correlation by Geschiere [25] (equation 4.13) contains the liquid Schmidt number Sc_L. The mass diffusivity D of the ammonia vapour into the liquid ammonia-water mixture is determined by using data by Conde [48]. Geschiere [25] assumed a liquid film is present over the entire surface and along the entire length of the heat transfer plate. It is unlikely this was the case during the ammonia-water mixture condensation experiments due to the arrangement of the mixing zone (figure 3.18). The difference between the convective heat transfer coefficients from the ammonia-water mixture condensation experiments and the convective heat transfer coefficients from equation 4.13 can be explained by this argument.

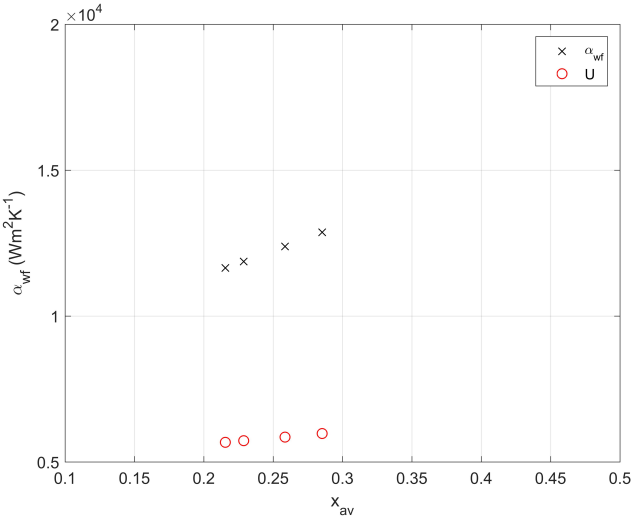

Figure 5.9: The convective heat transfer coefficient on the working fluid side α_{wf} and the overall heat transfer coefficient U versus the average vapour quality x_{av}, for measured vapour qualities in the range of 0.2 to 0.3 during the ammonia-water mixture experiments.

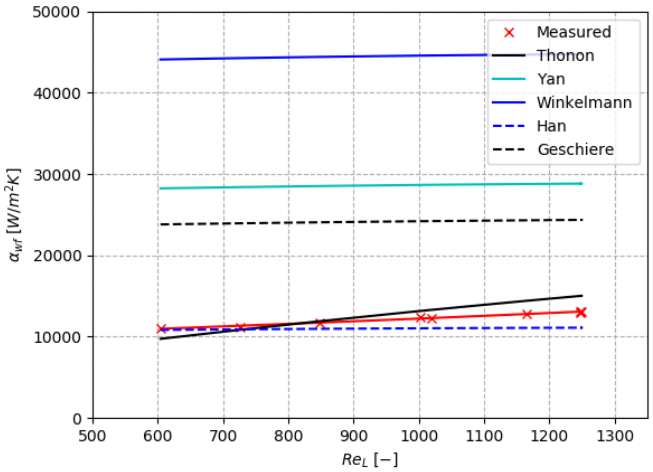

Figure 5.10: Comparison of convective heat transfer coefficient correlations for condensation versus the liquid Reynolds number Re_L for the ammonia-water mixture condensation experiments, including the measured data, Winkelmann [7], Thonon [18], Yan *et al.* [15], Geschiere [25] and Han *et al.* [26] (extrapolated). The working fluid mass flux range during the ammonia-water mixture experiments was 52 to 84 [kg/m^{2}s].

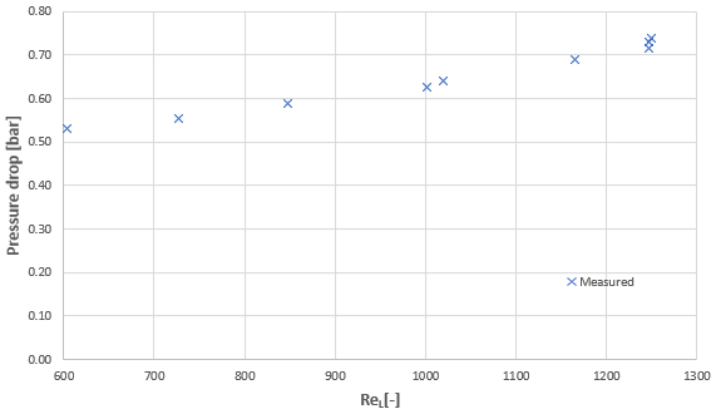

Figure 5.11: The working fluid pressure drop over the condenser versus the liquid Reynolds number Re_L, for measured liquid Reynolds numbers in the range of 604 to 1250 during the ammonia-water mixture experiments.

5.2.2. PRESSURE DROP

Figure 5.11 shows the pressure drop of the working fluid side for the single channel ammonia-water mixture condensation experiments. The fluid properties, such as the density ρ and the dynamic viscosity μ are not constant for two-phase flow in the heat exchanger. This means the pressure drop is not only dependent on the mass flux, as in the single phase flow case. However, as the change of vapour quality x was only around 0.15 during the ammonia-water mixture experiments, the density ρ and the dynamic viscosity μ did not vary much.

On the cold water side, the pressure drop due to elevation was taken into account. On the working fluid side, the pressure drop due to difference in vertical position of the in- and outlet pressure sensors will be neglected, as this difference is quite low (see figure 3.4).

Pressure drop in tubes To measure the pressure drop over the condenser on the working fluid side, the pressure sensor on the liquid line is used to determine the inlet pressure. Regarding the pressure drop in the stainless steel tubes between the in- and outlet pressure sensors on the working fluid side, again the equation in VDI [45] can be used:

$$\Delta P_{tube} = \xi \cdot \frac{L_{tube}}{d_{tube}} \cdot \frac{\rho_{wf} \cdot w_{wf}^2}{2} \tag{5.16}$$

The liquid line has an inner diameter of 6 [mm]. The maximum flow velocity of the liquid ammonia mixture w_L for the ammonia-water mixture condensation experiments is 0.71 [m/s]. As this liquid flow velocity is low, the pressure drop in the tubes of the liquid line can be neglected. However, around 20 [cm] before the inlet of the condenser on the working fluid side, the liquid line with an outer diameter of 8 [mm] is inside the vapour line with an inner diameter of 10 [mm] (see figure 3.6). The liquid ammonia-water mixture and the ammonia vapour are mixed when the liquid exits the 8 [mm] liquid line through spray holes (see figures 3.18 and 3.5). With a single channel arrangement, the liquid exits the spray holes and is mixed with the vapour flow before the inlet of the condenser. The mixed flow is flowing through a 1 [mm] circular gap (see figure 5.12). In order to calculate the pressure drop of the mixed flow in the gap between the liquid line and the vapour line, equation 5.16 can be used. The maximum liquid velocity is low, but the maximum vapour flow velocity is significant: $w_G = \dot{m}_G / \rho_G / (\frac{1}{4}\pi(0.010^2 - 0.008^2)) = 38.5$ [m/s]. Subsequently, the Reynolds number of the vapour flow Re_G in the gap is 1690.

As the flow is laminar, the drag coefficient ξ can be calculated with the following equation

$$\xi = \frac{64}{Re_G}, \tag{5.17}$$

leading to a drag coefficient ξ of 0.038. The pressure drop of the vapour flow in the gap then becomes $\Delta P_{tube} = 948$ [Pa]. This pressure drop is not significant enough to be taken into account.

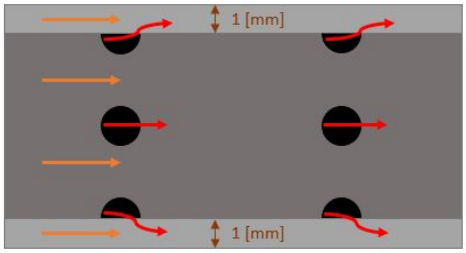

Figure 5.12: Schematic of the flow through the gap of 1 [mm] between the ammonia vapour line and the liquid line with spray holes. The red arrows indicate the liquid ammonia-water mixture flow coming out of the spray holes and the orange arrows indicate the ammonia vapour flow around the liquid spray tube.

Frictional pressure drop The Fanning friction factor on the working fluid side can be obtained from equation 4.16, when substituting the two-phase Fanning friction factor f_{TP} for the working fluid Fanning friction factor f_{wf} and using equation 4.19:

$$f_{wf} = \frac{\Delta P_f \cdot \rho_{av} \cdot d_h^3}{2 \cdot Re_{LO}^2 \cdot \mu_L^2 \cdot L_p}. \tag{5.18}$$

Now, for each of the measurements the Fanning friction factor can be obtained. The average density ρ_{av} is determined by the following equation

$$\rho_{av} = \frac{1}{v_{av}} = \frac{2}{v_{in} + v_{out}}, \tag{5.19}$$

where $v_{in} = 1/\rho_{in}$ is the specific volume at the inlet of the working fluid side and $v_{out} = 1/\rho_{out}$ is the specific volume at the outlet of the working fluid side.

The liquid phase density is determined by taking the average of the liquid phase density at the inlet and the liquid phase density at the outlet. In a similar way, the vapour phase density is determined by taking the average of the vapour phase density at the inlet and the vapour phase density at the outlet.

This leads to the following Fanning friction factor equation on the working fluid side for the measured mass flux range of $52 < G_{wf} < 84$ [kg/m^{2}s]:

$$f_{wf} = 270{,}000 \cdot Re_{eq}^{-1.5}. \tag{5.20}$$

This equation has a maximum error of 5% with respect to the measured Fanning friction factors. More experiments are needed to propose a Fanning friction factor correlation in a larger range.

Figure 5.13 shows a Fanning friction factor correlation comparison for condensing flow, including this research, Yan *et al.* [15], Han *et al.* [26] and Kuo *et al.* [27]. The correlation by Han *et al.* [26] is not validated for the measured mass flux range of $52 < G_{wf} < 84$, but it is extrapolated for this comparison. The measured Fanning friction factor does not correspond with any of the existing correlations.

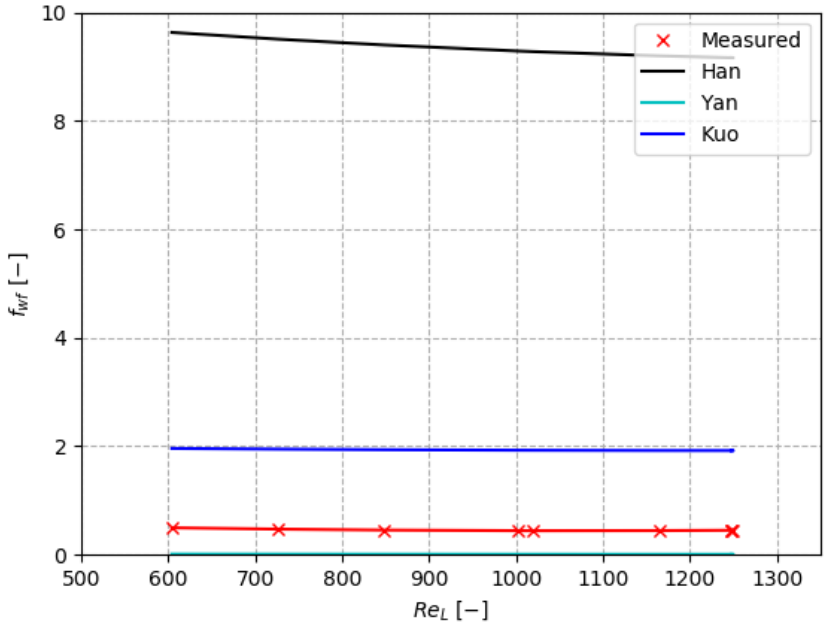

Figure 5.13: Fanning friction factor correlation comparison for condensing flow, including this research, Yan *et al.* [15], Han *et al.* [26] and Kuo *et al.* [27]. The measured mass flux range is $52 < G_{wf} < 84$ [kg/m^{2}s]. The correlation by Han *et al.* [26] is not validated for the measured mass flux range.

5.3. NUMERICAL MODEL RESULTS: AMMONIA-WATER MIXTURE

In this section, the results from the numerical condenser model discussed in chapter 4 will be shown and compared to the results from the ammonia-water mixture condensation experiments.

5.3.1. INPUTS

In section 4.2.1 the algorithm of the numerical condenser model was discussed. Figure 4.3 shows the required inputs of the model. The assumptions made in the model are listed in section 4.2.2.

Effective heat transfer area In section 3.5 the total effective heat transfer area for the gasketed heat exchanger was determined. The effective heat transfer area $A_{e,gasketed}$ is equal to 0.512 [m^2] for the maximum number of eight effective plates. During the ammonia-water mixture condensation experiments, a single channel configuration was used (see figure 3.18), so all heat was transferred through one effective plate. The effective area for the ammonia-water mixture experiments was equal to $0.512/8 = 0.064$ [m^2].

Convective heat transfer coefficients The single phase convective heat transfer coefficient is determined from the water-water experiments (see section 5.1.1). Equation 5.1 was proposed for single phase flow.

The two-phase convective heat transfer coefficients for all the measurement points are determined from the ammonia-water mixture experiments (see section 5.2.1 and figure 5.8). Equation 5.14 is used in the model for the measured mass flux range of $52 < G_{wf} < 84$ [kg/m^{2}s].

Pressure drop The single phase pressure drop and Fanning friction factor are determined from the water-water experiments (see section 5.1.2). Equation 5.10 is proposed for single phase flow. With respect to the two-phase working fluid flow, equation 5.20 is used in the model for the measured mass flux range of $52 < G_{wf} < 84$ [kg/m^{2}s].

Working fluid inlet temperature Figure 3.18 shows how the ammonia vapour flow and the ammonia-water mixture liquid flow are mixed at the inlet of the condenser. As discussed in section 4.1.1, the working fluid

inlet temperature $T_{wf,in}$ can be determined from a thermodynamic library by using the mixed enthalpy $h_{mix,wf,in}$ of the two flows, the working fluid inlet pressure $P_{wf,in}$ and the combined concentration X_{wf} of the two flows.

Figure 5.14 shows the enthalpy-concentration diagram for ammonia-water mixtures, with the ammonia vapour inlet flow enthalpy and the ammonia-water liquid inlet flow enthalpy, for a total working fluid mass flow of $\dot{m}_{wf} = 0.0136$ [kg/s]. The liquid inlet working fluid concentration X_L is 0.876 and the combined working fluid concentration X_{wf} is 0.909. (concentrations obtained from the REFPROP library [47]).

5.3.2. COMPARISON OF THERMODYNAMIC LIBRARIES

Two different thermodynamic libraries were tried in the model: the REFPROP library by the National Institute of Standards and Technology [47] and the AmmoniaWaterProp library based on the work by Rattner and Garimella [49] (specific for ammonia-water mixtures). The Rattner library was used for ammonia-water mixtures in the model by Goudriaan [2] and Kuikhoven [3].

Concentration The concentration of the working fluid flow X_{wf} can be determined iteratively by using the measured temperature, the pressure and the density of the working fluid. Goudriaan [2] made a comparison between the Rattner and REFPROP library (see figure 5.15). At a certain temperature, the corresponding concentrations of the two libraries differ significantly.

Figure 5.16 shows the calculated temperature profiles by the numerical model compared to the experimentally measured temperatures, for a mass flow of $\dot{m}_{wf} = 0.0136$ [kg/s]. The figures include the measured temperatures on the working fluid and cold water side and the calculated temperature profiles on the working fluid and cold water side. The inlet working fluid temperature is also calculated by the model. Figure 5.17 shows the results when the REFPROP library is used ($X_{wf} = 0.909$) and figure 5.16b shows the results when the Rattner library is used ($X_{wf} = 0.956$). When the REFPROP library is used, the calculated temperatures correspond well with the measured temperatures. The absolute difference in working fluid outlet temperature is 0.06 [°C] (-0.62 %) and the absolute difference in cold water inlet temperature is 0.054 [°C] (-1.07 %). When the Rattner library is used, the absolute difference in working fluid outlet temperature is 0.57 [°C] (-6.0 %) and the absolute difference in cold water inlet temperature is 0.87 [°C] (+17.3 %) for a working fluid mass flow of $\dot{m}_{wf} = 0.0136$ [kg/s].

The model is significantly more accurate at predicting the working fluid outlet temperature and the cold water inlet temperature when the REFPROP library is used. The model was not only inaccurate for a mass flow of $\dot{m}_{wf} = 0.0136$ [kg/s] when the Rattner library was used, but the for all the mass flow input values.

The difference in calculated concentration between the thermodynamic libraries is quite high ($X_{wf} = 0.909$ for REFPROP and $X_{wf} = 0.956$ for Rattner). The inaccurate results from the model when Rattner is used, could be caused by an incorrect determination of the concentration when the Rattner library is used. Other calculations for which a thermodynamic library is used, such as the working fluid inlet and outlet temperatures per control volume, could still be accurate when the Rattner library is used. Figure 5.17 shows the results when the REFPROP library is used to calculate the concentration and the Rattner libary is used for the other calculations that require a thermodynamic library. In this case, the absolute difference in working fluid outlet temperature is 0.81 [°C] (+8.4 %) and the absolute difference in cold water inlet temperature is 0.82 [°C] (-16.5 %) for a working fluid mass flow of $\dot{m}_{wf} = 0.0136$ [kg/s]. Thus, using the Rattner library in the model leads to inaccurate temperature profile predictions. The REFPROP library will be used to generate numerical model results for different mass flows $\dot{m}_{wf}$.

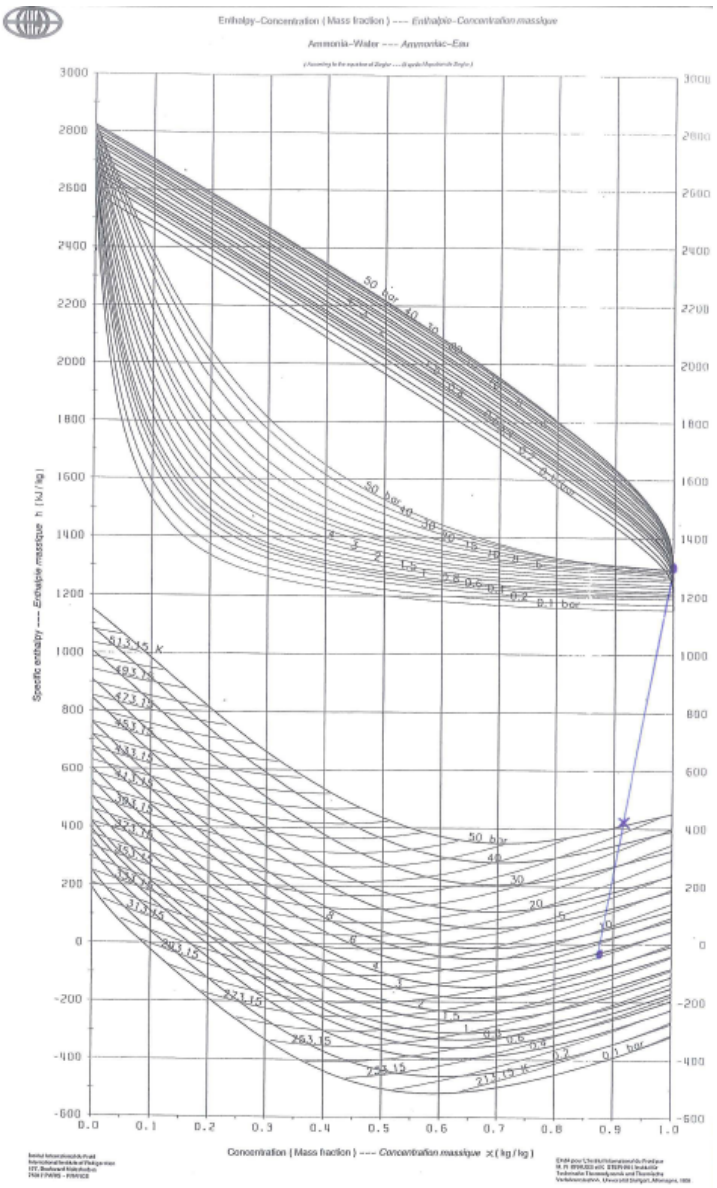

Figure 5.14: The enthalpy-concentration diagram for ammonia-water mixtures (Krauss and Stephen [28]), with the turbine outlet flow enthalpy and the liquid valve outlet flow enthalpy, for one of the measurement points. The mixed enthalpy and concentration lay between the turbine outlet and valve outlet points.

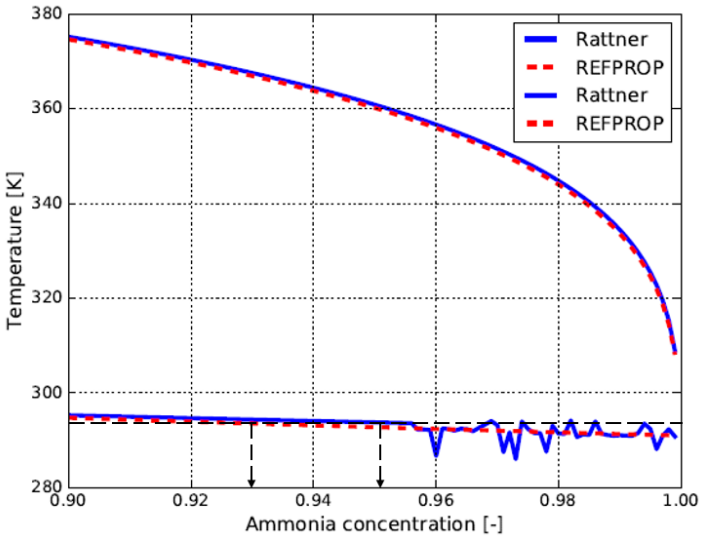

Figure 5.15: Temperature versus concentration diagram for ammonia-water mixtures: a comparison between the Rattner and REFPROP thermodynamic libraries, from Goudriaan [2]. The calculated concentration varies significantly between the libraries for a certain temperature, indicated by the arrows.

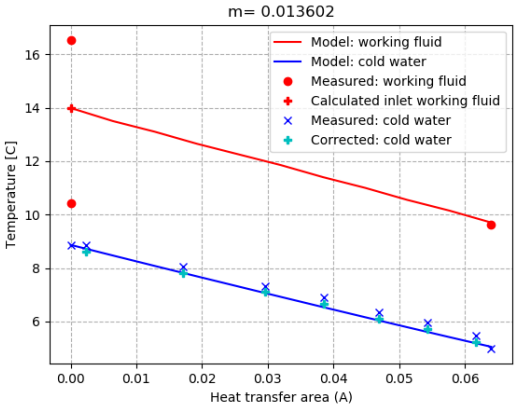

(a) Results for $\dot{m}_{wf} = 0.0136$ $[kg/s]$ using REFPROP ($X_{wf} = 0.909$).

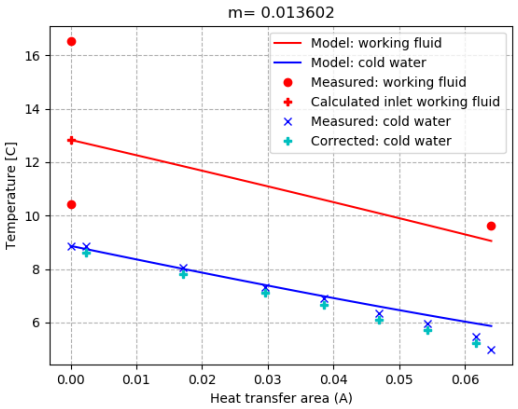

(b) Results for $\dot{m}_{wf} = 0.0136$ $[kg/s]$ using Rattner ($X_{wf} = 0.956$).

Figure 5.16: The temperature profiles calculated from the numerical condenser model compared to the measured temperatures T for a working fluid mass flow of $\dot{m}_{wf} = 0.0136$ [kg/s]. Figure a shows the results when the REFPROP library is used and figure b shows the results when the Rattner library is used. A significant difference between the temperature profiles calculated by the model and the measured temperatures can be observed.

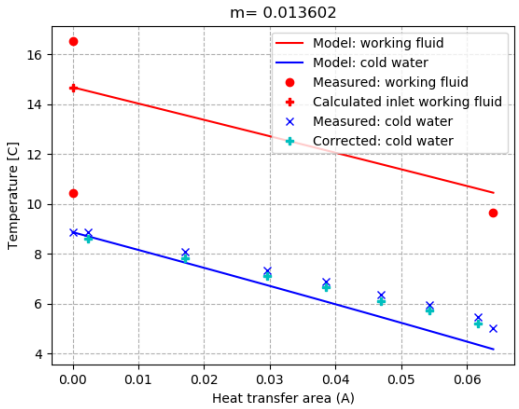

Figure 5.17: The temperature profiles calculated from the numerical condenser model compared to the measured temperatures T for a working fluid mass flow of $\dot{m}_{wf} = 0.0136$ [kg/s], when REFPROP is used for the concentration calculation ($X_{wf} = 0.909$) and Rattner is used for the other calculations.

5.3.3. RESULTS: VARYING MASS FLOW

In this section, the calculated temperature profiles by the numerical model compared to the experimentally measured temperatures will be shown for different working fluid mass flows $\dot{m}_{wf}$. In the previous section the conclusion was made that the REFPROP library should be used in the model to obtain the most accurate results. Figure 5.18 shows the temperature profiles calculated from the numerical condenser model compared to the measured temperatures T for four different working fluid mass flows $\dot{m}_{wf}$. The difference between the measured and calculated temperature on the working fluid side is max. 3.5%, at $\dot{m}_{wf} = 0.0084$ [kg/s]. The difference between the measured and calculated temperature on the cold water side is max. 2.1%, also at $\dot{m}_{wf} = 0.0084$ [kg/s].

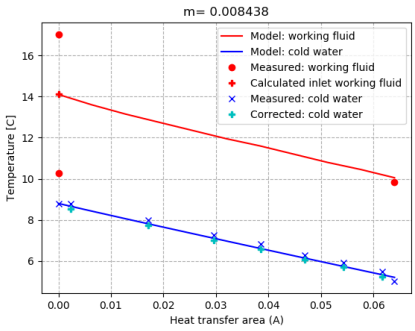

(a) Results for a working fluid mass flow of $\dot{m}_{wf} = 0.0084$ [kg/s].

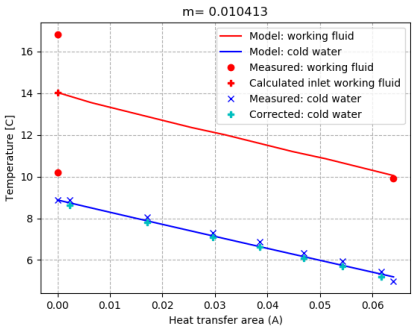

(b) Results for a working fluid mass flow of $\dot{m}_{wf} = 0.0104$ [kg/s].

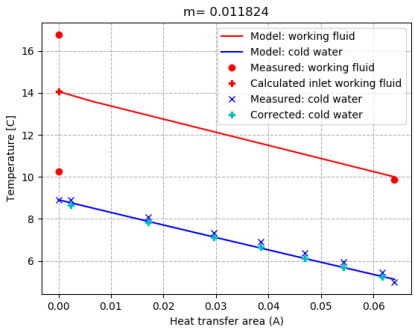

(c) Results for a working fluid mass flow of $\dot{m}_{wf} = 0.0118$ [kg/s].

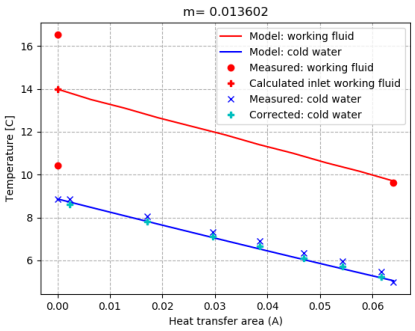

(d) Results for a working fluid mass flow of $\dot{m}_{wf} = 0.0136$ [kg/s].

Figure 5.18: The temperature profiles calculated from the numerical condenser model compared to the measured temperatures T for four different working fluid mass flows $\dot{m}_{wf}$.

5.4. AMMONIA CONDENSATION EXPERIMENTS

Similar to the ammonia-water mixture condensation experiments, pure ammonia experiments were also executed. This way, a comparison of the results from the pure ammonia experiments can be made to the results from the ammonia-water experiments.

Input parameters The pure ammonia condensation experiments were done with a single channel arrangement. During the ammonia condensation experiments, the working fluid flow (pure ammonia) was varied. Measurements were done on the following working fluid mass flows $\dot{m}$: 0.0060 [kg/s], 0.0068 [kg/s], 0.0072 [kg/s], 0.0077 [kg/s], 0.0086 [kg/s], 0.0094 [kg/s], 0.0108 [kg/s], 0.0120 [kg/s], 0.0132 [kg/s] and 0.0141 [kg/s] (see table 5.4). The corresponding mass fluxes G_{wf} and vapour qualities x are shown in table 5.4.

The working fluid mass flux influenced the vapour fraction (see figure 5.19). During the ammonia experiments, the cold water inlet temperature was constant at 8 [°C]. This temperature is higher than the cold water temperature during the ammonia-water mixture experiments (5 [°C]). The cooling capacity was not sufficient to reach 5 [°C] during the pure ammonia experiments. Similar to the ammonia-water mixture experiments, the cold water flow was constant at 0.012 [L/s].

Table 5.4: The set mass flows for the pure ammonia condensation experiments with the corresponding mass fluxes and vapour qualities.

Mass flow $\dot{m}_{wf}$ [kg/s]	0.0060	0.0068	0.0072	0.0077	0.0086	0.0094	0.0108	0.0120	0.0132	0.0141
Mass flux G_{wf} [kg/m^{2}s]	36.67	41.81	43.99	47.43	52.87	57.54	65.85	73.66	80.72	86.29
Vapour inlet quality x_{in}	0.329	0.292	0.273	0.247	0.218	0.199	0.145	0.126	0.112	0.108
Average vapour quality x_{av}	0.248	0.222	0.206	0.186	0.164	0.150	0.103	0.090	0.079	0.077
Vapour outlet quality x_{out}	0.167	0.152	0.140	0.124	0.110	0.101	0.062	0.053	0.045	0.046

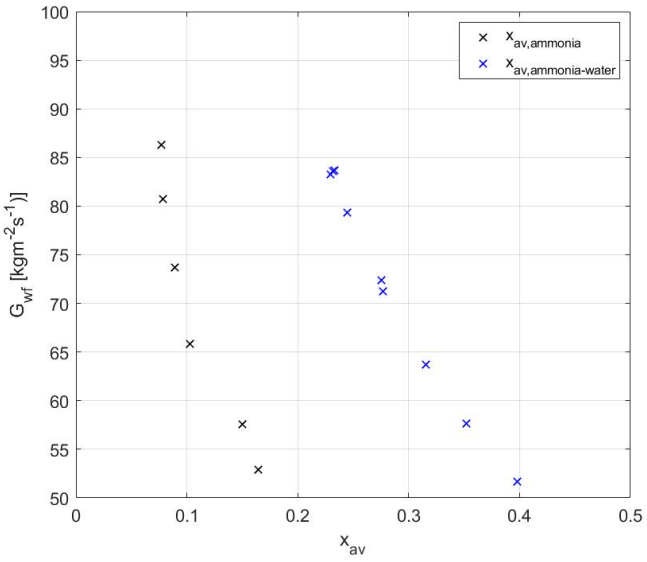

Figure 5.19: The working fluid mass flux G_{wf} versus the average vapour quality x_{av} during the pure ammonia experiments. The measured working fluid mass flux range is 37 to 86 [kg/m^{2}s].

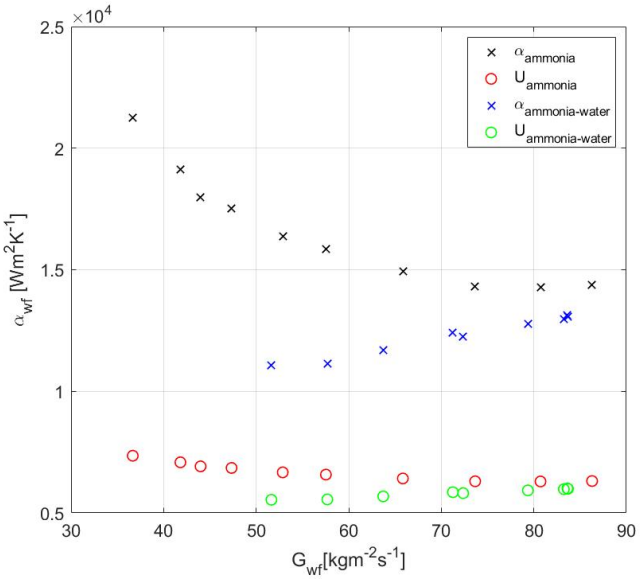

Figure 5.20: Comparison of the pure ammonia and ammonia-water mixture data regarding the convective heat transfer coefficient α and the overall heat transfer coefficient U. The working fluid mass flux range G_{wf} during the pure ammonia experiments was 37 to 86 [kg/m^{2}s] and 52 to 84 [kg/m^{2}s] during the ammonia-water mixture experiments.

5.4.1. HEAT TRANSFER AND TEMPERATURE PROFILES

Figure 5.22 shows the measured temperatures for the different pure ammonia working fluid mass flows at the corresponding positions on the heat transfer plate. The red circles show the measured temperatures on the working fluid side. At the working fluid inlet, both the liquid and the vapour inlet are shown, where the vapour flow is the highest temperature of the two. The measured cold water temperature profile is shown by dark blue points. The cold water temperature profile is linear for all the working fluid mass flows. The fact that the temperature on the working fluid side is not constant along the length of the heat transfer plate for all the ammonia mass flows, can be explained by the fact that the liquid is cooled before all the vapour is condensed. Geschiere [25] discusses this phenomenon.

Issues Between the ammonia-water mixture condensation experiments and the pure ammonia condensation experiments another local temperature sensor malfunctioned (the first sensor counting from the cold water outlet side). Thus, in total three of the nine sensors were not operational during the pure ammonia condensation experiments. No interpolation was used this time, as two local temperature sensors next to each other malfunctioned and the interpolation would be too inaccurate.

Heat transfer coefficients Figure 5.20 shows a comparison of the pure ammonia and ammonia-water mixture data regarding the convective heat transfer coefficient α and the overall heat transfer coefficient U versus the working fluid mass flux G_{wf}. Contrary to the ammonia-water mixture experiments, the convective and overall heat transfer coefficients decrease for increasing mass flux. The increasing mass flux corresponds with a lower vapour quality (see figure 5.19) and the range of vapour qualities is not comparable to the ammonia-water experiments. More experiments are needed in which only the vapour quality x or the working fluid mass flux G_{wf} is varied.

5.4.2. PRESSURE DROP

Figure 5.21 shows a comparison of the pressure drop over the working fluid side between the ammonia-water mixture experiments and the pure ammonia experiments. For equal working fluid mass flux G_{wf}, the pressure drop is slightly higher for pure ammonia compared to the ammonia-water mixture. This can be caused by the difference in average density of the working fluid in the condenser. The fact that pure ammonia has a lower density than ammonia-water mixtures explains why the pressure drop is higher for pure ammonia (see equation 4.16). This is also supported by the fact that the trend of the pressure drops is similar.

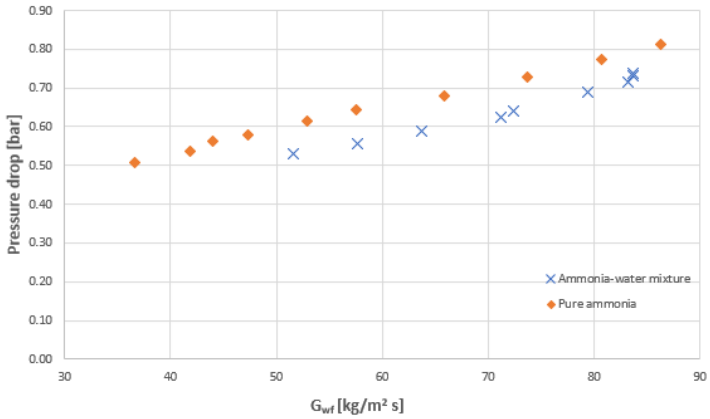

Figure 5.21: Comparison of the pressure drop over the working fluid side between the ammonia-water mixture experiments and the pure ammonia experiments, in the mass flux range of $37 < G_{wf} < 86$ [kg/m^{2}s].

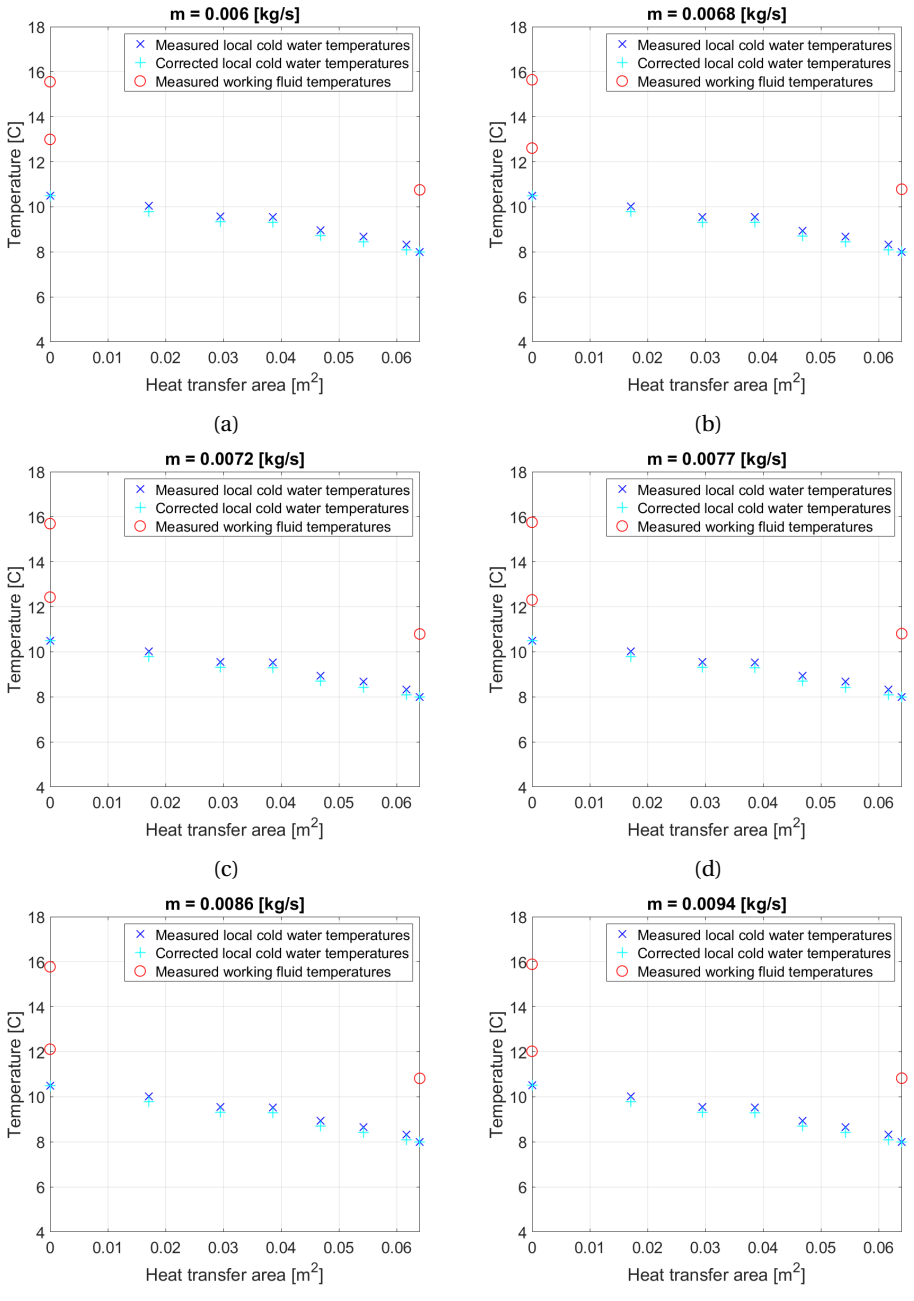

Figure 5.22: The measured temperatures T for various pure ammonia working fluid mass flows m_{wf}, versus the heat transfer area A. The subfigures a to j show the liquid working fluid inlet temperature, the vapour working fluid inlet temperature, the working fluid outlet temperature, the cold water inlet and outlet temperatures and the local cold water temperatures in the condenser.

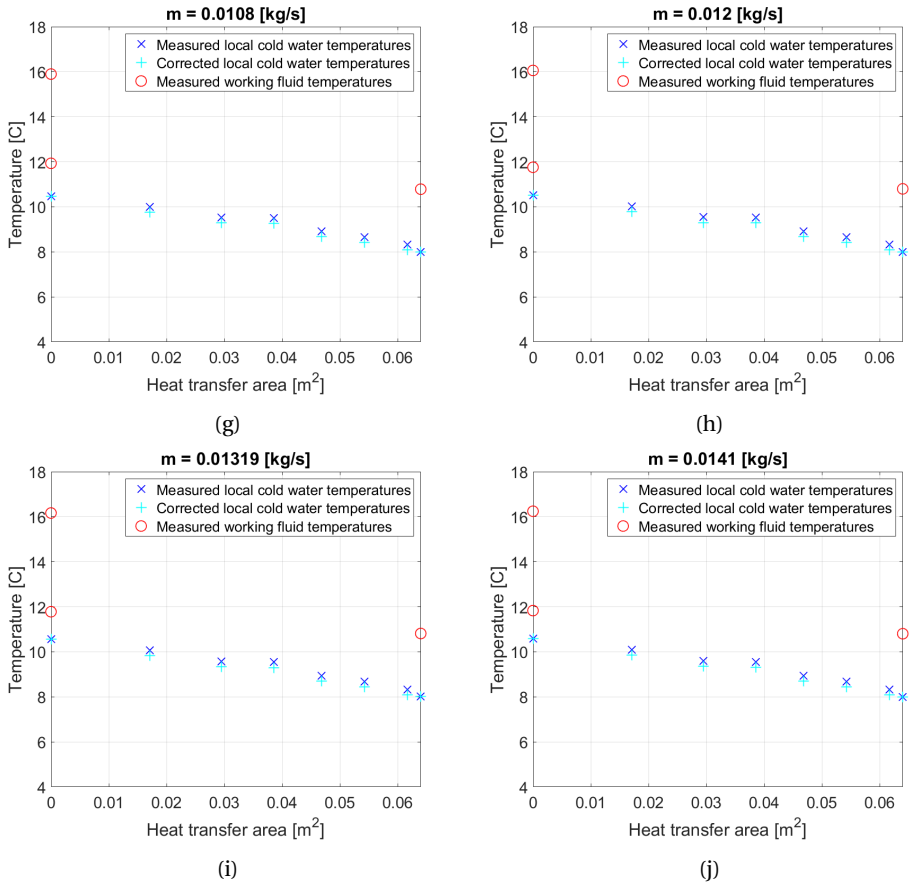

Figure 5.22: The measured temperatures T for various pure ammonia working fluid mass flows m_{wf}, versus the heat transfer area A. The subfigures a to j show the liquid working fluid inlet temperature, the vapour working fluid inlet temperature, the working fluid outlet temperature, the cold water inlet and outlet temperatures and the local cold water temperatures in the condenser (continued).

6

CONCLUSION AND RECOMMENDATIONS

6.1. CONCLUSION

In this thesis, a framework has been made for future research on condensing flow in plate heat exchangers. Research on condensing flow in plate heat exchangers is an important step to make OTEC power generation more economically attractive.

In section 1.4 the objectives of this thesis were discussed. To what degree the objectives were achieved, is discussed in the following paragraphs:

OTEC-demo extension The OTEC-demo set-up is extended with a gasketed heat exchanger, which can be used as condenser. This heat exchanger is implemented in such a way that the existing condenser can be used as a subcooler. New sensors are implemented to make it possible to measure the inlet and outlet temperatures and pressures of the new condenser. Also, nine miniature temperature sensors are placed along the endplate of gasketed heat exchanger in the direction of the flow, which allow the temperature to be measured locally in the condenser. This way, temperature profiles and local heat transfer coefficients can the determined in the condenser. A differential pressure sensor over the gasketed heat exchanger was added to the set-up.

Visualization section parts A transparent corrugated endplate and a pressure plate with window are designed and fabricated to create the possibility to visualize the two-phase flow in the condenser. This way, in future experiments flow patterns can be identified in the condenser, which allows modification of the flow pattern maps proposed by Tao *et al.* [13].

Water/water experiments From the water/water experiments, a pressure drop correlation and a convective heat transfer coefficient correlation have been proposed for single phase flow in the condenser. These correlations are validated in the Reynolds number range of $725 < Re < 2472$.

Ammonia-water mixture condensation experiments For all the working fluid mass flows and vapour fractions, the cold water temperature profile was linear, which indicates convective heat transfer coefficient on the working fluid side did not change much along the length of the heat transfer plate. This can be explained by the small change in vapour quality during the ammonia-water mixture condensation experiments. The convective heat transfer coefficient increased for increasing working fluid mass flux. The convective heat transfer coefficient also increased for increasing inlet working fluid vapour fraction. More experimental data are required to propose a general convective heat transfer coefficient correlation, specifically on different ammonia-water concentrations and pure ammonia. More experiments, in which more parameters are varied, are also required to propose a two-phase pressure drop correlation.

Model verification The REFPROP thermodynamic library is used in the developed numerical model. Using the Rattner thermodynamic library in the model produced inaccurate results. The numerical model can predict the measured working fluid outlet temperature and the cold water inlet temperature within an accuracy

of 4%, for the ammonia-water mixture experiments. This means the assumptions made in the model are valid for the ammonia-water mixture condensation experiments.

Pure ammonia condensation experiments The convective and overall heat transfer coefficients decreased for increasing mass flux during the pure ammonia experiments. During the ammonia-water mixture experiments, the convective and overall heat transfer coefficients increased for increasing mass flux. However, no conclusions can be made based on the current datasets, as the average vapour fractions differed between the pure ammonia and ammonia-mixture experiments. For equal working fluid mass flux, the pressure drop is slightly higher for pure ammonia compared to the ammonia-water mixture. This is probably caused by the difference in average density between pure ammonia and an ammonia-water mixture.

6.2. RECOMMENDATIONS

The following recommendations for further research are proposed:

- Propose lighting and a camera so visualization experiments can be executed. Check if the two phases can clearly be distinguished. Execute visualization experiments to identify flow patterns. Compare the results to the flow pattern maps proposed by Tao *et al.* [13]. Investigate the distribution over the plates at the condenser inlet and check whether the assumption of homogeneous mixing of the liquid and vapour flows is valid. Propose a set-up for multi-channel visualization.
- Perform more experiments with the local temperature sensors on varying mass based ammonia concentrations, between 100% and 90% ammonia concentration. Further analyse the pure ammonia experiments. Perform multi-channel experiments. Compare the results and check the influence of the number of channels. Propose a convective heat transfer coefficient correlation and a pressure drop correlation for the working fluid side. Compare the relations for different ammonia concentrations.
- Research the accuracy of the AmmoniaWaterProp (Rattner) thermodynamic library.

A

MULTICHANNEL VISUALIZATION SECTION DESIGN

Before building the visualization section, some designs are made. Two separate cases are defined: a single channel visualization set-up (one channel per fluid) and a multi-channel visualization set-up. In this thesis, it was proposed to do visualization experiments with a single channel arrangement. In this appendix, the multi-channel visualization set-up will be discussed. These designs will not be further used for experiments in this thesis.

The problem with the multi-channel arrangement lies in the fact that the visualized working fluid flow only transfers heat in one direction (see figure A.1). This is not characteristic for all condensing working fluid flows in a heat exchanger with a multi-channel configuration, as one or more working fluid flows transfer heat to two sides.

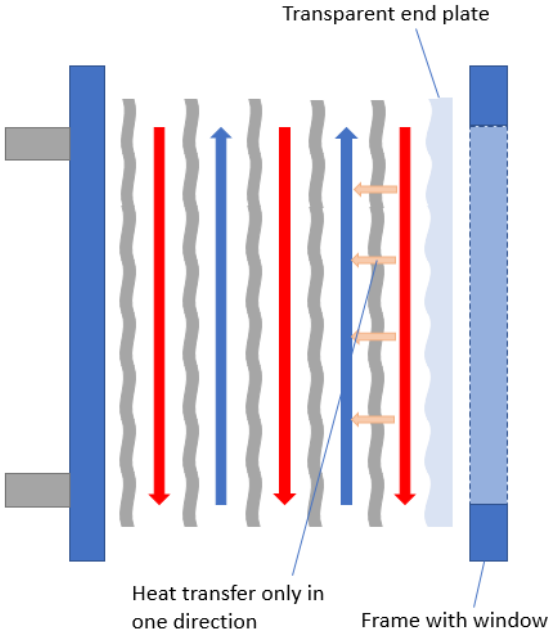

Figure A.1: Simplified side view of a possible multichannel visualization set-up for the OTEC-demo

Figure A.2 shows how the previously discussed problem can be solved. Another transparent cold fluid flow will be added, which requires another corrugated transparent plate as well. Now, the visualized working fluid flow is cooled from two sides, making the visualization more representative.

This set-up is a lot more complicated. Firstly, the thermal conductivity of the transparent material is a lot lower than the thermal conductivity of the standard stainless steel material. The decrease in heat transfer needs to be compensated by using a different fluid with a lower viscosity or by increasing the temperature difference over the plastic plate, thus making the cold water flow colder.

Also, the fact that one would have to look through two transparent plates with corrugation and a cooling fluid, could make it difficult to distinguish flow patterns in the working fluid flow.

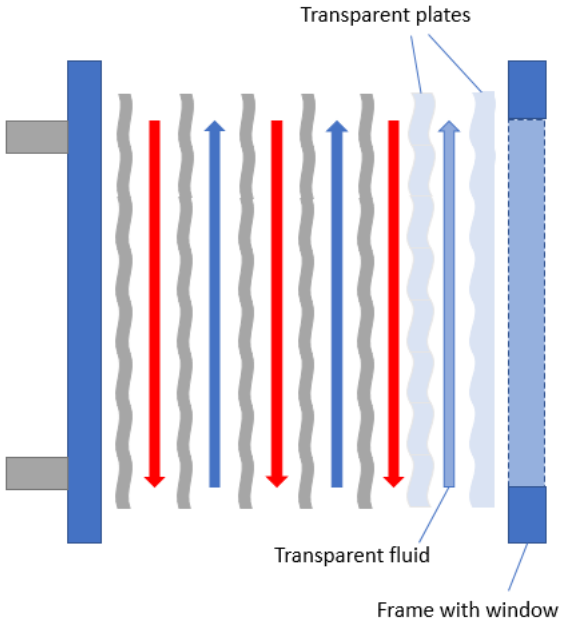

Figure A.2: Simplified side view of a possible multichannel visualization set-up for the OTEC-demo

B

STANDARD CONFIGURATION MEASUREMENTS

Before doing measurements to investigate the transport phenomena in an ammonia(-water) condenser, the standard configurations of the working fluid flow and ammonia concentration in the cycle will be decided. These experiments were done using the set-up before the extension of the set-up, so the brazed heat exchanger was used.

B.1. INPUT PARAMETERS

The standard configurations are defined by doing measurements with varying working fluid flow and concentration. Figure B.1 shows an overview of the ammonia concentration and the working fluid flow of all the measurements. As can be seen in the figure, four configurations (with small deviations) were used for the working fluid flow $\dot{m}$, 0.013 [kg/s], 0.010 [kg/s], 0.007 [kg/s] and 0.005 [kg/s].

On the cold water side, the temperature of the inlet flow was set to a constant value of $T_{water,in} = 5$ [°C] (which represents deep seawater at 1 [km] depth) and the temperature of the outlet flow was kept constant at $T_{water,out} = 10.5$ [°C]. This constant temperature difference corresponded to a constant ammonia vapour flow at the inlet of the condenser of around $\dot{m}_G = 0.004$ [kg/s]. The mass flow was set to a constant value of $\dot{m}_{water} = 0.225$ [L/s] at the cold water side of the condenser.

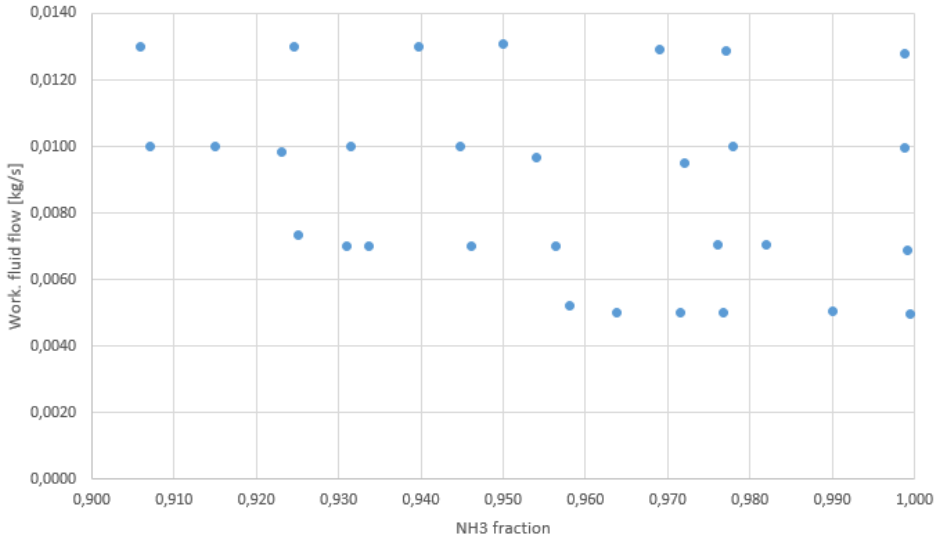

Figure B.1: Overview of all the measurement points

B.2. RESULTS

B.2.1. OVERALL HEAT TRANSFER COEFFICIENT

The results in figure B.2 show a clear trend, a higher ammonia concentration in the ammonia-water mixture leads to a higher overall heat transfer coefficient U. The working fluid mass flow also seems to influence the overall heat transfer coefficient a bit. A higher working fluid mass flow leads to a higher overall heat transfer coefficient.

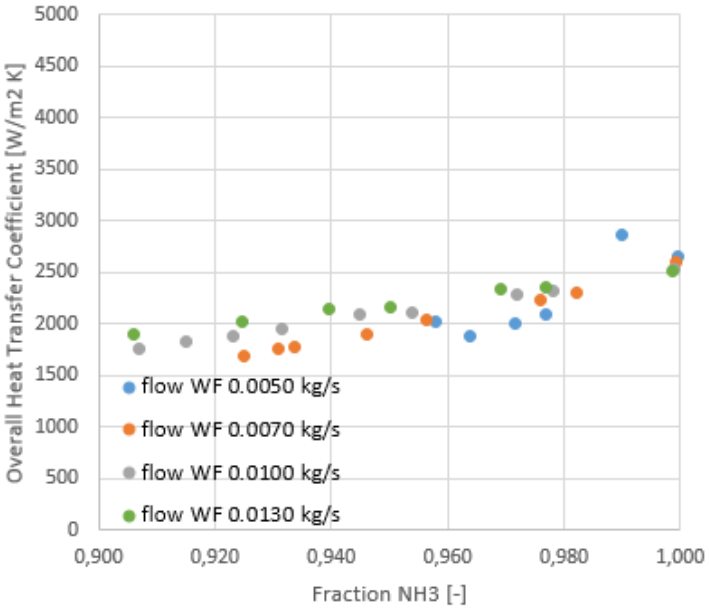

Figure B.2: Overall heat transfer coefficient U for varying concentration and working fluid flow

B.2.2. PRESSURE DROP

The pressure drop over the condenser was also investigated. The results in figure B.3 show that the pressure drop decreases for higher concentration. The working fluid mass flow does not seem to have an influence on the pressure drop over the condenser.

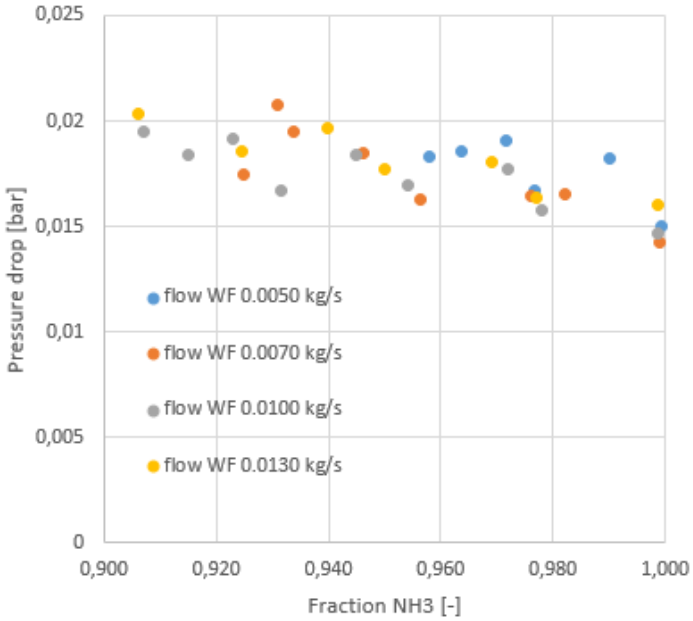

Figure B.3: Pressure drop over the condenser for varying concentration and working fluid flow

B.3. DISCUSSION

Initially, the plan was to do tests for 6 different ammonia concentrations, 100%, 98%, 96%, 94%, 92% and 90%. However, since the variation of the working fluid flow influenced the concentration (it was observed that the level of the tanks in the cycle changed with varying working fluid flow), there were a lot more variations in the concentrations than planned. The obtained data is still relevant, as the measured data can still show a trend.

C

OTEC-DEMO FRAME EXTENSION

In order to fit another heat exchanger in the OTEC-demo set-up, the frame of the set-up needed to be extended. In this chapter the sketches of the extended frame are shown.

C.1. FRONT VIEW

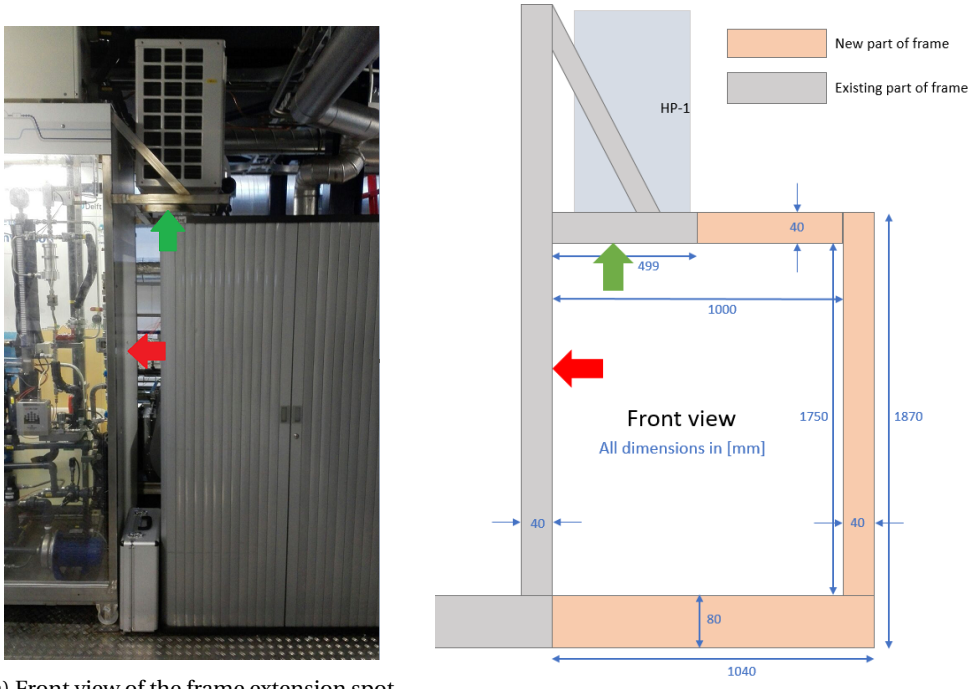

(a) Front view of the frame extension spot.

(b) Front view sketch of the designed frame extension.

Figure C.1: Front view of the frame extension.

C.2. SIDE VIEW

(a) Side view of the frame extension spot.

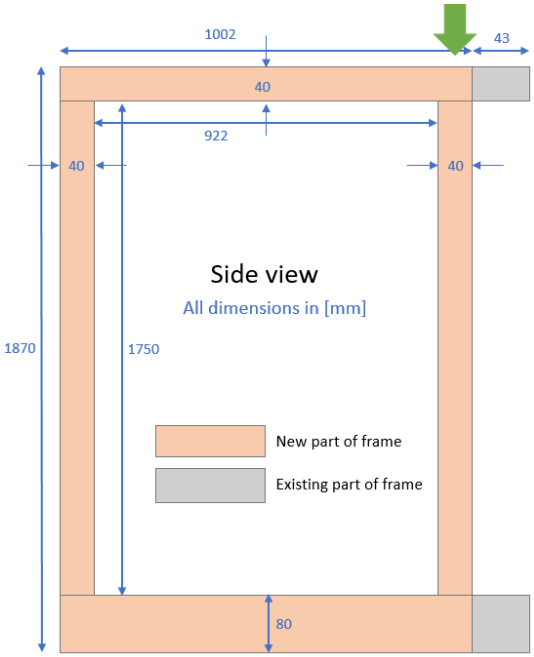

(b) Side view sketch of the designed frame extension.

Figure C.2: Side view of the frame extension.

C.3. RAILS AND STRIPS

Both at the front and the side, a rail and a strip need be constructed so transparent plates, similar to the current ones, can be used. The rails need to be placed just under the top horizontal bar and the strips need to be placed just on top of the bottom horizontal bar.

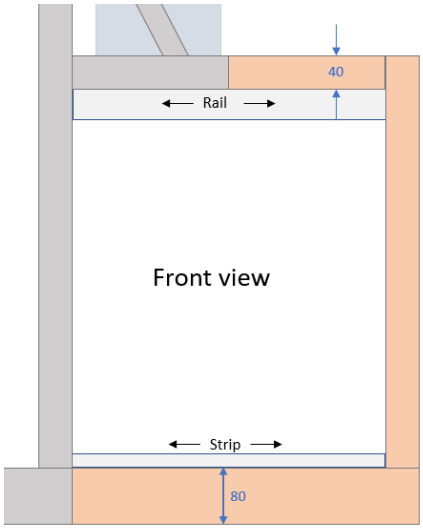

(a) The strip and the rails on the front view.

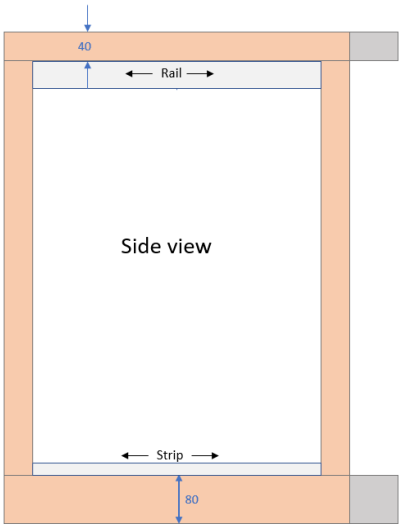

(b) The strip and the rails on the side view.

Figure C.3: The position of the strip and the rails in the frame extension.

(a) The strip on the frame.

(b) The rail of the frame.

Figure C.4: The position of the strip and the rails in the frame extension.

C.4. SUSPENSION POINTS

At the back of the frame, suspension points need to be added, similar to the current ones.

(a) A suspension point.

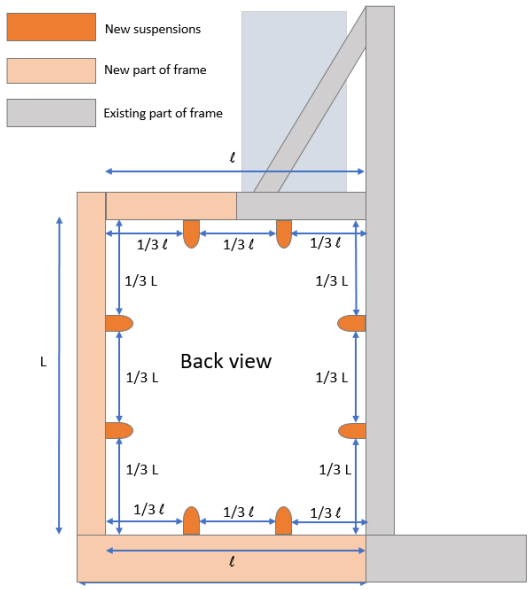

(b) Sketch of frame extension with suspension points.

Figure C.5: The suspension points in the frame extension.

D

PREVIOUS ARRANGEMENTS

In this appendix, the old arrangements of the parts that have been changed for the extension of the OTEC-demo are shown.

Figure D.1 shows the arrangement of the old mixing zone of the brazed heat exchanger.

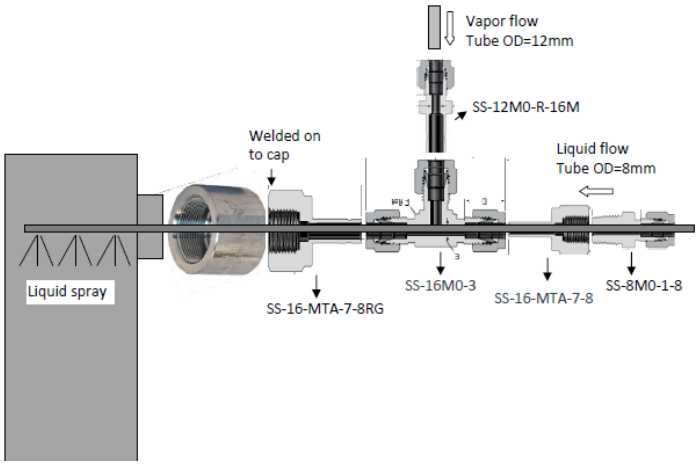

Figure D.1: Arrangement of the old mixing zone of the brazed gasket heat exchanger, including the Swagelok® part numbers.

Figure D.2 shows a schematic of the PVC piping of the old condenser set-up of the cold water side inlet. As there is limited space for the PVC piping, it is important that the lengths of some relevant parts are indicated.

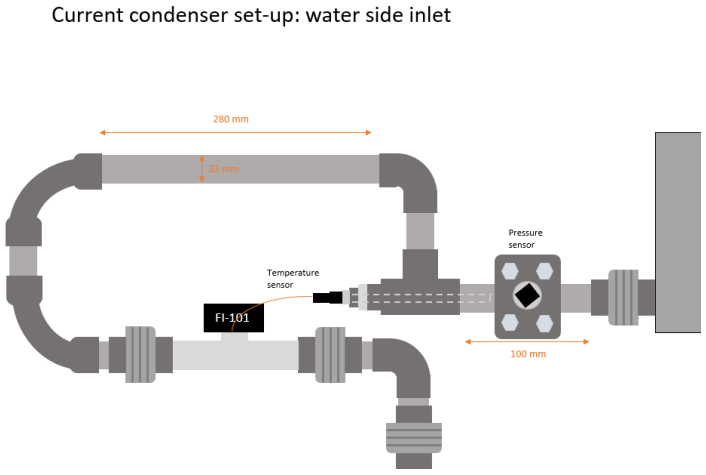

Figure D.2: The old arrangement of the PVC piping on the cold water side inlet side.

E

COOLING CAPACITY EXPERIMENT

In order to check the maximum heat transfer in the condenser, the cooling capacity of the heat pump needed to be investigated. The heat pump (see figure E.1) is used to cool down the water in the cold water tank. A set of experiments was performed, in which the heat transfer in the condenser was calculated from the measured temperatures and mass flow, for varying cold water temperature. Figure E.2 shows the results of the experiment. The cooling capacity seems to have a close to linear correlation with the cold water temperature.

Figure E.1: Image of the heat pump

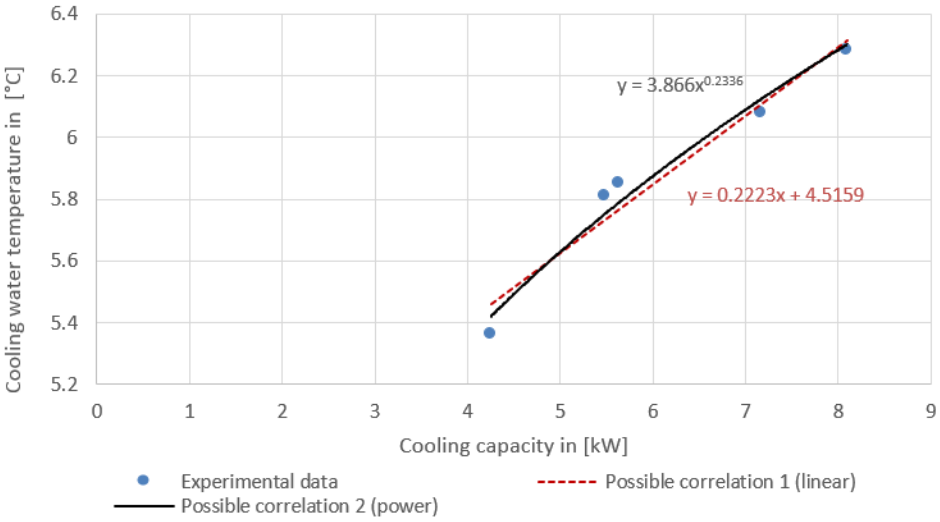

Figure E.2: The cooling capacity of the OTEC-demo for varying cold water temperature

F

RELEASE VALVES ARRANGEMENT

The pressure difference over the condenser will be measured with the Siemens SITRANS P500 pressure transmitter. A 5-way valve manifold (see figures F.1 and F.2) had to be connected to the P500 in for the following reasons:

- Valves A-B make it possible to isolate the P500.
- Valve B-B is required for levelling the high and low pressure side, so it makes calibration possible.
- Valves A-C give the possibility to release pressure from the system.

The process connections (A) are obviously connected to the working fluid lines at respectively the in- and outlet of the condenser, but the release valves can be connected to various instruments. A drain tank and a ventilation pipe are available for the set-up. Figure F.3 shows some of the possible arrangements of the lines connected to the 5-way valve manifold.

It was decided to connect the release valves to the drain tank. The lines will join before being connected to the drain tank line. The line to the drain tank was closer than the ventilation and no advantages of using the ventilation could be found. No one way valves are used, as the release valves will just be opened separately from each other.

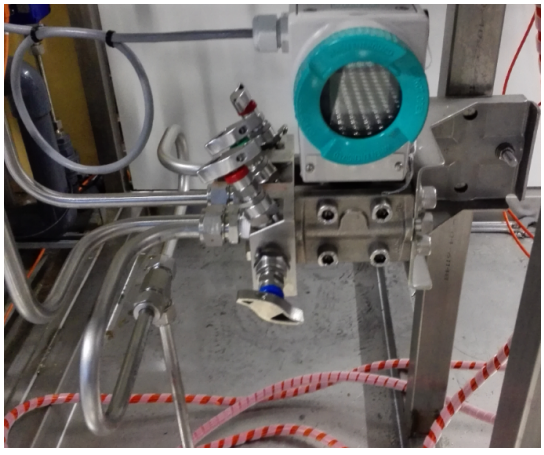

Figure F.1: The Siemens SITRANS P500 with attached 5-way valve manifold.

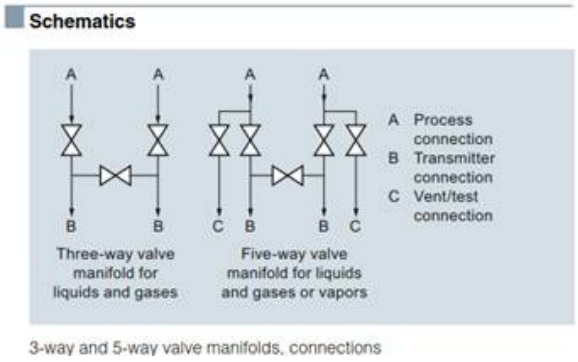

Figure F.2: Schematics of the 3-way and 5-way valve manifolds. The 5-way valve manifold includes two release valves.

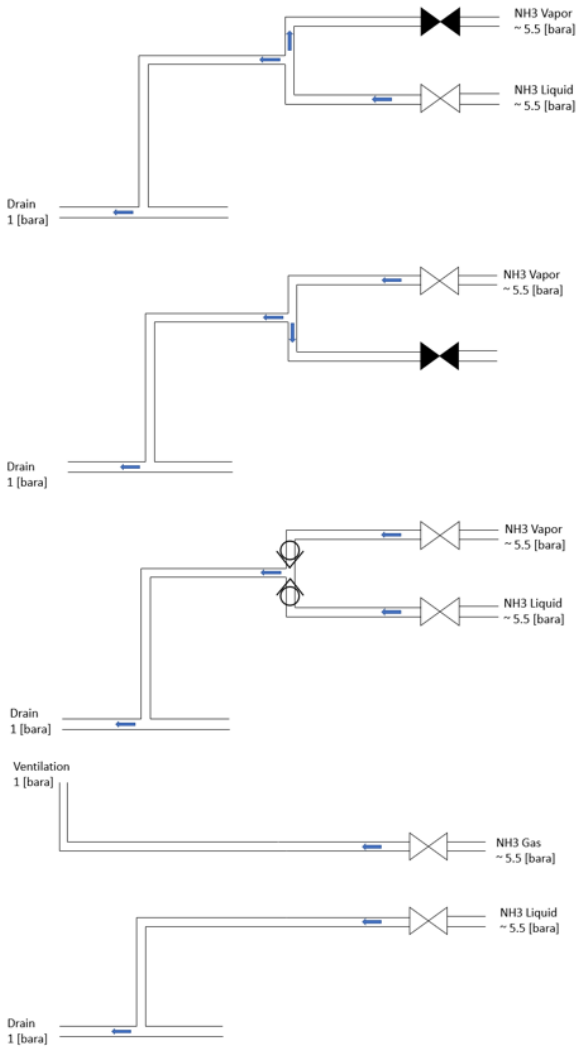

Figure F.3: Possible arrangements of the release valves of the 5-way valve block connected to the SITRANS P500 Pressure difference sensor.

G

BYPASS VALVE TESTS

At the start of the project, a new bypass valve was implemented in the OTEC-demo, in order to regulate the vapor flow and thereby the vapor fraction. To test the influence of the bypass valve, a set of measurements was done with varying angular positions of the bypass valve. The rest of the input parameters were kept constant.

Figure G.1 shows the influence of the angular position of the bypass on the vapor flow.

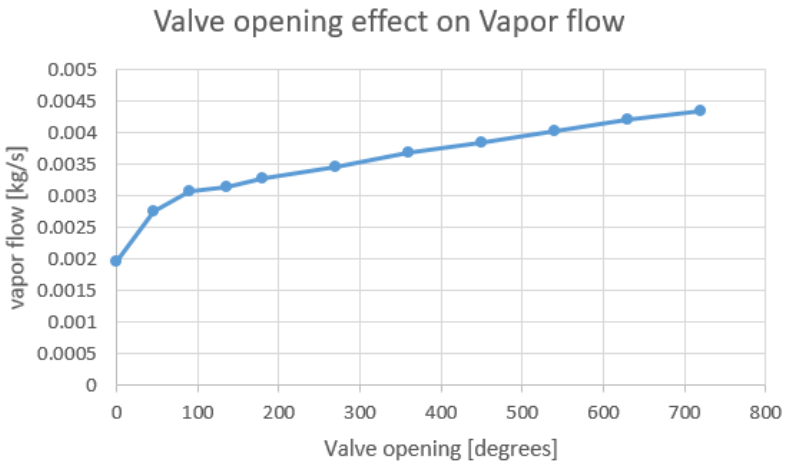

Figure G.1: Influence of bypass valve position on vapor flow

Increasing the vapor flow will increase the power output of the system.

BIBLIOGRAPHY

[1] J. Kirkenier, *Techno-economic optimization of Organic Rankine Cycles using working fluid mixtures for 10 to 25 MW OTEC power plants*, Msc thesis, Delft University of Technology (2014).

[2] R. Goudriaan, *Performance analysis of ammonia and ammonia-water as working fluids for Ocean Thermal Energy Conversion power plants*, Msc thesis, Delft University of Technology (2017).

[3] L. Kuikhoven, *Influence of the ammonia concentration on the performance of OTEC power cycles*, Msc thesis, Delft University of Technology (2017).

[4] *www.separationequipment.com/m6-plate-heat-exchanger.html,* .

[5] K. Koyama, Y. Nakamura, and H. Arima, *Visualization of fc-72 flow boiling in parallel-and counter-flow plate heat exchangers,* in *ASME 2014 International Mechanical Engineering Congress and Exposition, Montreal, Canada* (2014).

[6] H. Arima, A. Okamoto, and Y. Ikegami, *Local boiling heat transfer characteristics of ammonia/water binary mixture in a vertical plate evaporator,* international journal of refrigeration **34**, 648 (2011).

[7] D. Winkelmann, *Condensation of pure refrigerants and their zeotropic mixtures in plate heat exchangers* (Deutscher Kälte-und Klimatechnischer Verein, 2010).

[8] K. Nilpueng and S. Wongwises, *Two-phase gas–liquid flow characteristics inside a plate heat exchanger,* Experimental Thermal and Fluid Science **34**, 1217 (2010).

[9] E. Jassim, T. Newell, and J. Chato, *Two-phase flow visualization in chevron and bumpy style flat plate heat exchangers,* Heat transfer engineering **27**, 20 (2006).

[10] H. Asano, N. Takenaka, T. Wakabayashi, and T. Fujii, *Visualization and void fraction distribution of downward gas–liquid two-phase flow in a plate heat exchanger by neutron radiography,* Nuclear Instruments and Methods in Physics Research Section A: Accelerators, Spectrometers, Detectors and Associated Equipment **542**, 154 (2005).

[11] P. Vlasogiannis, G. Karagiannis, P. Argyropoulos, and V. Bontozoglou, *Air–water two-phase flow and heat transfer in a plate heat exchanger,* International Journal of Multiphase Flow **28**, 757 (2002).

[12] C. Tribbe and H. Müller-Steinhagen, *Gas/liquid flow in plate-and-frame heat exchangers-part ii: two-phase multiplier and flow pattern analysis,* Heat transfer engineering **22**, 12 (2001).

[13] X. Tao, C. Infante Ferreira, and M. Nuijten, *Two-phase vertical downward flow in plate heat exchangers: flow patterns and condensation mechanisms,* (2018a).

[14] *Alfa Laval CHE00082EN* (2016).

[15] Y.-Y. Yan, H.-C. Lio, and T.-F. Lin, *Condensation heat transfer and pressure drop of refrigerant r-134a in a plate heat exchanger,* International Journal of Heat and Mass Transfer **42**, 993 (1999).

[16] R. K. Sinnott and G. Towler, *Chemical engineering design: SI Edition* (Elsevier, 2009).

[17] V. D. Donowski and S. G. Kandlikar, *Correlating evaporation heat transfer coefficient of refrigerant r-134a in a plate heat exchanger,* in *Engineering Foundation Conference on Pool and Flow Boiling, Alaska* (2000).

[18] B. Thonon, *Design method for plate evaporators and condensers,* in *BHR Group Conference Series Publication*, Vol. 18 (MECHANICAL ENGINEERING PUBLICATIONS LIMITED, 1995) pp. 37–50.

[19] W. Focke, J. Zachariades, and I. Olivier, *The effect of the corrugation inclination angle on the thermohydraulic performance of plate heat exchangers,* International Journal of Heat and Mass Transfer **28**, 1469 (1985).

[20] H. Martin, *A theoretical approach to predict the performance of chevron-type plate heat exchangers,* Chemical Engineering and Processing: Process Intensification **35**, 301 (1996).

[21] H. Kumar, *The plate heat exchanger: construction and design,* in *Institute of Chemical Engineering Symposium Series*, Vol. 86 (1984) pp. 1275–1288.

[22] R. Heavner, H. Kumar, and A. Wanniarachchi, *Performance of an industrial plate heat exchanger: effect of chevron angle,* in *AICHE Symposium series* (American Institute of Chemical Engineers, 1993) pp. 262–262.

[23] Z.-j. Luan, G.-m. Zhang, M.-c. Tian, and M.-x. Fan, *Flow resistance and heat transfer characteristics of a new-type plate heat exchanger,* Journal of Hydrodynamics, Ser. B **20**, 524 (2008).

[24] T. S. Khan, M. S. Khan, and Z. H. Ayub, *Single-phase flow pressure drop analysis in a plate heat exchanger,* Heat transfer engineering **38**, 256 (2017).

[25] F. Geschiere, *OTEC condenser heat exchanger analysis*, Msc thesis, Delft University of Technology (2018).

[26] D.-H. Han, K.-J. Lee, and Y.-H. Kim, *The characteristics of condensation in brazed plate heat exchangers with different chevron angles,* JOURNAL-KOREAN PHYSICAL SOCIETY **43**, 66 (2003).

[27] W. Kuo, Y. Lie, Y. Hsieh, and T. Lin, *Condensation heat transfer and pressure drop of refrigerant r-410a flow in a vertical plate heat exchanger,* International Journal of Heat and Mass Transfer **48**, 5205 (2005).

[28] M. Krauss and K. Stephen, *Enthalpy-concentration chart,* Institute international Du Froid (1991).

[29] K. Rajagopalan and G. C. Nihous, *Estimates of global ocean thermal energy conversion (otec) resources using an ocean general circulation model,* Renewable Energy **50**, 532 (2013).

[30] *www.bluerise.nl,* .

[31] M. M. Abu-Khader, *Plate heat exchangers: recent advances,* Renewable and sustainable energy reviews **16**, 1883 (2012).

[32] K. Thulukkanam, *Heat exchanger design handbook* (CRC Press, 2013).

[33] M. Nuijten, *Modelling in the absorption of binary mixtures in plate heat exchangers,* Msc thesis, Delft University of Technology (2015).

[34] V. Grabenstein, A.-E. Polzin, and S. Kabelac, *Experimental investigation of the flow pattern, pressure drop and void fraction of two-phase flow in the corrugated gap of a plate heat exchanger,* International Journal of Multiphase Flow **91**, 155 (2017).

[35] T. Oshinowo and M. Charles, *Vertical two-phase flow part i. flow pattern correlations,* The Canadian Journal of Chemical Engineering **52**, 25 (1974).

[36] X. Tao, M. E. Dahlgren, and C. Infante Ferreira, *Local nh3 condensation in a plate heat exchanger,* 13th IIR Gustav Lorentzen Conference On Natural Refrigerants. Valencia, Spain. (2018b).

[37] K. Sarraf, S. Launay, G. El Achkar, and L. Tadrist, *Local vs global heat transfer and flow analysis of hydrocarbon complete condensation in plate heat exchanger based on infrared thermography,* International Journal of Heat and Mass Transfer **90**, 878 (2015).

[38] H. Veijer, *Analysis for measurements of an otec power plant,* (2016).

[39] *www.eplastics.com,* .

[40] W. Woishnis and S. Ebnesajjad, *Chemical Resistance of Thermoplastics* (William Andrew, 2012).

[41] H. Westergaard, *Stresses in concrete pavements computed by theoretical analysis,* Public roads (1926).

[42] *Ces edupack,* (2016).

[43] G. A. Longo, *Heat transfer and pressure drop during hydrocarbon refrigerant condensation inside a brazed plate heat exchanger,* International journal of refrigeration **33**, 944 (2010).

[44] G. A. Longo and A. Gasparella, *Heat transfer and pressure drop during hfc refrigerant vaporisation inside a brazed plate heat exchanger,* International Journal of Heat and Mass Transfer **50**, 5194 (2007).

[45] VDI, *Heat atlas,* (2010).

[46] F. M. White, *Fluid mechanics. 5th* (2003).

[47] E. W. Lemmon, M. L. Huber, and M. O. McLinden, *NIST Standard Reference Database 23: Reference Fluid Thermodynamic and Transport Properties-REFPROP, Version 9.1, National Institute of Standards and Technology,* (2013).

[48] M. Conde, *Thermophysical properties of NH3 + H2Omixtures for the industrial design of absorption refrigeration equipment,* (2006).

[49] A. S. Rattner and S. Garimella, *Fast, stable computation of thermodynamic properties of ammonia-water mixtures,* International Journal of Refrigeration **62**, 39 (2016).